



universität  
wien

# DIPLOMARBEIT

Titel der Diplomarbeit

AMS measurement of the reaction  $^{35}\text{Cl}(n,\gamma)^{36}\text{Cl}$  and its relevance to  
astrophysics and nuclear technology

angestrebter akademischer Grad

Magister der Naturwissenschaften (Mag. rer. nat.)

Verfasser:	Stefan Pavetich
Matrikel-Nummer:	0301062
Studienrichtung:	411 Physik
Betreuer:	Mag. Dr. Anton Wallner

Wien, am 31.01.2011



## Abstract

$^{36}\text{Cl}$  is a long-lived radionuclide ( $t_{1/2} = 301000$  a), which is dominantly produced via the reaction  $^{35}\text{Cl}(n,\gamma)^{36}\text{Cl}$ . The seed nuclei of this reaction, the stable  $^{35}\text{Cl}$ , acts as a neutron poison in the nucleosynthesis processes during later burning phases of stars. This makes the reaction important for astrophysical network calculations, aiming to reproduce the abundances of elements. Due to the long half-life of  $^{36}\text{Cl}$ , the cross-section and the production rate of the above reaction are also important for nuclear technology and nuclear waste management. The two main goals of the present work are:

- (i) the production of an independent  $^{36}\text{Cl}/^{35}\text{Cl}$  reference material for accelerator mass spectrometry (AMS) measurements
- (ii) the determination of the Maxwellian averaged cross-section (MACS) of  $^{35}\text{Cl}(n,\gamma)^{36}\text{Cl}$  at 25 keV using AMS.

Approaching the first goal, NaCl pellets were irradiated at the TRIGA Mark II reactor at the Atominstitut der österreichischen Universitäten in Vienna (ATI) and at the Budapest research reactor (BRR). The neutron fluence was determined from the  $^{197}\text{Au}(n,\gamma)^{198}\text{Au}$  neutron capture cross-section, which is a standard at thermal energies, via gold foils attached to and gold powder homogeneously mixed into the NaCl-pellets. With this data we calculated a  $^{36}\text{Cl}/^{35}\text{Cl}$  ratio for the irradiated samples. The AMS measurements on these samples were performed at VERA (Vienna Environmental Research Accelerator), and compared to another AMS reference material from ETH Zürich. The  $^{36}\text{Cl}/^{35}\text{Cl}$  ratios calculated from the  $^{198}\text{Au}$ -activity and the well-known neutron capture cross-section of  $^{197}\text{Au}$ , fits within 1 to 4 % to the measured ratios obtained by AMS for the samples irradiated at the BRR.

To determine the 25 keV-Maxwellian averaged cross-section of  $^{35}\text{Cl}(n,\gamma)^{36}\text{Cl}$ , AMS measurements were performed on two samples, which were irradiated with neutrons of a Maxwell-Boltzmann energy distribution of 25 keV at the Karlsruhe Institute of Technology (KIT). A preliminary value for the cross-section is deduced by combining the results from AMS data and the mean neutron-fluence from the neutron irradiations. The MACS was calculated by weighting the mean value for the cross-section with a Maxwell-Boltzmann energy distribution of 25 keV. From the first irradiated NaCl pellet (KIT1) we obtained a MACS of  $(10.5 \pm 0.6)$  mbarn, which is in good agreement with values from literature. The second sample (KIT2) resulted in a MACS-value of  $(8.8 \pm 0.5)$  mbarn, which is about 20 % lower than the value from the first sample. These difference is higher than expected from the uncertainties of the individual results. A possible origin might be the geometry of the neutron activation, which will be investigated in the future.

---

## Zusammenfassung

Das langlebige Radionuklid  $^{36}\text{Cl}$  ( $t_{1/2} = 301000$  a) wird hauptsächlich durch die Neutroneneinfangreaktion  $^{35}\text{Cl}(n,\gamma)^{36}\text{Cl}$  produziert.  $^{35}\text{Cl}$ , das stabile Saatkernisotop für diese Reaktion fungiert in späteren Brennphasen von Sternen als sogenanntes Neutronengift. Dies macht die obige Reaktion für astrophysikalische Netzwerkrechnungen, deren Ziel die Bestimmung der Element- und Isotopenhäufigkeiten ist, relevant. Wegen der langen Halbwertszeit von  $^{36}\text{Cl}$  sind der Wirkungsquerschnitt und die Produktionsrate von  $^{36}\text{Cl}$ , der obigen Neutroneneinfangreaktion auch für die Kerntechnologie und die nukleare Abfallwirtschaft interessant. Diese Arbeit verfolgt folgende Ziele:

(i) Die Produktion von unabhängigen  $^{36}\text{Cl}/^{35}\text{Cl}$ -Referenzmaterial für AMS (accelerator mass spectrometry) Messungen.

(ii) Die Bestimmung des MACS (Maxwellian averaged cross-section) der Reaktion  $^{35}\text{Cl}(n,\gamma)^{36}\text{Cl}$  für ein Maxwell-Boltzmann Neutronenenergiespektrum von 25 keV.

Für die Produktion des unabhängigen  $^{36}\text{Cl}/^{35}\text{Cl}$ -Referenzmaterials wurden NaCl-Tabletten am TRIGA Mark II Reaktor des Atominstitutes der österreichischen Universitäten (ATI) und am Budapest Research Reactor (BRR) bestrahlt. Durch den sehr gut bekannten thermischen Neutroneneinfangswirkungsquerschnitt der Reaktion  $^{197}\text{Au}(n,\gamma)^{198}\text{Au}$ , der als Standard für thermische Neutronenenergien verwendet wird, wurde mittels Au-Pulver, welches mit dem NaCl-Pulver homogen vermischt wurde und mittels Goldfolien, die an die NaCl-Tabletten befestigt wurden, die Neutronenfluenz bei der Aktivierung bestimmt. Daraus konnte das  $^{36}\text{Cl}/^{35}\text{Cl}$ -Verhältnis berechnet werden. Die AMS-Messung, der am ATI und BRR bestrahlten Proben wurde mit VERA (Vienna Environmental Research Accelerator) durchgeführt. Die  $^{36}\text{Cl}/^{35}\text{Cl}$ -Verhältnisse der Proben wurden mit einem aus Zürich stammenden AMS-Referenzmaterial (ETH K381/4N) verglichen. Das aus den Fluenzmessungen und dem bekannten thermischen Wirkungsquerschnitt für  $^{35}\text{Cl}(n,\gamma)^{36}\text{Cl}$  gewonnene  $^{36}\text{Cl}/^{35}\text{Cl}$ -Verhältnis für die am BRR bestrahlten Proben stimmte mit den aus den AMS-Messungen gewonnenen Werten innerhalb einer Abweichung von 1-4 % überein.

Zur Bestimmung des 25keV-MACS von  $^{35}\text{Cl}(n,\gamma)^{36}\text{Cl}$  wurden AMS-Messungen an Proben aus zwei NaCl Tabletten durchgeführt, die zuvor am Karlsruhe Institute of Technology (KIT) mit einem Neutronenspektrum, welches fast einer Maxwell-Boltzmann-Verteilung von 25 keV entsprach, bestrahlt wurden. Durch die Kombination der mit AMS gemessenen Isotopenverhältnisse und der Neutronenfluenz bei der Bestrahlung ermittelten wir einen experimentellen Wirkungsquerschnitt. Der MACS wurde berechnet indem der experimentell gewonnene Wert mit einer Maxwell-Boltzmann-Energieverteilung von 25 keV gewichtet wurde. Für die beiden bestrahlten Tabletten KIT1 und KIT2 erhielten wir Resultate, die um fast 20% voneinander abweichen (KIT1:  $\sigma_{MACS}=(10.5\pm 0.6)$  mbarn; KIT2:  $\sigma_{MACS}=(8.8\pm 0.5)$  mbarn). Dieser Unterschied ist deutlich höher als die beiden Einzelresultate erwarten lassen. Eine mögliche Ursache dieser Abweichung, die in Zukunft untersucht werden wird, ist die Geometrie bei der Neutronenaktivierung.

---

## Sažetak

Dugoživi radioaktivni nuklid  $^{36}\text{Cl}$  ( $t_{1/2} = 301000$  godina) se uglavnom proizvodi reakcijom uhvata neutrona  $^{35}\text{Cl}(n,\gamma)^{36}\text{Cl}$ . Stabilni nuklid  $^{35}\text{Cl}$  djeluje kao neutronske otrov u kasnijim fazama razvoja zvijezda (reakcije fuzije kisika ili silicija), što čini reakciju relevantnom za proračune astrofizikalnih modelov, čiji je cilj određivanje učestalosti elemenata i izotopa. Udarni presjek reakcije  $^{35}\text{Cl}(n,\gamma)^{36}\text{Cl}$  i brzina proizvodnje  $^{36}\text{Cl}$  su zbog dugog vremena poluraspada ovog izotopa zanimljive za nuklearnu tehnologiju i upravljanje nuklearnim otpadom. Ovaj rad ima sljedeće glavne ciljeve:

(i) Proizvodnju neovisnih referentnih  $^{36}\text{Cl}/^{35}\text{Cl}$  uzoraka za mjerenja AMS-tehnikom (akceleratora masena spektrometrija).

(ii) Odrediti Maxwellijanski usrednjeni udarni presjek (MACS - Maxwellian averaged cross-section) reakcije  $^{35}\text{Cl}(n,\gamma)^{36}\text{Cl}$  za Maxwell-Boltzmann-ov spektar na 25 keV.

Proizvodnja neovisnih referentnih  $^{36}\text{Cl}/^{35}\text{Cl}$  uzoraka je izvršena ozračivanjem tableta NaCl u reaktoru TRIGA Mark II na ATI-u (Atominstitut der österreichischen Universitäten) i na postrojenju BRR-a (Budapest research reactor). Tok neutrona (neutron fluence) je određen pomoću dobro poznatog udarnog presjeka reakcije  $^{197}\text{Au}(n,\gamma)^{198}\text{Au}$ , koji se primijenjuje kao standard za termičke neutronske energije. Rabljeni su sljedeći uzorci: prah Au homogeno izmješan prahom NaCl i folije Au pričvršćene na tablete NaCl. Iz toka neutrona je izračunat omjer  $^{36}\text{Cl}/^{35}\text{Cl}$  u ovim tabletama. Na akceleratora postrojenju VERA (Vienna Environmental Research Accelerator) su izvršena mjerenja uzoraka, ozračenih na ATI-u i BRR-u AMS tehnikom. Dobivene vrijednosti omjera  $^{36}\text{Cl}/^{35}\text{Cl}$  ovih uzoraka su normirane pomoću referentnog materijala ETH K381/4N iz Züricha. Usporedba omjera  $^{36}\text{Cl}/^{35}\text{Cl}$ , dobivenih mjerenjem toka neutrona i poznatog udarnog presjeka reakcije  $^{35}\text{Cl}(n,\gamma)^{36}\text{Cl}$  za termičke energije s izotopnim omjerima iz mjerenja AMS tehnikom pokazuju 1-4 % razliku za uzorke ozračene na BRR-u.

Da bi se odredio MACS reakcije  $^{35}\text{Cl}(n,\gamma)^{36}\text{Cl}$  za 25 keV, izvršena su mjerenja AMS tehnikom na uzorcima dviju tableta NaCl, prethodno ozračenih spektrom neutrona, gotovo identičnom Maxwell-Boltzmann-ovoj raspodijeli od 25 keV, na KIT-u (Karlsruhe Institute of Technology). Kombinacijom izotopnih omjera određenih AMS tehnikom i rezultata za tok neutrona prilikom zračenja, dobili smo eksperimentalni udarni presjek. Konačna vrijednost MACS za ovu reakciju dobivena je nakon korekcije upotrijebljenog spektra energija neutrona na Maxwell-Boltzmann-ov spektar za 25 keV. Za aktivirane tablete KIT1 i KIT2 dobili smo rezultate (KIT1:  $\sigma_{MACS} = (10.5 \pm 0.6)$  mbarn; KIT2:  $\sigma_{MACS} = (8.8 \pm 0.5)$  mbarn), koji odstupaju jedan od drugog za gotovo 20%. U svrhu objašnjavanja dobivenog odstupanja dviju izračunatih vrijednosti, potreban je detaljniji geometrijski izračun neutronske aktivacije uzoraka, koji je izvan opsega ovog istraživanja.

---

# Contents

<b>1</b>	<b>Introduction</b>	<b>1</b>
1.1	Motivation . . . . .	1
1.2	Outline . . . . .	2
1.3	Physical and chemical properties of Cl . . . . .	3
<b>2</b>	<b>Particles and interactions</b>	<b>5</b>
2.1	Nuclei and nuclear reactions . . . . .	6
2.1.1	Cross-sections and reaction rates . . . . .	8
2.1.2	Resonances . . . . .	11
2.1.3	Stellar reaction rates and MACS - Maxwellian averaged cross-section . . . . .	12
2.2	Radioactive decay . . . . .	14
2.2.1	Classification of radioactive decay . . . . .	15
2.3	Interactions of ionizing radiation and matter . . . . .	17
2.3.1	$\gamma$ 's passing through matter . . . . .	17
2.3.2	Heavy charged particles and matter . . . . .	19
2.3.3	Electrons . . . . .	20
<b>3</b>	<b>Nucleosynthesis</b>	<b>23</b>
3.1	Stellar burning phases during hydrostatic equilibrium . . . . .	23
3.2	The s-process . . . . .	25
3.3	Production of $^{36}\text{Cl}$ on Earth . . . . .	27
<b>4</b>	<b>AMS - Accelerator mass spectrometry</b>	<b>29</b>
4.1	Basics of AMS . . . . .	29
4.1.1	The method . . . . .	29
4.1.2	The technique . . . . .	29
4.2	AMS at VERA . . . . .	33
4.2.1	Ion source . . . . .	35
4.2.2	Low-energy side . . . . .	35
4.2.3	Accelerator . . . . .	36
4.2.4	High-energy side . . . . .	37
4.2.5	Detector system . . . . .	38
<b>5</b>	<b>Neutron irradiations and activity measurements</b>	<b>41</b>
5.1	Production of the NaCl-pellets . . . . .	41

5.2	Irradiations of NaCl-pellets . . . . .	46
5.2.1	Irradiations at the ATI . . . . .	46
5.2.2	Irradiations at the BRR . . . . .	48
5.2.3	Irradiations at the KIT . . . . .	50
5.3	Activity measurements . . . . .	52
5.3.1	Calculation of the activity and the neutron fluence . . . . .	53
5.3.2	Results and Discussion . . . . .	63
<b>6</b>	<b>Sample preparation for AMS</b>	<b>71</b>
6.1	Chemical pretreatment . . . . .	72
6.2	Mechanical pretreatment . . . . .	76
<b>7</b>	<b>AMS-measurements and reference material</b>	<b>77</b>
7.1	Prearrangements for the AMS measurement . . . . .	77
7.1.1	The tuning . . . . .	77
7.1.2	The settings . . . . .	81
7.1.3	Electronic signal processing . . . . .	81
7.2	Measuring the $^{36}\text{Cl}/^{35}\text{Cl}$ -ratio . . . . .	82
7.2.1	Measured data . . . . .	82
7.2.2	Preconsiderations and Corrections . . . . .	85
7.2.3	Final AMS results and conclusions . . . . .	93
<b>8</b>	<b>The MACS of <math>^{35}\text{Cl}</math></b>	<b>97</b>
8.1	Determination of the MACS . . . . .	97
8.2	Discussion . . . . .	100
	<b>Bibliography</b>	<b>101</b>
	<b>Acknowledgments</b>	<b>107</b>
	<b>Curriculum vitae</b>	<b>111</b>

# List of Tables

3.1	Burning phases of a 20-25 $M_{\odot}$ star. . . . .	24
5.1	Overview of the masses of the NaCl pellets . . . . .	43
5.2	Masses of the gold foils used as neutron fluence monitors during the neutron irradiations. . . . .	45
5.3	Irradiation of the ATI samples. . . . .	48
5.4	Irradiation of the BUD samples. . . . .	49
5.5	Irradiation of the KIT samples. . . . .	51
5.6	Constants and their uncertainties used for the determination of the neutron fluence during the irradiation. . . . .	54
5.7	Variables used for the determination of the neutron fluence during the irradiations. . . . .	55
5.8	Values for the irradiation time, the efficiency and the self attenuation correction factor for one specific sample. . . . .	64
5.9	Data from the activity measurement of the Au powder in sample BUD1 and the attached Au foils. . . . .	64
5.10	Mean values for the neutron fluence during the irradiation of the first two ATI samples and their calculated $^{36}\text{Cl}/^{35}\text{Cl}$ -ratio of the samples assuming a pure thermal spectrum. . . . .	65
5.11	Mean values of the neutron fluence during the irradiation of the samples BUD1,2,3 and the resulting $^{36}\text{Cl}/^{35}\text{Cl}$ -ratios. . . . .	65
5.12	Mean values of the neutron fluence during the irradiation of ATI5 to ATI9 and the calculated $^{36}\text{Cl}/^{35}\text{Cl}$ -ratios of the samples, assuming a pure thermal spectrum. . . . .	68
5.13	Neutron fluence values during the irradiation of the KIT samples. . . . .	70
5.14	Uncertainties for the calculation of the neutron fluence at KIT, mainly taken from [Dillmann, 2010]. . . . .	70
6.1	Materials used for the chemical preparation of AgCl-samples and AgBr-backings for AMS. . . . .	72
6.2	Dilution of 14 molar $\text{HNO}_3$ to 0.5 molar $\text{HNO}_3$ for the precipitation of S with $\text{Ba}(\text{NO}_3)_2$ and quartz filters . . . . .	73
6.3	Dissolution of $\text{AgNO}_3$ , $\text{KBr}$ and $\text{NaCl}$ in $\text{HNO}_3$ . . . . .	74
6.4	Precipitation of Br to AgBr and Cl to AgCl for different backing and sample material. . . . .	75

List of Tables

---

7.1	Example for the settings of the main components of the accelerator for mass 36. (beam-time session Feb. 2010).	81
7.2	Measured raw data obtained for the runs on cathode KIT1 the from Apr. 2010.	85
7.3	Sulfur corrected ( $(\frac{^{36}\text{Cl}}{^{35}\text{Cl}})_S$ ) and normalized ( $(\frac{^{36}\text{Cl}}{^{35}\text{Cl}})_{S,n}$ ) $^{36}\text{Cl}/^{35}\text{Cl}$ -ratios from the runs on KIT1 from Apr.2010.	88
7.4	Measurement parameters and control quantities for all beam-time sessions.	89
7.5	Blank and reference materials used in all beam-times.	90
7.6	Calculated isotopic ratios for some targets (beam-time session Apr. 2010).	91
7.7	Corrected and normalized isotopic ratios for all targets during all beam-time session.	92
7.8	Final $^{36}\text{Cl}/^{35}\text{Cl}$ -ratios for the neutron activated samples measured by AMS, and normalized to the reference material ETH K381/4N.	93
7.9	Comparison of $^{36}\text{Cl}/^{35}\text{Cl}$ -ratios 1.	94
7.10	Comparison of the $^{36}\text{Cl}/^{35}\text{Cl}$ -ratios 2	94
8.1	Experimental neutron capture cross-section for the two NaCl-pellets.	97
8.2	Values for the spectrum averaged cross-section ( $\langle\sigma\rangle_{SACS}$ ) and the theoretical Maxwellian averaged cross-section ( $\langle\sigma\rangle_{MB}$ ) calculated with the ENDF/B-VII.0 data.	98
8.3	Final values for the MACS of $^{35}\text{Cl}$ obtained in this work and compared to values from literature.	99

# List of Figures

1.1	Chlorine in the chart of nuclides. . . . .	4
2.1	Binding energy per nucleon of stable isotopes with respect to the mass number. . . . .	7
2.2	Cross-section for neutron capture reactions as function of the velocity of the projectile. . . . .	11
2.3	Neutron capture cross-sections of $^{197}\text{Au}$ and $^{35}\text{Cl}$ from sub-thermal energies to 20 MeV. The data was taken from the ENDF/B-VII.0 (Evaluated Nuclear Data File) library. . . . .	12
2.4	Decay scheme of $^{198}\text{Au}$ . . . . .	16
2.5	Decay scheme of $^{36}\text{Cl}$ . . . . .	17
2.6	Photon attenuation coefficients for photon absorption, Compton effect, pair production and the sum of all three reactions in Ge. The data is taken from [Berger <i>et al.</i> , 1990] . . . . .	19
3.1	Relative abundances of neutrons under certain temperature conditions.	26
4.1	Schematic view of VERA. . . . .	34
5.1	Components of the press used for the production of the NaCl pellets. .	42
5.2	Mounted sample press. . . . .	42
5.3	Pressed NaCl+Au-pellet. . . . .	42
5.4	Schematic view of samples ATI2,3,5,6,7,8. . . . .	44
5.5	Schematic view of samples BUD1,2,3 . . . . .	44
5.6	Schematic view of sample ATI9 . . . . .	44
5.7	Scheme of the Budapest Research Reactor (BRR) . . . . .	49
5.8	Schematic view of the NIPS and PGAA at BRR. . . . .	50
5.9	Schematic view of the irradiation assembly at KIT. . . . .	51
5.10	Typical spectrum of an irradiated (NaCl+Au)-pellet (BUD1) recorded with a Ge-detector. . . . .	52
5.11	Illustration of the mean value theorem. . . . .	57
5.12	Efficiency of the Ge-detector at VERA as a function of photon-energy.	61
5.13	Efficiency of the Ge-detector at VERA as a function of the distance between sample and active area of the detector. . . . .	62
5.14	Efficiency of the Ge-detector at VERA as a function of the distance between sample and active area of the detector for the two relevant photon energies for this work. . . . .	63

List of Figures

---

5.15	$\frac{\langle \Phi_{tot,Au-powder} \rangle}{\langle \Phi_{tot,MV foils} \rangle}$ -ratios of the BUD1,2 and ATI5,6,7,8 samples. . . . .	67
5.16	$\frac{\langle \Phi_{tot,Na-powder} \rangle}{\langle \Phi_{tot,MV foils} \rangle}$ -ratios of the BUD1,2 and ATI5,6,7,8 samples. . . . .	69
7.1	Schematic view of VERA, which shows the beam optical elements optimized by Faraday cups, beam profile monitors and detectors. . . . .	79
7.2	Simplified schematic view of the signal processing electronics . . . . .	82
7.3	Two dimensional energy-spectra of blank, standard and KIT1 material. . . . .	84
7.4	Comparison of the final results for KIT1. . . . .	95
8.1	Comparison of a theoretical 25 keV Maxwell-Boltzmann neutron-spectrum with the experimental spectra, as simulated by PINO. . . . .	99

# 1 Introduction

## 1.1 Motivation

One of the main goals of this thesis was the measurement of the Maxwellian averaged cross-section (MACS) of the neutron capture reaction  $^{35}\text{Cl}(n,\gamma)^{36}\text{Cl}$  for a Maxwell-Boltzmann distributed neutron spectrum of 25 keV. Exact knowledge of the neutron capture cross-section is essential for different scientific areas, since it affects the production of  $^{36}\text{Cl}$ .

- **Astrophysical importance:** In later burning phases of massive stars the production of heavy elements above iron strongly depends on neutron capture and radioactive decay (s-process, see section 3.2). For charged particles the Coulomb barriers are too high, and all fusion processes above Fe are endothermic as they result in heavier elements with lower binding energy per nucleon. Therefore neutron capture is the main process for nucleosynthesis above Fe. The required neutrons can be produced in different burning phases (see section 3.1). Statistical physics shows that the energy distribution of these neutrons is of Maxwell-Boltzmann with its maximum at  $E = k_B T$ , where E is the energy, T the temperature and  $k_B$  the Boltzmann constant. To calculate isotopic abundances one needs to know the MACS for the neutron capture reactions. In particular,  $^{35}\text{Cl}$  acts as a neutron poison in the s-process, because it lowers the production of heavier elements by consuming neutrons.
- **Importance for nuclear waste management:** Since mankind uses nuclear technology, there is a growing anthropogenic component in the production of  $^{36}\text{Cl}$ . High energy neutrons in the MeV energy range are produced in nuclear power plants, fission and fusion research reactors and during nuclear weapons tests. By "cooling" the neutrons (e.g. moderation in nuclear reactors) one gets a neutron energy spectrum which ranges from meV up to some MeV. These neutrons produce any kind of stable and radioactive isotopes. The most problematic ones are those with long half-lives and high production rates, as they accumulate steadily over a long period. The production rate of  $^{36}\text{Cl}$  is of great interest, because dissolved  $^{35}\text{Cl}$  is very common in water and  $^{36}\text{Cl}$  has a long half-life. To calculate the production rate one needs to know the cross-section over a large energy region.
- **Geological importance:**  $\frac{^{36}\text{Cl}}{^{35}\text{Cl}}$ -ratios can be used to date geological or water samples, which were exposed to neutrons and cosmic rays, to the age of

some million years. The cross-section of the particular reactions is needed to determine the production rate during the exposure.

The second aim of this thesis was the production of an independent  $^{36}\text{Cl}/^{35}\text{Cl}$  AMS reference material. In AMS, reference materials with well-known isotopic ratios (in the present work the  $^{36}\text{Cl}/^{35}\text{Cl}$ -ratio) are required for the normalization of measured ratios from unknown samples. Sample material with a certain isotopic ratio is produced under well-known experimental conditions. In our case  $^{36}\text{Cl}$  was produced via irradiation of NaCl samples with thermal neutrons. The reference material undergoes the same chemical and mechanical pretreatment as the unknown samples. It is advantageous for the normalization if the standard material and the unknown samples have isotopic ratios of the same order of magnitude.

## 1.2 Outline

The two main goals of this work were:

- 1. Production of an independent  $^{36}\text{Cl}/^{35}\text{Cl}$  reference for accelerator mass spectrometry (AMS)**
- 2. Determination of the Maxwellian averaged cross-section (MACS) of  $^{35}\text{Cl}(n,\gamma)^{36}\text{Cl}$  at 25 keV using AMS.**

The steps to achieve this goals were:

- Irradiation of NaCl-pellets at different neutron-producing facilities; Au-foils and Au-powder was used as fluence-monitor
- Activity measurements of the Au-foils and pellets; calculation of the neutron fluence and of the  $^{36}\text{Cl}/^{35}\text{Cl}$ -ratio via

$$\frac{^{36}\text{Cl}}{^{35}\text{Cl}} = \Phi_n \sigma_{^{35}\text{Cl}(n,\gamma)^{36}\text{Cl}} \quad (1.1)$$

- Chemical and mechanical pretreatment of the samples
- AMS measurements of the samples
- Determination of the MACS of  $^{35}\text{Cl}$  using the AMS- and fluence data

After a short introduction to the element chlorine in section 1.3, the theoretical background of interactions between particles and radiation, especially neutron capture reactions and subsequent secondary reactions will be given in chapter 2. The necessary measurable parameters for the production of  $^{36}\text{Cl}/^{35}\text{Cl}$ -reference materials, the calculation of MACS (isotopic ratios, neutron fluences and cross-sections), and the basic relations between these parameters will be presented in section 2.1.

Approaching the first task (AMS-reference material), neutron activations of NaCl pellets and activity measurements are essential. The production of the samples, the irradiation procedures and the activity measurements are described in detail in chapter 5. The calculation of the  $^{36}\text{Cl}/^{35}\text{Cl}$ -ratio by the measured neutron fluence and the known thermal neutron capture cross-section of  $^{35}\text{Cl}$  is described in section 5.3. These values are AMS independent.

In order to calculate the MACS of  $^{35}\text{Cl}(n,\gamma)^{36}\text{Cl}$  at 25 keV, AMS (Accelerator mass spectrometry) measurements on samples irradiated at KIT (Karlsruhe Institute of Technology) were performed at VERA (Vienna Environmental Research Accelerator), to determine the unknown  $^{36}\text{Cl}/^{35}\text{Cl}$ -ratios of the irradiated samples. The basics of AMS and of AMS at VERA will be presented in chapter 4. The chemical and mechanical pretreatment of the sample material for the AMS measurements will be described in chapter 6 and the AMS-measurement itself will be presented in chapter 7.

The AMS-independent  $^{36}\text{Cl}/^{35}\text{Cl}$ -ratios of the produced reference materials were also compared to other reference materials.

The calculation and discussion of the MACS is presented in chapter 8.

### 1.3 Physical and chemical properties of Cl

Chlorine is the seventeenth element in the periodic table of the elements. With its seventeen protons and electrons, it is the second element in the group of halogens. In its ground state chlorine has the electron configuration  $1s^2 2s^2 2p^6 3s^2 3p^5$ . Under standard conditions (temperature 25°C and pressure 1.01 bar) it occurs as a pale yellow-green gas of  $\text{Cl}_2$  molecules with a density of 2.898 g/l [Linde, 2009]. Its melting point is -101.5°C and its boiling point is -34.04°C [Linde, 2009].

With 3.612724(27) eV [Linde, 2009] chlorine has the highest electron affinity (energy difference between lowest ground state of the atom and lowest state of the corresponding negative ion) of all elements, so chlorine forms negative ions very easily. The electronegativity (relative description of the tendency of an atom in a molecule to attract additional electrons) of chlorine is 3.16 on Pauling scale, which is the second highest of all elements. These are the reasons why chlorine is very reactive and it cannot be found as a neutral atom in nature. It is only found in chemical compounds, mostly as salt like NaCl or KCl but due to its reactivity it combines with nearly every other element. After hydrogen and oxygen, chlorine is the most abundant element in seawater (19.4 g/l). Chlorine is easily dissolved in water. In its form as one compound of salts it is also very common in Earth's crust (145 mg/kg). The data in this paragraph was taken from [Linde, 2009].

Chlorine in its elemental form was first isolated by Carl Wilhelm Scheele in 1774 by the reaction  $\text{MnO}_2 + 4\text{HCl} \rightarrow \text{MnCl}_2 + \text{Cl}_2 + 2\text{H}_2\text{O}$  and today it is mostly produced via  $2\text{NaCl} + 2\text{H}_2\text{O} \rightarrow \text{Cl}_2 + \text{H}_2 + 2\text{NaOH}$  (electrolysis). Chlorine is used for

<b>K 35</b> 190 ms $\beta^+$ $\gamma$ 2583; 2590... $\beta$ 1.425; 1.705; 1.555...	<b>K 36</b> 342 ms $\beta^+$ 9.9... $\gamma$ 1973; 2433; 2208... $\beta$ 0.970; 0.693; $\beta$ 2.015; 2.725...	<b>K 37</b> 1.22 s $\beta^+$ 5.1... $\gamma$ 2796...	<b>K 38</b> 924.6 ms; 7.6 m $\beta^+$ 5.0 $\beta^+$ 2.7; $\gamma$ 2166...	<b>K 39</b> 93.2581 $\alpha$ 2.1 $\sigma_{n, \alpha}$ 0.0043 $\sigma_{n, p} < 0.00005$	<b>K 40</b> 0.0117 $1.28 \cdot 10^9$ a $\beta^-$ 1.3; $\epsilon$ ; $\beta^+$ ... $\gamma$ 1461; $\sigma$ 30; $\sigma_{n, \alpha}$ 0.42; $\sigma_{n, p}$ 4.4	<b>K 41</b> 6.7302 $\alpha$ 1.46
<b>Ar 34</b> 844 ms $\beta^+$ 5.0... $\gamma$ 666; 3129... $\beta$	<b>Ar 35</b> 1.78 s $\beta^+$ 4.9... $\gamma$ 1219; (1763...)	<b>Ar 36</b> 0.3365 $\alpha$ 5 $\sigma_{n, \alpha}$ 0.0054 $\sigma_{n, p} < 0.0015$	<b>Ar 37</b> 35.0 d $\epsilon$ $n$ $\gamma$ $\sigma_{n, \alpha}$ 1080 $\sigma_{n, p}$ 37	<b>Ar 38</b> 0.0632 $\alpha$ 0.6	<b>Ar 39</b> 269 a $\beta^-$ 0.6 $n$ $\gamma$ $\sigma$ 600 $\sigma_{n, \alpha} < 0.29$	<b>Ar 40</b> 99.6003 $\alpha$ 0.64
<b>Cl 33</b> 2.51 s $\beta^+$ 4.5... $\gamma$ (841; 1966; 2867...)	<b>Cl 34</b> 32.0 m; 1.53 s $\beta^+$ 2.3... $\gamma$ 2127; 1175; 3240... $\beta^+$ 4.5; $n$ $\gamma$	<b>Cl 35</b> 75.76 $\alpha$ 43.7 $\sigma_{n, \alpha} \sim 8 \cdot 10^{-5}$ $\sigma_{n, p}$ 0.44	<b>Cl 36</b> $3.0 \cdot 10^5$ a $\sigma < 10$ $\sigma_{n, \alpha}$ 0.00059 $\sigma_{n, p}$ 0.046	<b>Cl 37</b> 24.24 $\alpha$ 0.43	<b>Cl 38</b> 37.18 m $\beta^-$ 4.9... $\gamma$ 2168; 1642...	<b>Cl 39</b> 56 m $\beta^-$ 1.9; 3.4... $\gamma$ 1267; 250; 1517...
<b>S 32</b> 94.99 $\alpha$ 0.55 $\sigma_{n, \alpha} < 0.0005$	<b>S 33</b> 0.75 $\alpha$ 0.46 $\sigma_{n, \alpha}$ 0.12 $\sigma_{n, p}$ 0.002	<b>S 34</b> 4.25 $\alpha$ 0.25	<b>S 35</b> 87.5 d $\beta^-$ 0.2 $n$ $\gamma$	<b>S 36</b> 0.01 $\alpha$ 0.24	<b>S 37</b> 5.0 m $\beta^-$ 1.8; 4.9... $\gamma$ 3103...	<b>S 38</b> 2.83 h $\beta^-$ 1.0; 2.9... $\gamma$ 1942; 1746...
<b>P 31</b> 100 $\alpha$ 0.17	<b>P 32</b> 14.26 d $\beta^-$ 1.7 $n$ $\gamma$	<b>P 33</b> 25.34 d $\beta^-$ 0.2 $n$ $\gamma$	<b>P 34</b> 12.4 s $\beta^-$ 5.4... $\gamma$ 2127...	<b>P 35</b> 47.4 s $\beta^-$ 2.3... $\gamma$ 1572...	<b>P 36</b> 5.6 s $\beta^-$ $\gamma$ 3291; 903; 1638; 2540...	<b>P 37</b> 2.31 s $\beta^-$ $\gamma$ 646; 1563; 2254...

Figure 1.1: Chlorine in the chart of nuclides from [Magill *et al.*, 2006].

the disinfection of water, but there are various other applications. It is also used for sanitary products, in the paper-, textile- and petrol industry. Due to its poisonous effect, it is also used in insecticides and was used as war gas in world war I [Linde, 2009].

The atomic mass of chlorine is  $m=35.453$  g/mol [Magill *et al.*, 2006]. Chlorine has two stable isotopes namely  $^{35}\text{Cl}$  with a natural abundance of 75.77(4) % and  $^{37}\text{Cl}$  with a natural abundance of 24.23(4) % [NNDC, 2005].

According to [NNDC, 2005] (data from 2005) there are 23 more known chlorine isotopes (21) and isomers (2), with mass numbers from 29 to 51. The chlorine isotopes with mass numbers smaller than 35 decay by  $\beta^+$ -decay, electron capture or proton emission [NNDC, 2005]. All of the neutron rich Cl-isotopes decay by emission of  $\beta^-$ -radiation [NNDC, 2005]. All these radioactive nuclides are short-lived with half-lives up to 56 minutes [NNDC, 2005]. The only exception is the isotope of interest for this thesis,  $^{36}\text{Cl}$ . Its half-life of  $t_{1/2} = 3.01(2) \cdot 10^5$  a [NNDC, 2005] is long enough that measurable traces of this isotope can be found in nature.  $^{36}\text{Cl}$  is mainly produced by neutron capture on  $^{35}\text{Cl}$ , but it can also be produced by spallation of argon and by muon capture on  $^{40}\text{Ca}$ . A more detailed description of nuclear reactions with a focus on neutron capture will be given in chapter 2.1.

## 2 Particles and interactions

In the last century the study of cosmic rays and of nuclear reactions in particle accelerators and colliders lead to the discovery of more and more subatomic particles. These particles were classified by their measured elemental properties like mass, charge, spin, isospin, parity, hypercharge and strangeness. All physical interactions between these particles are based on four forces [Segré, 1977].

1. **Strong interaction** is the strongest force. Its range is  $10^{-15}$  m and it only effects particles with color charge. This force binds the neutrons and protons in a nucleus. The interaction itself is described as an exchange of gluons. There are eight different gluons. They are all massless and each of them carries a combination of a color and an anticolor.
2. **Electromagnetic interaction** is approximately hundred times weaker than the strong interaction. It effects all charged particles and all particles with a magnetic momentum. The range of this interaction is infinite, because of the  $1/r$  dependence of the electromagnetic potential (Coulomb potential). The interacting particles are the massless, uncharged photons  $\gamma$ .
3. **Weak interaction** has  $10^{-13}$  times the strength of the strong interaction and also has a very short range. This force is responsible for  $\beta$  - decay by the exchange of the massive  $W^+$ ,  $W^-$ , or  $Z$  particles.
4. **Gravitation** is the weakest of the four forces and has only  $10^{-38}$  times the strength of the strong interaction, but due to its  $1/r$  potential an infinite range. The postulated exchange particle of this interaction is the massless graviton. It effects all particles but -because of its weakness- it is only important on large scales and can be neglected for our purposes.

Basically there are two groups of particles, the fermions and the bosons, which can be divided in further subclasses:

- **Fermions** have a half integral spin. Pauli's law says that a certain quantum-mechanical state can only be populated by a single fermion. Two fermions have to differ in at least one quantum number. All of our worlds non-exotic matter is built up of Fermions in its bases. There are two subclasses of Fermions:
  - *Leptons* are colorless particles. This group contains the electron  $e^-$  and the electron neutrino  $\nu_e$ , the muon  $\mu^-$  and the muon neutrino  $\nu_\mu$ , the tauon

$\tau^-$  and the tauon neutrino  $\nu_\tau$ . The  $e^-$ ,  $\mu^-$ ,  $\tau^-$  are negatively charged and have mass. So they are affected by all forces except the strong interaction. Neutrinos are not charged. They are only affected by the weak and the gravitational interaction. All of these particles also have a corresponding antiparticle.

- *Quarks* are massive particles with electrical and color charge. There are six so called flavors of quarks which are named: up, down, strange, charm, bottom and top, and differ in their mass, charge and other properties. Every quark exists in all three colors and there is an antiquark to every quark flavor. All baryonic matter which includes protons and neutrons is made up of a combination of three quarks. So baryons are also fermions.
- **Bosons** have an integer spin. Any number of bosons can occupy the same quantum state. The exchange particles of all four interactions are bosons and the postulated Higgs particle would also be a boson. Mesons which consist of a quark antiquark pair are bosons too.

Conservation laws build the basis of the physical and mathematical description of interactions between particles. Energy, momentum and angular momentum are conserved due to fundamental invariances of space and time [Segré, 1977].

## 2.1 Nuclei and nuclear reactions

Every nucleus consists of protons and neutrons. Protons are made up of two up and one down quark, are positively charged ( $q_p = 1.602176487(40) \cdot 10^{-19}\text{C}$ ) [NIST, 2006] and they have a mass of  $m_p = 938.272013(23)\text{MeV}c^2$  [NIST, 2006]. Neutrons have a similar mass of  $m_n = 939.565346(23)\text{MeV}/c^2$  [NIST, 2006]. They are not charged, but have a magnetic momentum, so they still can be affected by electromagnetic forces. Two down quarks and one up quark build a neutron. Protons are stable, but free neutrons are unstable to  $\beta$ -decay. The half-life of free neutrons is  $t_{1/2} = 10.24(2)\text{min}$  [IAEA, 2007-2010].

For the study of nuclear reactions some definitions are needed. The mass number  $\mathbf{A}$  of a nucleon is the sum of the number of protons  $\mathbf{Z}$  (atomic number) and the number of neutrons  $\mathbf{N}$ . The value for the mass of a nucleus ( $M_{nucleus}$ ) is always smaller than the sum of the masses of its protons and neutrons, because of the release of the binding energy ( $E_B$ ) which is defined as the required energy to disaggregate the nucleus in its constituents.

$$E_B = (Zm_p + Nm_n - M_{nucleus})c^2 \quad (2.1)$$

The value for the binding energy per nucleon varies between 7 and 9 MeV for the most stable nuclei (see fig. 2.1).

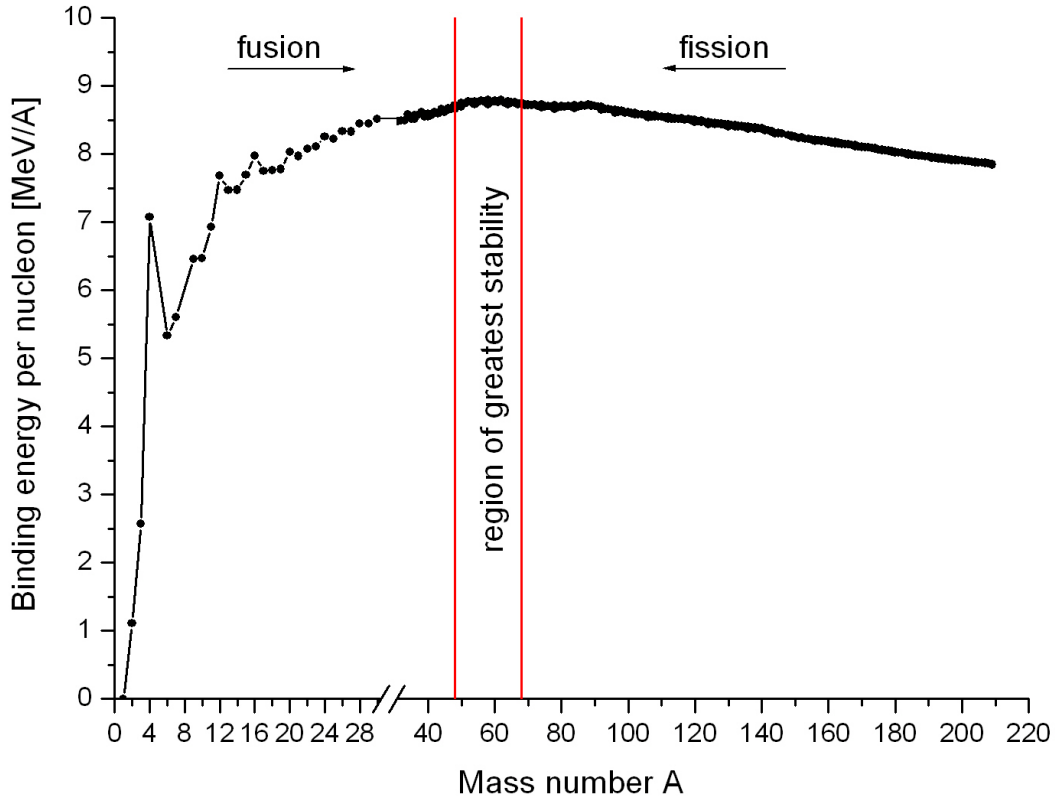


**Figure 2.1:** Binding energy per nucleon of stable isotopes with respect to the mass number [Audi *et al.*, 2003].

A simple model for nuclei is the liquid drop model, which postulates the independence of the binding energy per nucleon and the density of the nuclei from the mass number. This is analogous to liquid droplets where the energy for vaporization and the density are independent from the volume of the droplet [Segré, 1977]. In other models like the Fermi model the protons and neutrons occupy discrete energy levels in separate potential wells. The depth of this potential wells corresponds to the separation energy of the single nucleons. In this model excitation of the nucleus is described by rising one or more nucleons to higher energy levels.

In this work nuclei will be noted as  ${}^A\text{X}$  and nuclear reactions as

$${}^A\text{X}(x, y){}^B\text{Y} \quad (2.2)$$

where  ${}^A\text{X}$  is the target nucleus which, together with the projectile  $x$ , forms the initial state  $\mathbf{i}$ .  ${}^B\text{Y}$  is the reaction product and  $y$  is the ejectile. They form the final state  $\mathbf{f}$ . The rest-mass difference between the initial and the final state is called  $Q$ -value of a reaction. If the  $Q$ -value is positive the reaction is exotherm (energy is released by

the reaction). Reactions with a negative Q-value are endotherm and have an energy threshold. From the kinematics of such a reaction one can calculate that the center of mass energy has to be equal or greater than the Q-value so that the reaction can take place.

$$\frac{1}{2} \frac{m_x m_X}{m_X + m_x} v_x^2 = |Q| \quad (2.3)$$

At low projectile energies, up to several MeV, which is the energy region important to this thesis, there are two main classes of nuclear reactions.

- **Direct reactions** occur at any energies and on time scales of  $10^{-22}$  s. This is the time needed by a projectile to cross the target. Particle emission is anisotropic, forward peaked and the ejectiles have discrete energies [Segré, 1977].
- **Compound nucleus reactions** take place at projectile energies up to 50 MeV. During this reaction the incident projectile and the target form an excited compound nucleus. Life times of these compound nuclei are in the range of  $10^{-16} - 10^{-14}$  s. After this time the compound nucleus deexcites by emitting particles. The emission is practically isotropic and the energies of the ejectiles are nearly Maxwell-Boltzmann distributed [Segré, 1977].

Higher energies can favor other nuclear reactions like pre-equilibrium reactions ( $E > \text{MeV}$ ), spallation reactions ( $E > 200 \text{MeV}$ ) or fragmentation reactions ( $E > 500 \text{MeV}$ ).

### 2.1.1 Cross-sections and reaction rates

This chapter is a summary of the discussion of cross-sections given in [Segré, 1977]. The cross-section  $\sigma$  is defined as a measure for the probability that a specified reaction between a projectile and a target takes place. It is measured in units of area ( $1 \text{b}(\text{arn}) = 10^{-24} \text{cm}^2$ ) and it is the physical proportionality factor which connects the number of target nuclei  $N_X$  and the fluence  $\Phi$  (number of projectiles per area) with the number of produced nuclei  $N_Y$ .

$$N_Y = \sigma N_X \Phi \quad (2.4)$$

Assuming that the cross-section is small enough, so that one can neglect the decreasing number of targets by the reaction itself one can easily build the time-derivation of the above formula and one gets the reaction rate  $N'$ .

$$N' = \sigma N_X \varphi \quad (2.5)$$

Where  $\varphi$  is the incident flux (projectiles per area and time) which can also be written as the product of the density of the projectiles  $n_x$  and the velocity of these projectiles  $v_x$ . Using this product and dividing the above formula by the target volume  $V_T$  ( $n_X = N_X/V_T$ ) one can get the total reaction rate  $r$ :

$$r = n_x \sigma v_x n_X \quad (2.6)$$

The first three factors are the so called transition probability per unit of time,  $w$ :

$$w = n_x v_x \sigma \quad (2.7)$$

Fermi's golden rule No.2 also gives an expression for the transition probability of a definite initial state to a continuum of final states, which only means that despite a specified momentum, angular momentum and polarization in the initial state the conservations laws allow a whole continuum of final states. One can get the transition probability by:

$$w = \frac{2\pi}{\hbar} \langle |H_{if}| \rangle^2 \frac{dn}{dE} \quad (2.8)$$

$\frac{dn}{dE}$  is the density of final states and  $H_{if}$  is the transition matrix (Hamiltonian operator). This leads us to two "problems": first,  $\frac{dn}{dE}$  is infinite for a continuum and second it is not possible to calculate  $H_{if}$  in general [Segré, 1977]. The first problem can be solved under the assumption that the final states are enclosed in a box of finite volume  $\Omega$  and one gets the expression:

$$\frac{dn}{dE} = \frac{4\pi\Omega}{(2\pi\hbar)^3} p_y^2 \frac{dp_y}{dE} \quad (2.9)$$

Where  $p_y$  is the momentum of the ejectile. The transition matrix can be written as:

$$H_{if} = \langle \psi_f | U | \psi_i \rangle \quad (2.10)$$

where  $\psi_f, \psi_i$  are normalized wave functions in  $\Omega$ , and  $U$  is the interaction potential. Under some assumptions [Segré, 1977] one can approximate  $H_{if}$  as:

$$H_{if} \cong \frac{\langle U \rangle \times V}{\Omega} \quad (2.11)$$

$V$  is the volume of the nucleus and  $\langle U \rangle$  is the average interaction potential over the nuclear volume. In the above equations the Coulomb potential was not considered, so they are only valid for neutral particles x,y. If the projectile and ejectile are charged, their wavefunctions are reduced by Coulomb repulsion. If both particles are charged one gets:

$$H_{if} \cong \frac{\langle U \rangle \times V}{\Omega} e^{(-G_x - G_y)} \quad (2.12)$$

where  $G$  is the Gamow factor given by:

$$G_x = \frac{1}{\hbar} \int_{R_2}^{R_1} [2m_x(V_x - E_x)]^{1/2} dr \cong \frac{\pi Z_X Z_x e^2}{\hbar v_x} \quad (2.13)$$

Where the  $Z$ 's are the atomic numbers of the involved particles and  $e$  is the elementary charge. One can choose the normalization volume  $\Omega$  so that there is only one projectile in this volume and  $n_x$  becomes  $1/\Omega$ . By combination of the equations 2.7, 2.8 and 2.9 one gets:

$$\frac{1}{\Omega} v_x \sigma = \frac{2\pi}{\hbar} \langle |H_{if}| \rangle^2 \frac{4\pi\Omega}{(2\pi\hbar)^3} p_y^2 \frac{dp_y}{dE} \quad (2.14)$$

For  $dE$  one can also write  $v_y dp_y$  and with  $M_{if} = \Omega H_{if}$  one gets:

$$\sigma = \frac{1}{\pi\hbar^4} \langle |M_{if}| \rangle^2 \frac{p_y^2}{v_x v_y} \quad (2.15)$$

If the spin  $I$  of the particles should also be considered the Hamiltonian has to be modified. One has to build the mean over all initial states and the sum over all final states. The equation for the cross-section is slightly modified to:

$$\sigma = \frac{1}{\pi\hbar^4} \langle |M_{if}| \rangle^2 \frac{p_y^2}{v_x v_y} (2I_Y + 1)(2I_y + 1) \quad (2.16)$$

Here  $I_Y$  is the spin of the produced particle and  $I_y$  is the spin of the ejectile. One can see that:

$$\sigma \propto \frac{p_y^2}{v_x v_y} e^{(-G_x - G_y)} \quad (2.17)$$

With the last equation the general characteristics of cross-sections of some typical nuclear reactions can be derived (see [Segré, 1977]). All the considerations made above are only valid if there are no resonances in the energy region of interest.

For our purposes the most important case of nuclear reactions, are neutron induced reactions (see Fig 2.2). Examples for this reaction are  $(n, \gamma)$ ,  $(n, p)$ ,  $(n, \alpha)$  and neutron induced fission. The velocity of the ejectil  $v_y$  can be assumed constant, because the  $Q$ -values of these reactions are usually in the range of MeV and so the changes of the low energy of the projectile (eV) do not affect the calculation of  $v_y$ . Furthermore  $v_y \cong const$  implies  $E_y \cong const$  and  $G_y \cong const$ . The Gamow factor of the neutral incident particle is zero. So one can write:

$$\sigma \propto \frac{1}{v_x} \propto \frac{1}{\sqrt{E_x}} \quad (2.18)$$

This  $\frac{1}{v_x}$  behavior (see fig. 2.2) suggests that the neutron capture cross-section for neutrons in the 25 keV range is approximately 1000 times smaller than the neutron capture cross-section of thermal neutrons ( $E = 25$  meV). Due to the existence of

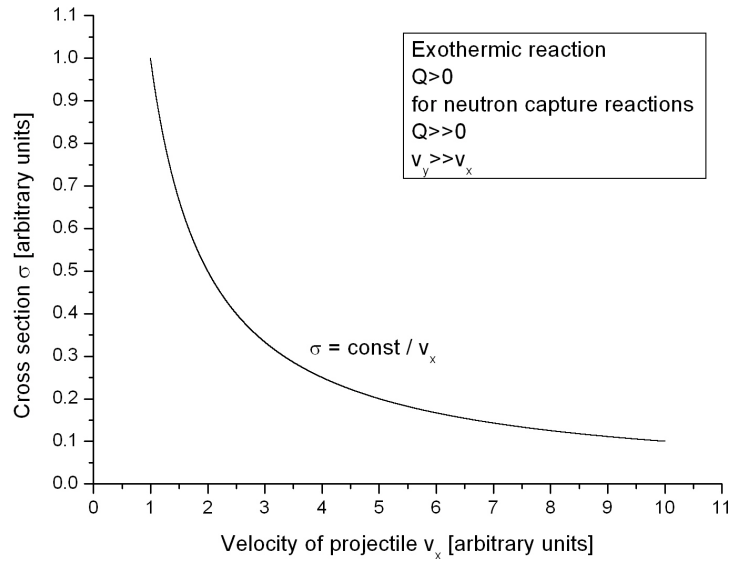


**Figure 2.2:** Cross-section for neutron capture reactions as function of the velocity of the projectile. Resonances (see next chapter) were not taken into account here.

resonances, which will be described in the next section this is only partly true (see fig. 2.3).

### 2.1.2 Resonances

A nuclear reaction is resonant if the center of mass energy of the target and the projectile equals the energy of an excited state of the compound nucleus. The cross-section of a reaction at resonant energies is basically described by the Breit-Wigner formula. Based on [Segré, 1977] one gets:

$$\sigma(n, \gamma) = \pi \lambda \lambda_r \frac{\Gamma_\gamma \Gamma_n^{(r)}}{\Gamma^2/4 + (E - E_r)^2} \frac{2I_Y + 1}{(2I_n + 1)(2I_X + 1)} \quad (2.19)$$

for  $(n, \gamma)$  reactions [Segré, 1977].  $\lambda$  and  $\lambda_r$  are the wavelengths of the neutron and the compound nucleus.  $E$  is the center of mass energy,  $E_r$  is the resonance energy,  $I_Y$ ;  $I_n = 1/2$  and  $I_X$  are the spins of the compound nucleus, the neutron and the target.  $\Gamma_n$  is the neutron width,  $\Gamma_\gamma$  is the radiative width,  $\Gamma = \Gamma_n + \Gamma_\gamma$  is the resonance width of the reaction. These widths give the energy widths in which the resonance occurs and the strength of the resonance.  $\Gamma$  also defines the lifetime  $\tau$  of the compound nucleus by  $\Gamma\tau \approx \hbar$ . At resonant energies the cross-section can be orders of magnitude higher than at non-resonant energies (see Fig. 2.3).

To classify resonances one can use the resonance width as parameter. Narrow and isolated resonances have widths of several eV, which correspond to lifetimes of  $10^{-16}$  s. Broad resonances have widths of several MeV. The time scale for these direct

reactions is about  $10^{-22}$  s.

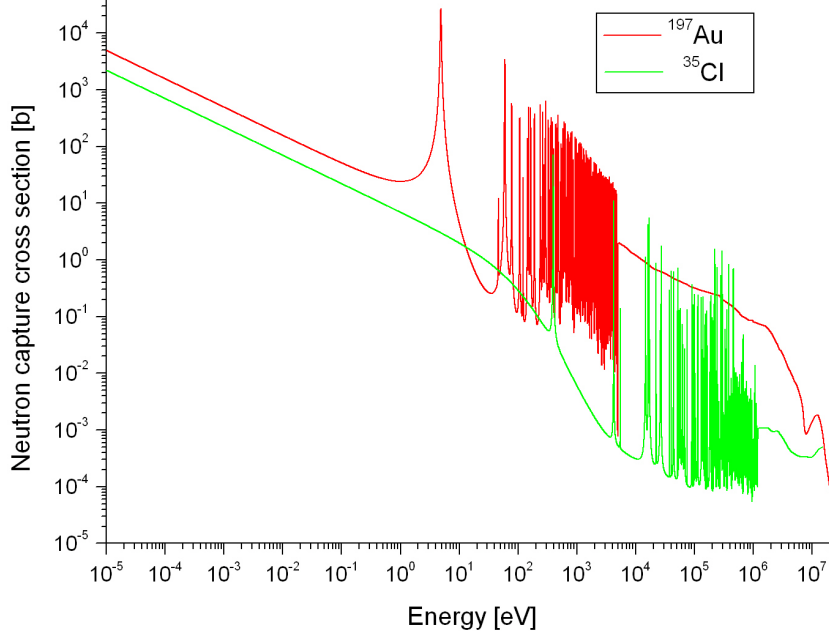


**Figure 2.3:** Neutron capture cross-sections of  $^{197}\text{Au}$  and  $^{35}\text{Cl}$  from sub-thermal energies to 20 MeV. The data was taken from the ENDF/B-VII.0 (Evaluated Nuclear Data File) library.

### 2.1.3 Stellar reaction rates and MACS - Maxwellian averaged cross-section

Equation 2.6 defines the total reaction rate for particles of a defined velocity (energy). If the particle energies (velocities) are distributed, one has to integrate over the whole distribution. The averaged reaction rate per particle pair is then given by:

$$\langle \sigma v \rangle = \int_0^{\infty} \phi(v) v \sigma(v) dv \quad (2.20)$$

Where  $v$  is the velocity of the incident particle and  $\phi(v)$  represents the velocity distribution of these projectiles. So  $\phi(v)dv$  is the probability to find a projectile in the velocity range between  $v$  and  $v + dv$ . The distribution can be normalized so that  $\int_0^{\infty} \phi(v)dv = 1$ .

At stellar conditions neutrons of different energies are produced in various reactions (for examples see chapter 3.2). These neutrons thermalize quickly due to scattering processes. For example, they reach kinetic equilibrium at the local temperature of approximately  $2 - 3 * 10^8\text{K}$  for red giant stars, which are the interesting stars for our purpose. Such a temperature corresponds to typical particle energies of 20 – 30 keV. The thermalization time of approximately  $10^{-11}$  s is short compared to the

lifetime for neutron capturing [Allen *et al.*, 1971]. Thermalization of the neutrons means that their velocities and accordingly their energies follow a Maxwell-Boltzmann distribution of the local temperature.

$$\phi(v)dv = \frac{4}{\sqrt{\pi}} \left(\frac{v}{v_T}\right)^2 e^{-\left(\frac{v}{v_T}\right)^2} \frac{dv}{v_T} \quad (2.21)$$

with  $v_T = \sqrt{\frac{2k_B T}{\mu}}$ , where  $k_B$  is the Boltzmann constant,  $T$  the temperature and  $\mu = \frac{m_x m_X}{m_x + m_X}$  is the reduced mass. In terms of energy, equation 2.21 can be written as:

$$\phi(E)dE = \frac{2}{\sqrt{\pi}} \frac{1}{(kT)^{3/2}} \sqrt{E} e^{-\left(\frac{E}{kT}\right)} dE \quad (2.22)$$

Combining equations 2.20 and 2.21 one gets the Maxwellian averaged capture rate (stellar reaction rate) [Allen *et al.*, 1971].

$$\langle \sigma v \rangle = \frac{4}{\sqrt{\pi}} \frac{1}{(v_T)^2} \int_0^\infty v^2 \frac{v}{v_T} \sigma(v) e^{-\left(\frac{v}{v_T}\right)^2} dv \quad (2.23)$$

The Maxwellian averaged cross-section (MACS) is then defined as:

$$\sigma_{MACS} = \frac{\langle \sigma v \rangle}{v_T} = \frac{4}{\sqrt{\pi}} \frac{1}{(v_T)^2} \int_0^\infty v \sigma(v) \left(\frac{v}{v_T}\right)^2 e^{-\left(\frac{v}{v_T}\right)^2} dv \quad (2.24)$$

or in terms of energy:

$$\sigma_{MACS} = \frac{2}{\sqrt{\pi}} \frac{1}{(kT)^2} \int_0^\infty \sigma(E) E e^{-\frac{E}{kT}} dE \quad (2.25)$$

MACS are calculated for energies of typically 25 or 30 keV, which corresponds to stellar neutron energies. If the individual resonances can be experimentally resolved the  $\sigma_{MACS}$  can be determined by solving the above integral. This can be done by separating it into the non-resonant  $1/v$  component and the resonances. The  $1/v$  component can be integrated and the resonances can be treated as a series of delta functions, whose sum can be calculated. If it is not possible to resolve the individual resonances one can obtain an averaged cross-section at a certain energy which is virtually equivalent to the MACS at this energy. In this thesis we will determine the  $\sigma_{MACS}(25 \text{ keV})$ . This will be done by calculating the experimental cross-section  $\sigma$  from  $\sigma = \frac{^{36}\text{Cl}}{^{35}\text{Cl}} \frac{1}{\Phi}$  (see equation 2.4). The irradiations of the samples were performed with a quasi Maxwellian neutron spectrum (more detailed information on the irradiation will be given in chapter 5). The experimental cross-section needs to be modified to correct for the difference between the experimental and a real Maxwell-Boltzmann spectrum. [Ratynski & Käppeler, 1988]

$$\sigma_{MACS} = \frac{2}{\sqrt{\pi}} \frac{\langle \sigma \rangle_{MB}}{\langle \sigma \rangle_{SACS}} * \sigma_{exp} \quad (2.26)$$

Where  $\frac{2}{\sqrt{\pi}}$  is a conventional normalization factor (normalization of MB-spectrum) [Ratynski & Käppeler, 1988]. The  $\langle\sigma\rangle_{MB}$  results from folding the real Maxwell-Boltzmann spectrum with the differential cross-section data for  $^{35}\text{Cl}$  (in our case taken from ENDF/B-VII.0 (Evaluated Nuclear Data File), [NEA, 2010]) and  $\langle\sigma\rangle_{SACS}$  (spectrum averaged cross-sections) is calculated by folding the experimental neutron spectrum with the differential cross-section data.

$$\langle\sigma\rangle_{MB} = \frac{\int_0^\infty \sigma(E) E e^{-\frac{E}{kT}} dE}{\int_0^\infty E e^{-\frac{E}{kT}} dE} \quad (2.27)$$

$$\langle\sigma\rangle_{SACS} = \frac{\int_0^\infty \sigma(E) N(E) dE}{\int_0^\infty E N(E) dE} \quad (2.28)$$

The course of the cross-section function, which can be calculated theoretically very well, has to be known for the weighting. Due to the fact that the neutron spectrum and the differential cross-section data consist of small energy steps, the integrals in equation 2.27 and 2.28 will be replaced by sums in our calculations.

## 2.2 Radioactive decay

Radioactive decay is a statistical process. The probability for the decay of a particle in an infinitesimal short time interval  $dt$  is given by  $\lambda_d dt$ , where  $\lambda_d$  is the decay constant which is different for all unstable isotopes. Radioactive decay events are Poisson-distributed. Environmental, physical and chemical conditions normally do not influence the decay. There is one exception for the case of electron capture which will be described later in this chapter. Radioactive decay is described by the following differential equation:

$$dN = -\lambda_d N(t) dt \quad (2.29)$$

Here  $N(t)$  is the number of atoms and  $dN$  is the change in the number of atoms. The equation can be solved by separating the variables. With the initial condition  $N(t=0) = N_0$  one gets:

$$N(t) = N_0 e^{-\lambda_d t} \quad (2.30)$$

Due to the statistical nature of the decay,  $N$  should be big enough to get reasonable results, when measuring activities. The activity  $A(t)$  is the time derivation of the number of atoms at a specific time  $t$  and is given by:

$$A(t) = \frac{dN}{dt} = -\lambda_d N(t) \quad (2.31)$$

Within the lifetime  $\tau$  of an isotope the initial number of atoms  $N$  is reduced to  $\frac{1}{e}N$ . The half-life  $t_{1/2}$  of an isotope gives the time interval, where the initial number of atoms is reduced to the half.

$$\frac{1}{e} N_0 = N_0 e^{-\lambda_d \tau} \quad \Rightarrow \quad \tau = \frac{1}{\lambda_d} \quad (2.32)$$

$$\frac{1}{2} N_0 = N_0 e^{-\lambda_d t_{1/2}} \quad \Rightarrow \quad t_{1/2} = \frac{\ln 2}{\lambda_d} \quad (2.33)$$

### 2.2.1 Classification of radioactive decay

**$\alpha$ -decay** is the emission of a  ${}^4\text{He}$ -nucleus. This decay is important for heavy nuclei, the half-lives are often long and the emitted  $\alpha$ 's of a particular decay are monoenergetic. By the emission of the  $\alpha$ -particle, energy is gained. The reaction is the following:



A classical description of the  $\alpha$ -decay is not possible, because the charged  $\alpha$ 's could either not overcome the Coulomb barrier of the nucleus or they would pass it instantaneously if they would have enough energy, which does not match with the long half-lives of the  $\alpha$ -decay. Quantum-mechanically the  $\alpha$ 's can be described as waves which can tunnel through the Coulomb barrier. During this tunneling the amplitude of the wave decreases with  $e^{-G}$ , where G is the Gamow-factor.

**$\beta$ -decay** is based on the weak interaction. In the standard model of particle physics it is described by the exchange of W-bosons. Depending on which gauge boson is exchanged there are two forms of  $\beta$ -decay. During the  $\beta^-$ -decay a neutron decays to a proton, an electron and an electron antineutrino are emitted, while during the  $\beta^+$ -decay a proton decays to a neutron, and a positron and a neutrino are emitted. The first one is exotherm. Free neutrons decay in this way. The latter one can not happen to a free proton, because the Q-value of the reaction is negative. The kinetic energy in the outgoing channel has to be splitted between the electron and antineutrino or positron and neutrino, so there is no sharp line in the energy spectrum of a particular  $\beta$ -decay. Examples for the two  $\beta$ -decays are:



There is also a third possibility of a decay where electrons are involved, the so called electron capture ( $\epsilon$ ). Here an electron from an inner shell is captured by a proton of the nucleus, forming a neutron and emitting a neutrino; e.g.:



The outgoing neutrino is monoenergetic, because it does not have to share its en-

ergy. If an isotope decays by electron capture its half-life may be increased in stellar environments, because at these temperatures the nuclei are highly ionized and there are less electrons which can be captured.

**$\gamma$ -decay** is the deexcitation from a higher energy state of a nucleus to a lower one by emitting a photon. It often follows a nuclear reaction or one of the previous decays, because the produced nuclei are often generated in an excited state. Each  $\gamma$ -decay has its characteristic energy, namely the energy difference between the two states. Examples for radioactive decays, important to this work are given in fig. 2.4 and fig. 2.5.

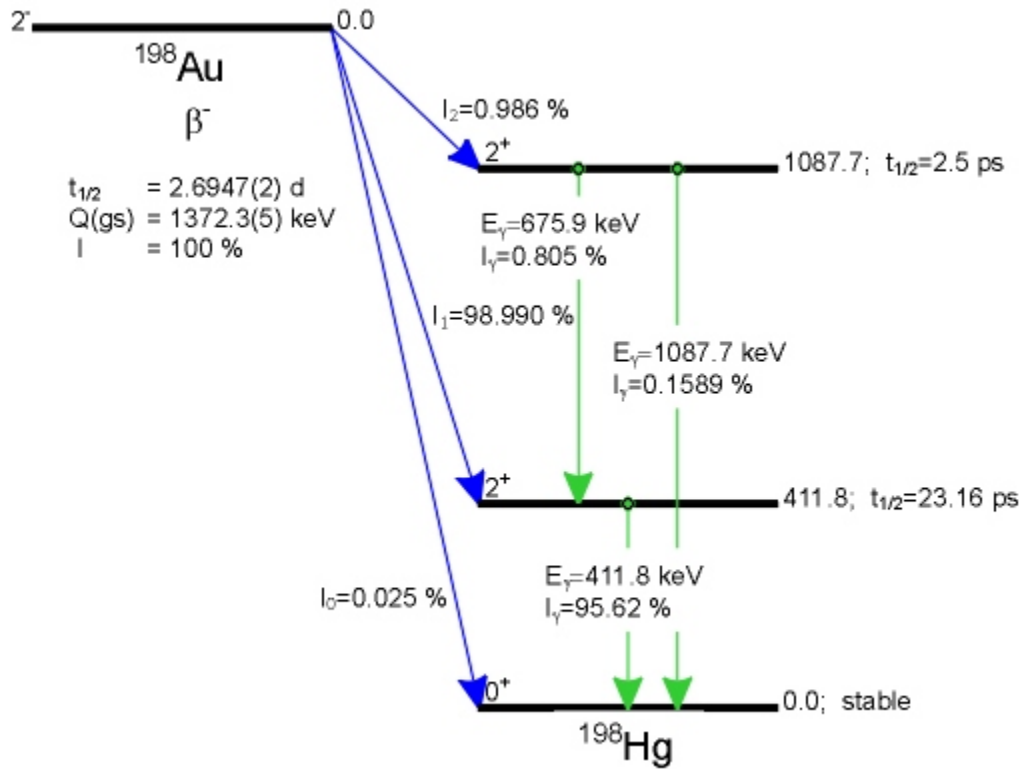


**Figure 2.4:** Decay scheme of  $^{198}\text{Au}$ . The isotope  $^{198}\text{Au}$  decays to the ground state or the first or second excited state of the  $^{198}\text{Hg}$  nucleus. The Q-value to the ground state is  $1372.3 \pm 0.5$  keV. In 98.99 % of the cases  $^{198}\text{Au}$  decays to the first excited state of  $^{198}\text{Hg}$ . Both excited states are very short lived and decay to the lower or to the ground state by emission of a photon with the corresponding energy [Xiaolong, 2009].

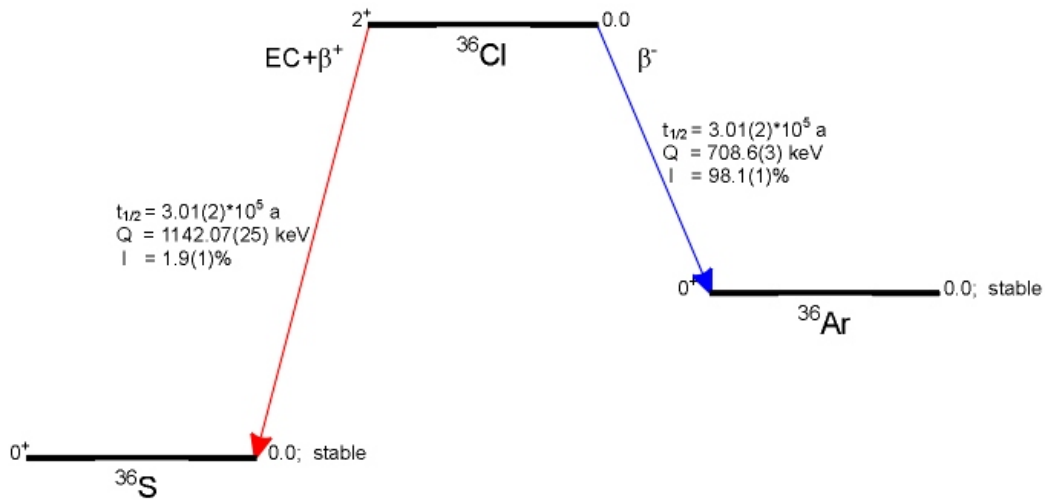


**Figure 2.5:** Decay scheme of  $^{36}\text{Cl}$ . With a probability of 98.1 %  $^{36}\text{Cl}$  decays via  $\beta^-$  decay to the ground state of  $^{36}\text{Ar}$  with a Q-value of  $708.6 \pm 0.3 \text{ keV}$  and in 1.9 % of the cases it decays via electron capture or  $\beta^+$ -decay to the ground state of  $^{36}\text{S}$  with a Q-value of  $1142.07 \pm 25 \text{ keV}$  ([Endt, 1990]).

## 2.3 Interactions of ionizing radiation and matter

### 2.3.1 $\gamma$ 's passing through matter

$\gamma$ -radiation is the high energy end of the electromagnetic spectrum. As mentioned in the previous chapter,  $\gamma$ 's are emitted by the deexcitation of a nucleus. Since Einstein's description of electromagnetic waves (photons), we know that the energy  $E$  of an electromagnetic wave (photon) is proportional to its angular frequency  $\omega$  and its momentum  $p$  is proportional to the inverse wavelength  $1/\lambda$ .

$$E = \hbar\omega \quad (2.38)$$

$$p = \frac{2\pi\hbar}{\lambda} \quad (2.39)$$

Wavelength and angular frequency are connected through the speed of light.

$$c = \frac{\omega\lambda}{2\pi} \quad (2.40)$$

There are three possibilities for interactions of photons with matter (nuclear reactions are not included here). It depends on the energy of the photon which process dominates:

- **Photoelectric effect:** The photon interacts with a bound shell electron of an atom. All of the photons energy is transferred to the electron. It is partly needed

to escape from the Coulomb potential of the atom. The rest is transformed into kinetic energy of the escaping electron. This interaction is dominant for low energy  $\gamma$ 's. The probability for the photoelectric effect reaches its maximum when the energy of the photon matches the binding energy of an electron. Mosley's law [Segré, 1977] gives a good approximation for these binding energies.

$$E_b = 13.605 \frac{(Z - s)^2}{n^2} \quad (2.41)$$

Where  $E_b$  is the binding energy,  $Z$  is the atomic number,  $s$  is the screening constant and depends on the shell of the interacting electron and  $n$  is 1 for the k-shell, 2 for the l-shell and so on. As one can see in equation 2.41, high energy photons like  $\gamma$ 's will most likely match the energy of the k-electrons of heavy elements. The photoelectric effect is highly dependent on the atomic number  $Z$ . Its rate increases with approximately  $Z^5$ . Secondary effects of the photoelectric effect are fluorescent radiation: an electron from a higher shell fills the empty place of the escaped electron and x-rays are emitted. The emission of Auger electrons takes place if these x-rays free another electron from a higher shell.

- **Compton effect:** Photons are scattered on electrons and energy from the photon is partly transferred to the electron. By losing energy the photons frequency decreases and its wavelength increases. From the kinematics of the reaction one can calculate the difference in the wavelength  $\Delta\lambda$  and the transferred energy  $E_e$ .

$$\Delta\lambda = \lambda_c(1 - \cos\vartheta) \quad (2.42)$$

$$E_e = E_\gamma \left(1 - \frac{1}{1 + \frac{\lambda_c}{\lambda}(1 - \cos\vartheta)}\right) \quad (2.43)$$

Here  $\lambda_c = \frac{2\pi\hbar}{m_e c}$  is the Compton wavelength and  $\vartheta$  is the scattering angle.  $E_e$  reaches a maximum if  $\vartheta = \pi$ .

- **Pair production:** In this process the photon is converted into an electron-positron pair. Due to conservation laws this decay can only take place, if there is a third particle involved, which can take the recoil. This reaction has an energy threshold of 1022 keV, which is the sum of the rest masses of the  $e^-$  and  $e^+$ . The kinetic energy of the positron and the electron is given by:

$$E_e = \frac{\hbar\omega - 2m_e c^2 - E_{recoil}}{2} \quad (2.44)$$

The produced positron is stopped in the material and annihilates with an electron, forming two photons of 511 keV which fly in opposite directions. Possible interactions of the electron will be described in the next section. Pair

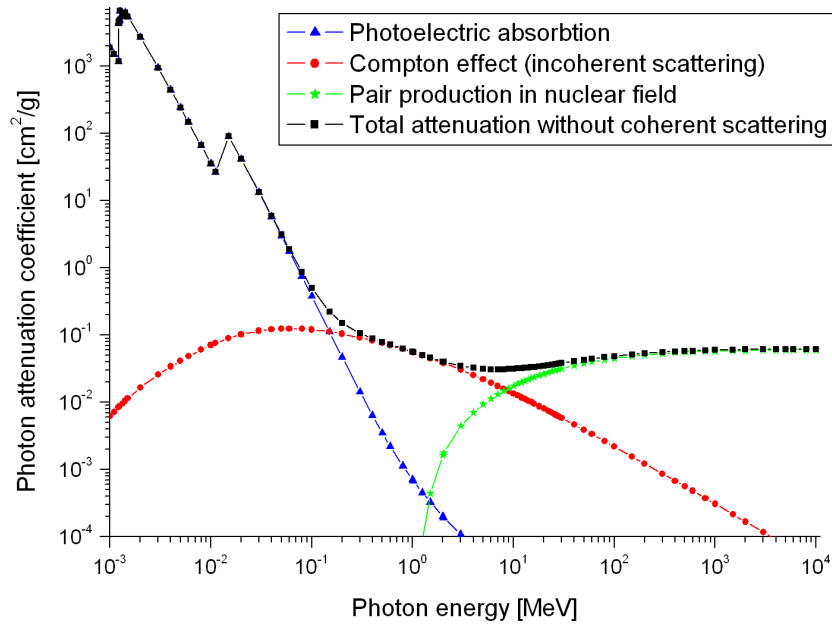


**Figure 2.6:** Photon attenuation coefficients for photon absorption, Compton effect, pair production and the sum of all three reactions in Ge. The data is taken from [Berger *et al.*, 1990]

production is the dominant reaction for high energy  $\gamma$ 's. Its cross-section is proportional to  $Z^2$ .

All of these processes lead to partial or full absorption of photons passing through matter. This attenuation of photon intensity is a statistical process which can be described with an exponential decrease. The probability for the absorption of a photon in an infinitesimal thin layer of material  $dx$  is given by  $\mu dx$ , where  $\mu$  is the attenuation coefficient, which is a material constant. The resulting differential equation can be solved in the same way as the differential equation for the radioactive decay. For the attenuation of a photon beam of initial intensity  $I_0$  one gets:

$$I(x) = I_0 e^{-\mu x} \quad (2.45)$$

### 2.3.2 Heavy charged particles and matter

A beam of heavy charged particles like protons or ions interacts with the surrounding bulk material; energy loss occurs mainly through Rutherford scattering and ionization of the bulk material.

The first one is the elastic scattering on the Coulomb potential of a nucleus of the bulk material. Scattering angles due to this reaction are small. The differential

cross-section  $\frac{d\sigma}{d\omega}$  (cross-section  $\sigma$  for particular solid angle  $\omega$ ) is given by [Segré, 1977](Rutherford scattering cross-section):

$$\frac{d\sigma}{d\omega} = \frac{1}{4} \left( \frac{Zze^2}{mv^2} \right) \frac{1}{\sin^4(\vartheta/2)} \quad (2.46)$$

Here  $Z$  and  $z$  are the charges of the target and the projectile in units of the elemental charge  $e$ .  $m$  and  $v$  are the mass and the velocity of the projectile and  $\vartheta$  is the scattering angle. The above formula is only an approximation, because it does not take into account specific nuclear forces nor quantum and relativistic effects, but it gives very good result if the distance between target and projectile is above a certain value [Segré, 1977].

Ionization of the bulk material atoms is the main source of the energy loss for charged particles passing through matter. Here the particles are inelastically scattered on the shell of an atom, which is ionized during this interaction. One can calculate the energy loss per unit length by the Bethe-Bloch-formula.

$$-\frac{dE}{dx} = \frac{4\pi z^2 e^4}{mv^2} \rho_e \left( \log \frac{2mv^2}{I(1-\beta^2)} - \beta^2 \right) \quad (2.47)$$

Where  $I$  is a material constant,  $\beta = \frac{v}{c}$  is the velocity in units of the speed of light and  $\rho_e$  is the density of electrons, which can be calculated by  $\rho_e = \frac{Z\rho}{m}$ . In the last formula  $\rho$  is the mass density. If the energy loss is plotted versus the penetration depth (length of particle path in material) one gets the Bragg-curve.

The particles loose nearly all of their energy shortly before they are completely stopped (Braggpeak). As already mentioned before, ionization is the dominant energy loss process, although the loss of energy on a single Rutherford scattering event is bigger then on a single ionization event, but ionization occurs much more frequently.

There are some other processes, which also have an influence on the energy loss of charged particles in matter, like polarization and emission of Cherenkov light, for particles which are faster then the speed of light in the medium. For further information see [Segré, 1977].

Due to the fact that neutrons have a magnetic moment they can also interact with the surrounding material through electromagnetic forces, but the cross-sections for these reactions are very small. Neutrons will mostly interact due to the strong or weak forces. They can be elastically or inelastically scattered and they can be captured as it was described in chapter 2.1.

### 2.3.3 Electrons

The interactions of electrons with matter can be summarized as follows:

- Energy loss by ionization is the main component for slow electrons ( $E < 2mc^2$ ). It can be treated similar to the ionization process caused by heavy charged

particles but there are also important differences. *"It is necessary to take into account the identity of the particles involved in the collision and their reduced mass."* [Segré, 1977] Therefore the equation for the stopping power has to be modified. However for slow electrons it gives almost the same values as for heavy charged particles. The stopping power is still proportional to the nuclear charge of the targets and to  $\log(E)$ .

- Energy loss by radiation (Bremsstrahlung) is proportional to the kinetic energy of the moving electrons, and becomes the dominating term for fast electrons ( $E > 2mc^2$ ).
- Annihilation with positrons. After an electron is slowed down to very low energies it can annihilate with a positron from pair production reactions, releasing two photons of 511 keV in opposite directions.



## 3 Nucleosynthesis

In this chapter we will deal with the different burning phases of stars and a short description of the s-process will be given. " *The evolution of stars is initially connected with nuclear reaction networks. It is these networks that determine the rate at which nuclear binding energy is made available to power the star*" [Arnett, 1996, p.93]. To describe these networks in a mathematical formalism, systems of nonlinear differential equations are necessary. The most common reactions in these networks are  $(p,\gamma)$ ,  $(p,n)$ ,  $(p,\alpha)$ ,  $(n,\gamma)$ ,  $(n,\alpha)$ ,  $(\alpha,\gamma)$  and their inverse reactions, but there are also other important reactions with heavier nuclei, like the triple  $\alpha$ -process or the fusion of two  $^{12}\text{C}$  or two  $^{16}\text{O}$  nuclei. The network equations describe the abundance of an isotope via the sum of all possible production rates and all possible decay rates. Further information on the network reaction equations and their solution, applying a steady state or an equilibrium ansatz, can be found in [Arnett, 1996].

### 3.1 Stellar burning phases during hydrostatic equilibrium

Hydrostatic equilibrium means that the gravitational forces in a star exactly compensate the radiative pressure, caused by nuclear fusion processes. Hydrogen nuclei are the first available fuel for nuclear reactions in stars. The burning of hydrogen (single protons) starts at temperatures of  $10^7$  K and core densities of several  $\text{g}/\text{cm}^3$ . All stars spent most of their lives in the H-burning phase. It is also important to notice that massive stars burn their fuel much faster than less massive stars. There are two main reaction paths for hydrogen burning.

- **pp-cycles:** is important for small and cool stars like our sun. The reaction rates are proportional to the fourth power of the temperature [Boyd, 2007]. Three different pp-cycles exist. It depends on the temperature of the star which of the processes is favored. pp-I is the simplest one consisting only of three reactions. The first one is the fusion of two protons to a deuteron  $p(p,\nu_e)d$ . In the next step the d reacts with another p and  $^3\text{He}$  is produced  $d(p,\gamma)^3\text{He}$ . Finally two  $^3\text{He}$  nuclei are fused to  $^4\text{He}$  and two protons are released  $^3\text{He}(^3\text{He},2p)^4\text{He}$ . pp-II and pp-III are more complicated and include nuclear reactions with other light elements as Li, Be and B. The Q-value of 26.73 MeV [Boyd, 2007] is the same for all three reaction chains, but energy losses through neutrinos are different.
- **CNO-cycles:** This is the dominant process in massive hot stars from younger generations, where heavier elements like carbon, nitrogen and oxygen, are used

as catalysts for the fusion of four protons to one He nucleus. Reaction rates are proportional to  $T^{17}$  and the Q-value is the same as in the pp-chain.

In more massive stars other cycles like the NeNa- or the MgAl-cycle are also possible to convert protons to helium.

The next stages in stellar evolution are:

- He-burning
- C-burning
- Ne-burning
- O-burning
- Si-burning

Burning phase	Main products	Secondary products	T [10 <sup>9</sup> K]	t [a]	Main reaction
H	He	<sup>14</sup> N	0.02	10 <sup>7</sup>	pp-cycles, and CNO-cycles
He	C, O	<sup>18</sup> O, <sup>22</sup> Ne	0.2	10 <sup>6</sup>	triple $\alpha$ process , $^{12}\text{C}(\alpha,\gamma)^{16}\text{O}$
C	Ne, Mg	Na	0.8-1.2	10 <sup>3</sup>	$^{12}\text{C}(\text{C},\alpha)^{20}\text{Ne}$ , $^{12}\text{C}(\text{C},\text{n})^{23}\text{Mg}$ , $^{12}\text{C}(\text{C},\text{p})^{23}\text{Na}$
Ne	O, Mg	Al, P	1.2-1.4	3	$^{20}\text{Ne}(\gamma,\alpha)^{16}\text{O}$ , $^{20}\text{Ne}(\alpha,\gamma)^{24}\text{Mg}$
O	Si, S, P	Cl, Si, Ar, K, Ca, Ti, Ce	2	0.8	$^{16}\text{O}(\text{O},\alpha)^{28}\text{Si}$ , $^{16}\text{O}(\text{O},2\text{p})^{30}\text{Si}$ , $^{16}\text{O}(\text{O},\text{n})^{31}\text{S}$ , $^{16}\text{O}(\text{O},\text{d})^{30}\text{P}$ , $^{16}\text{C}(\text{O},\text{p})^{31}\text{P}$
Si	Fe	Co, Ni, Ti, V, Cr	2.7-4	0.02	$^{28}\text{Si}(\gamma,\alpha)^{24}\text{Mg}$ , $^{28}\text{Si}(\gamma,\text{p})^{27}\text{Al}$ , $^{28}\text{Si}(\gamma,\text{n})^{27}\text{Si}$ , $^{24}\text{Mg}(\gamma,\alpha)^{20}\text{Ne}$ , multiple $\alpha$ , p, n captures; radioactive decay finally forms <sup>56</sup> Fe

**Table 3.1:** Burning phases of a 20-25  $M_{\odot}$  star. The data was taken from [Boyd, 2007], [Wallerstein *et al.*, 1997], [Schaller *et al.*, 1992] and [Weaver *et al.*, 1978]

These burning phases only occur if the star is massive enough to provide the needed density and temperature. Our sun for example will stop nucleosynthesis after He-burning. In tab 3.1 the main reactions, the main and the secondary products of the different burning phases for a 20 to 25  $M_{\odot}$  (solar mass) star are summarized.

The data for the table is taken from [Boyd, 2007], [Wallerstein *et al.*, 1997], [Schaller *et al.*, 1992] and [Weaver *et al.*, 1978]. For further information see [Boyd, 2007] and [Wallerstein *et al.*, 1997].

As one can see in tab. 3.1, various nuclides are produced and dissociated in the different burning phases (e.g. chlorine during oxygen burning) until the reaction network reaches equilibrium. The heaviest isotope which is produced via exothermal nucleosynthesis is  $^{56}\text{Fe}$ . It is the nuclide with the highest binding energy per nucleon, so further nucleosynthesis does not provide energy benefit. As one can see in tab. 3.1 the core temperature rises with the change of the fuel, which also means that the temperature of the whole star rises. This leads to the ignition of the shell burning in outer regions of the star. At the end of the equilibrium burning phases, the star, if massive enough, has an onion-like shell structure, with a non burning outer shell followed by a H-, He-, C-, Ne-, O- and Si-burning shell respectively the core will be a dense compound of Ni and Fe [Boyd, 2007].

## 3.2 The s-process

Heavy nuclides beyond Fe cannot be produced in significant amounts by fusion of charged particles and nuclei, because of the increasing Coulomb-barrier with the charge of the nuclei. There are two main processes which are responsible for the production of heavy nuclei. They are called s- and r-process. Both are based on neutron capture reactions and  $\beta^-$ -decays. The names, s stands for slow and r for rapid, refer to the mean capture time for a neutron,  $\tau_n$ .

The s-process takes place in AGB (Asymptotic giant branch) stars (red giants) during He-burning and later burning phases. In the chart of nuclides the s-process follows the valley of stability, because the neutron density in these environments is relatively low (approximately  $10^8$  neutrons/cm<sup>3</sup>). This means that only stable, or very long lived isotopes in the s-process chain capture neutrons. Short-lived nuclei, which may be produced by neutron capture, will all decay before they can capture another neutron. If  $\tau_n \approx \tau_\beta$  (where  $\tau_\beta$  is the lifetime of the produced isotope), both scenarios are possible (branching points in chart of isotopes). Free neutrons are unstable and decay within a half-life of  $t_{1/2} = 10.24(2)$ min [IAEA, 2007-2010] via  $n(e^- \nu_e)p$ , so the neutrons for the s-process have to be constantly produced. There are two possible reaction chains which are responsible for the production.

- $^{22}\text{Ne}(\alpha, n)^{25}\text{Mg}$  [Wallerstein *et al.*, 1997] is the historically favored n-source.  $^{22}\text{Ne}$  can be produced directly by  $\alpha$ -capture and  $\beta^+$ -decay in the following reaction chain:  $^{14}\text{N}(\alpha, \gamma)^{18}\text{F}(e^+ \nu)^{18}\text{O}(\alpha, \gamma)^{22}\text{Ne}$ . The  $^{14}\text{N}$  comes from the stars H-burning shell and is mixed with the He from the core, during the so called dredge up phases of the star. Due to the high Z the reaction needs a temperature of  $2\text{-}3 \cdot 10^8$  K [Wallerstein *et al.*, 1997].

- $^{13}\text{C}(\alpha, n)^{16}\text{O}$  occurs at temperatures around  $10^8$  K.  $^{13}\text{C}$  could be produced via  $^{12}\text{C}(p, \gamma)^{13}\text{N}(e^+ \nu)^{13}\text{C}$ . The problem of this mechanism is that two mixing processes are necessary.  $^{12}\text{C}$  from the He-burning zone has to be mixed into the H-burning shell (dredge up) and afterwards  $^{13}\text{C}$  has to be mixed back into the He-burning zone [Wallerstein *et al.*, 1997].

Nowadays a common theory is that both reactions are responsible for neutron production but in different environments and different isotopic regions of the s-process [Wallerstein *et al.*, 1997]. In stellar environments the neutrons thermalize very quickly by scattering processes, and their energies are Maxwell-Boltzmann distributed. Typically, the temperature in the cores of massive Red giants is about  $3 \cdot 10^8$  K. This temperature gives a Maxwellian neutron-energy distribution with a most probable energy of 25 keV.

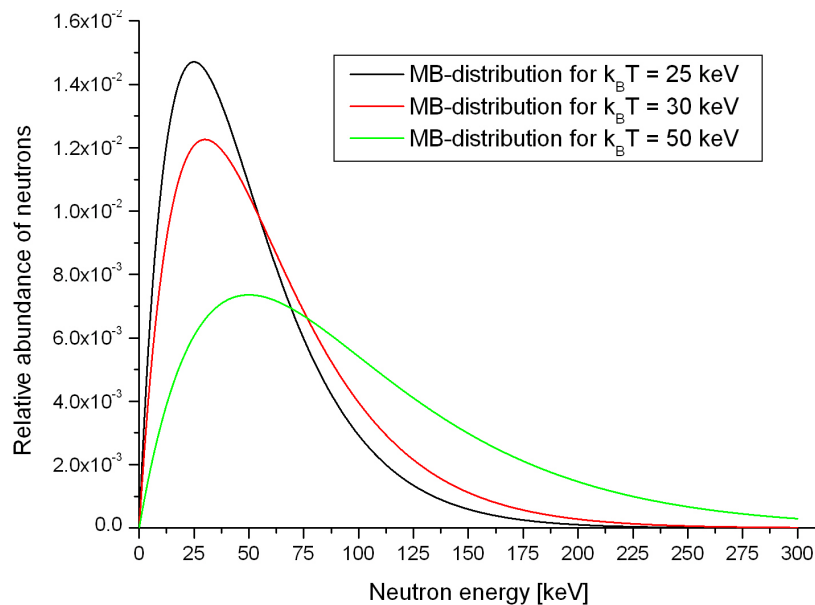


**Figure 3.1:** Relative abundances of neutrons under certain temperature conditions.  $k_B = 8.617343(15) \cdot 10^{-5}$  eV K $^{-1}$  [NIST, 2009] is the Boltzmann constant and T is the Temperature. 25 keV equates approximately  $2.9 \cdot 10^8$ , which is the core temperature of 20-25  $M_\odot$  stars.

The s-process can be divided into three components:

- **Weak component:** Responsible for the production of elements with  $56 \leq A \leq 90$ . It occurs in stars with more than eight  $M_\odot$ . The neutrons are mainly produced via  $^{22}\text{Ne}(\alpha, n)^{25}\text{Mg}$  at  $T \approx 3 \cdot 10^8$  K. Neutron densities are about  $10^6$  cm $^{-3}$ .
- **Main component:** At lower temperatures of  $T \approx 9 \cdot 10^7$  K elements with  $90 \leq A \leq 204$  are produced. The main source of the neutrons is the  $^{13}\text{C}(\alpha, n)^{16}\text{O}$

reaction, but neutrons are also produced via  $^{22}\text{Ne}(\alpha, n)^{25}\text{Mg}$ . Neutron densities are about  $10^7 \text{ cm}^{-3}$ .

- **Strong component:** This component is only postulated and should explain the high abundances of  $^{208}\text{Pb}$  and  $^{209}\text{Bi}$ .

Some isotopes which are lighter than  $^{56}\text{Fe}$  also have relatively high neutron capture cross-sections. These isotopes, e.g.  $^{35}\text{Cl}$ , disturb the production of isotopes with higher A, because they consume neutrons and act as so-called neutron poisons .

For reasons of completeness some facts about the r-process should also be mentioned. The r-process occurs during explosive scenarios, like supernovas or colliding neutron stars and leads to the production of the isotopes far away from the valley of stability. It also produces the heavy elements above Bi. Neutron densities can reach values of  $10^{21} \text{ cm}^{-3}$ . It should also be mentioned that other processes like the p-, or rp-process, which are responsible for the production of p-rich nuclei exist. The information in this chapter was taken from [Wallerstein *et al.*, 1997] and [Boyd, 2007].

### 3.3 Production of $^{36}\text{Cl}$ on Earth

In the atmosphere  $^{36}\text{Cl}$  is produced through various spallation reactions of the isotopes  $^{36,40}\text{Ar}$  by cosmic rays and their secondary particles [Tikhomirov & Blinov, 2009]. At Earth's surface and in the subsurface  $^{36}\text{Cl}$  is mainly produced by n-capture on  $^{35}\text{Cl}$  [Elmore *et al.*, 1979]. The neutron sources for this reactions are the cosmic radiation and natural radioactive isotopes. In the last 60 years the common presence of chlorine in water and minerals lead to a significant increase of the  $^{36}\text{Cl}$  amount in the atmosphere and in the oceans due to nuclear weapon tests and nuclear reactors [Hou *et al.*, 2007], which use water as moderator and coolant. Measurements of surface soil [Milton *et al.*, 1994] and water [Seki *et al.*, 2007] in the area of nuclear facilities show increased  $^{36}\text{Cl}/\text{Cl}$  ratios.

Neutrons produced by fission have energies in the region of several MeV. A fission-neutron energy spectrum can be approximated through a MB-spectrum of several MeV. These fast neutrons are decelerated (thermalized) by the moderator (water, graphite etc.) of the reactor. This leads to neutron energy spectra which cover a range from meV up to MeV.  $^{36}\text{Cl}$ , like many other isotopes is produced as a byproduct of these neutrons.

The most common reaction for the  $^{36}\text{Cl}$  production in fission reactors is the n-capture on  $^{35}\text{Cl}$ , and this reaction is dominated by the thermal neutrons, but as described in section 5.3, also the epithermal part of the neutron-spectrum contributes to the production of  $^{36}\text{Cl}$ . For the calculation of the production rates of  $^{36}\text{Cl}$  by neutron capturing in reactors the cross-section over the above mentioned energy range has to be known.

Production rates of such important radioactive byproducts of nuclear fission as  $^{36}\text{Cl}$  must be considered for the storage of radioactive waste. Also the storage of

radioactive waste itself can produce  $^{36}\text{Cl}$ , by activating the minerals in the rock, which surrounds the storage. The importance of  $^{36}\text{Cl}$  for nuclear waste management lies in its long half-life, and the high mobility of chlorine in the environment [Hou *et al.*, 2007].

## 4 AMS - Accelerator mass spectrometry

In the first part of this chapter a general overview of the AMS technique and the problems of AMS measurements will be given and in the second part the setup of the VERA-facility (Vienna Environmental Research Accelerator) and the problems of measuring  $^{36}\text{Cl}$  will be discussed.

### 4.1 Basics of AMS

#### 4.1.1 The method

Accelerator mass spectrometry is a sensitive technique to measure low isotopic ratios. The rare isotopes of interest are separated with different electromagnetic filters, an accelerator and different detectors [Litherland, 1984]. Additionally, also chemical properties, chemical reactions or lasers can be used to increase the sensitivity of the isotope separation [Litherland, 1980]. Normally the rare isotope of interest is measured relative to a stable isotope of the same element. The current of the stable isotopes is measured by Faraday cups and the rare isotopes are counted with particle detectors. For normalization and background corrections, standard material with known isotopic ratios and blank material, which undergo the same treatment as the samples is used.

In contrast to the determination of isotopic abundances of radioactive isotopes by activity measurements, AMS does not depend on secondary particles produced during the decay, because the isotopes of interest are counted directly. The advantage of this technique is, that radioisotopes with long half-lives and also stable isotopes can be measured, keeping the measurement time and sample size conventional (some mg). Compared to mass spectrometry, AMS has the advantage that molecules of the same mass as the isotopes of interest are split apart in the accelerator and do not contribute to the background. Isotopic ratios in the order of  $10^{-16}$  can be measured.

#### 4.1.2 The technique

In this section the main components of an AMS-facility will be discussed.

- **Ion source:** In the ion source either positive or negative atoms and molecules of the sample material are produced e.g. via thermal (heating) or mechanical (sputtering) reactions. Ion currents should be relatively high (several  $\mu\text{A}$ ) to reduce measuring times of rare isotopes [Litherland, 1984]. A negative ion source also works as the first filter due to the fact that some elements like the

noble gases or nitrogen do not form negative ions. The ions are extracted from the source with an appropriate high voltage.

- **Electrostatic filters:** An electrostatic filter (ESA - electrostatic analyzer) is a plate capacitor, circularly bended for a certain angle. By applying a voltage  $U$  to the plates, a homogeneous electric field  $|\vec{\mathcal{E}}| = \mathcal{E} \propto U$  forms. Charged particles with the charge  $q$  crossing this field are deflected by the Lorentz-force  $\vec{F}_L$ :

$$\vec{F}_L = q(\vec{\mathcal{E}} + (\vec{v} \times \vec{\mathcal{B}})) \quad (4.1)$$

Where  $\vec{v}$  is the velocity of the particle and  $\vec{\mathcal{B}}$  is the magnetic field which is not used here. According to Newton's third law this force equals the centrifugal force  $F_Z = |\vec{F}_Z|$  on the charged particles:

$$F_L = F_Z \quad (4.2)$$

$$q\mathcal{E} = \frac{mv^2}{r} \quad (4.3)$$

Where  $m$  is the mass of the particle and  $r$  is the radius of the particles path. This equation can be transformed to:

$$\mathcal{E}r = 2\frac{E}{q} \quad (4.4)$$

The product  $\mathcal{E}r$  is called electric rigidity, which only depends on the energy to charge ratio  $E/q$ . The radius of the ESA (electrostatic analyzer) is fixed so one can select particles with a certain  $E/q$  by applying a certain voltage to the plates of the ESA. Only this particles will pass the ESA on the predetermined path. Particles with other energy to charge ratios will be filtered.

- **Magnetic filters:** The working principle of a magnetic filter is similar to those of an electrostatic filter. These electromagnets bend the particle beam by a homogeneous magnetic field, which can be controlled by the applied voltage. Magnetic filters are sensitive to the momentum to charge ratio as can be derived using equations 4.1 and 4.2 setting the electric field 0.

$$\mathcal{B}r = \frac{p}{q} = \frac{\sqrt{2Em}}{q} \quad (4.5)$$

The product  $\mathcal{B}r$  is called magnetic rigidity. By applying a certain magnetic field to the magnets one can select particles with a certain  $p/q$  ratio. It is often necessary to measure particles with different electric and magnetic rigidity in short intervals. Electric fields change very quick after changing the voltage,

but magnetic fields do not. Multi beam switcher (MBS) can be used to avoid changing the magnetic field. The fast changing electric fields of these devices accelerate or decelerate particles so that different particles have the right magnetic rigidity to pass the bending magnet.

- **Accelerators:** Since the invention of the first particle accelerators in the 1930's great progress in this field was made, and the maximum resulting energy of the particles was pushed for orders of magnitude [Wilson, 2001]. Nevertheless, the principal idea of accelerating particles did not change. It is also based on the Lorentz force. Charged particles are accelerated by an electric field which is caused by a potential difference between two electrodes of the accelerator. Traveling through this field the particles gain energy proportional to the potential difference  $\Delta U$  and their charge  $q$ .

$$E = q\Delta U \quad (4.6)$$

Generally, accelerators can be divided into two classes, linear accelerators, where the particles pass each potential difference only once and circular accelerators, where the particles move on circular or helical paths passing the same potential difference several times. This is clearly an advantage of the circular accelerators. Their disadvantage is that the charged particles have to be forced on the circular path. If one wants to accelerate particles to higher energies the strength or the radius of the bending magnets has to be increased according to equation 4.5. Further criteria for the classification of accelerators are the way how the potential difference is achieved (Van de Graaff-, Cockcroft-Walton-, Wideröe-accelerators) or the different technique to accelerate different particles (Betatron) [Conte, 2008], [Wilson, 2001].

In AMS accelerators are used for two main purposes:

1. **To get rid of molecular isobars.** The ions are accelerated to energies of some MeV, fly through a volume of gas or a thin foil and collide with the atoms of the gas or the foil. In this so-called stripping process the ions lose several of their outer electrons (depending on the gas pressure or the thickness of the foil) and molecules are dissociated in their atomic components, because molecules with a charge state  $q \geq +3$  are not stable. The advantage of foil stripping is that foils are more effective in producing high charge states [Wittkower & Ryding, 1971] and that the vacuum in the accelerator tube is not degraded by residual gas as in the case of gas stripping. The advantage of gas stripping is that the medium is "indestructible" [Litherland, 1984].
2. **To achieve better separation of the isotope of interest from its atomic isobar** in the particle detectors on the high energy side of the spectrometer. The best separation can be achieved if the atoms are completely stripped as it is the case in very high energy heavy ion accelerators

with particle velocities  $v \gg \frac{Z}{137}c$  [Litherland, 1984]. Where  $Z$  is the atomic number and  $c$  is the speed of light.

The accelerator can be seen as another filter, which separates the isotope of interest from its isobaric molecule background. Cyclotrons additionally separate ions with the right  $M/q$  ratio due to:

$$\frac{1}{f} = \frac{2\pi M}{\mathcal{B} q} \quad (4.7)$$

Where  $f$  is the frequency of the cyclotron (inverse of the time, which is needed by the isotope of interest for one cycle).

- **Velocity filters:** These filters (Wien filter) separate particles by orthogonal magnetic and electric fields. To pass the filter on a linear path the Lorentz-force resulting from the sum of the electric and magnetic force on the particle has to be 0.

$$F_L = 0 = q(\mathcal{E} + v\mathcal{B}) \quad (4.8)$$

The vector character of  $\vec{v}$ ,  $\vec{\mathcal{E}}$  and  $\vec{\mathcal{B}}$  can be neglected because in this case they are all orthogonal to each other. By inserting equations 4.4 and 4.5 into equation 4.8 and algebraic transformations one gets:

$$v^2 = 2\frac{E}{m} \quad (4.9)$$

This filter is sensitive to the  $E/m$  ratio of the particles. If the particles do not have the predetermined velocity the magnetic and electric force are not in equilibrium and the particles are deflected.

For a more detailed look on the mathematical formalism of the different filters see [Conte, 2008], [Wilson, 2001].

- **Beam optics and analysis:**
  - **steerer:** These are parallel plate capacitors which are used to correct the direction of the ion beams, by electric fields of variable strength.
  - **slits:** Slits are used to get a narrow and sharp beam profile, which is needed during the tuning of the machine, to optimize the yield for the isotopes of interest.
  - **Faraday cups:** Metallic cups applied to an electrical potential. Charged particles hitting the cup cause a drop of the potential which is proportional to the current of the charged particles and can be measured.
  - **Magnetic and electrostatic quadrupoles:** These are used for beam focusing. They must be used in pairs (two magnetic quadrupoles or two

electric quadrupoles), where the second one is tilted  $90^\circ$  against the first one, because a single quadrupole always focuses the beam in one axis but defocuses it in the other axis. The focusing effect is stronger than the defocussing effect.

- **Einzel lenses:** Einzel lenses effect the path of charged particles by the electric fields between three or more cylindrical or rectangular tubes and focus the beam without changing its energy.
- **beam profile monitors:** A beam profile monitor consists of a rotating helical wire, which scans the beam in x- and y-direction during each rotation and measures the current in each position. So the cross-section (profile) of the beam can be visualized.
- **Detectors:** Detectors are the final filters for AMS. The basic requirement of a detector is to measure properties of incoming particles like energy, velocity, or position and / or simply count the incoming particles. This is achieved by measuring currents of secondary electrons produced during the interaction of the beam with the detector material. Different detectors types for measuring these properties exist. Examples are ionization chambers, semiconductor detectors (surface barrier detectors), foil-detectors. By measuring these properties also atomic isobars can be separated in some cases.

## 4.2 AMS at VERA

The **V**ienna **E**nvironmental **R**esearch **A**ccelerator (VERA) is a facility for AMS at the University of Vienna, based on a 3-MV pelletron tandem accelerator (see chapter 4.2.3) built by National Electronics Corporation in Wisconsin, USA [Vockenhuber *et al.*, 2003]. The machine was installed in 1995 and after test runs became operational in 1996 [Kutschera *et al.*, 1997]. It is used for the two main purposes of a university, education and research and its primary mission is the tracing of long-lived radionuclides in our environment [Kutschera *et al.*, 1997]. Additionally to astrophysical and nuclear research programmes, as related to this work, it is mainly used for archeology (scientific and commercial  $^{14}\text{C}$ -dating), paleoclimatology ( $^{10}\text{B}$ -measurements), atmospheric science, environmental studies, nuclear safeguards and new technical developments. VERA was continuously upgraded (high-energy ESA and several new detectors) and is now, in addition to AMS experiments [Kutschera *et al.*, 1997] also capable of PIXE- (Proton Induced X-ray Emission) and PIGE-measurements (Proton Induced Gamma-ray Emission).

In the following the main components of VERA used for my measurements will be discussed.

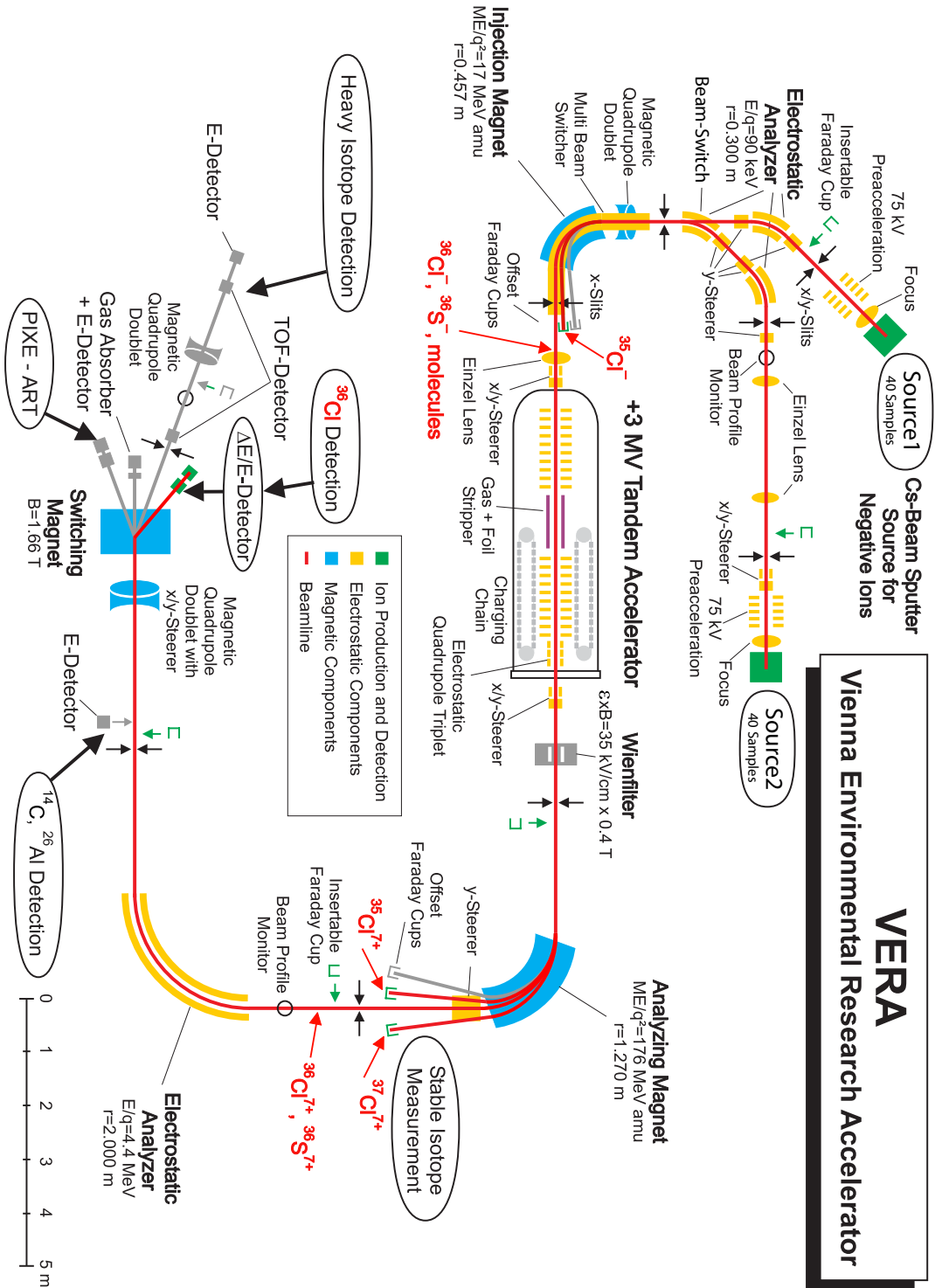


Figure 4.1: Schematic view of VERA. Setup for chlorine measurements (©Martschini).

### 4.2.1 Ion source

VERA uses a multiple in-vacuum cathode cesium sputter ion source build by NEC (type MC-SNICS) [Ferry, 1993], which produces negative ions of the target material (source S1). A second ion source was installed at VERA, to reduce the time used for switching between different isotopes [Priller *et al.*, 2010]. This source was never used for Cl-measurements. The target wheel can be equipped with up to 40 target cathodes (solid samples), so one can switch between multiple targets automatically and very quickly (i.e. without breaking the vacuum in the source). Normally target wheels and cathodes (target holders) are made of Al or Cu. For the Cl-measurements special copper cathodes, larger than the cathodes normally used, which can carry more sample material and a corresponding target wheel were designed and manufactured in-house by the VERA workshop. A detailed description of the targets can be found in chapter 6.2.

By heating cesium gas on a hot tantalum anode, the so called ionizer, the Cs atoms are ionized. (Cs is a good choice for the sputter gas because its ionizing energy is low.) The  $Cs^+$  ions are accelerated and focused onto the samples by an electrical potential difference between the tantalum anode and the target cathodes. This Cs beam sputters and ionizes the target material. The ionization is additionally favored by Cs condensing on the cooled surface of the samples. A positive high voltage extracts the negative ions from the source. Normally, the negative ion current from the source is in the order of some  $\mu A$  but the ionization efficiency and the ion current strongly depend on the electron affinity of the target material. Some elements like the noble gases do not form negative ions and can not be extracted from negative ion sources. Other elements like the halogens are ionized very easily. Chlorine and sulfur both have a high electron affinity. Additionally the  $Cl^-$  ions have the ability to sputter the target material itself as well. In the beginning of the Cl-AMS-measurements at VERA this lead to  $^{35}Cl^-$  currents of over 100  $\mu A$  and eventually sample melting. The problem was solved by controlling the cesium source output by the ionizer power automatically [Steier *et al.*, 2010].

### 4.2.2 Low-energy side

The injector side or the low-energy side of VERA consists of the low-energy ESA (electrostatic analyzer), the injection magnet and some focusing and beam analysis devices. The  $45^\circ$  ESA (or the two ESA with  $45^\circ$  from the second source, see fig. 4.1) have a nominal bending radius of 300 mm and can provide a maximal electric field strength of 6 kV/cm (for more information see [Priller *et al.*, 2010]), resulting in a maximal electric rigidity of  $\mathcal{E}r = 180$  kV and a maximal  $E_{low}/q$  ratio of 90 kV (see equ. 4.4) for the ions [Vockenhuber *et al.*, 2003]. Here  $E_{low}$  is the energy of the ion after pre-acceleration and  $q$  is the charge of the ion, normally -1 elemental charge. The ESA cuts off the tail of the particle energy distribution after the source and due to its spherical electrodes focuses in both directions [Vockenhuber *et al.*, 2003].

The second filter on the low-energy side is the  $90^\circ$  injector magnet, with a radius

of 457 mm and a maximal magnetic field of 1.31 T, resulting in a magnetic rigidity of  $\mathcal{B}r = 0.598$  Tm and according to equ. 4.5, maximal  $\frac{m_{low}E_{low}}{q^2}$  product of 17 amuMV/e [Vockenhuber *et al.*, 2003], where  $m_{low}$  is the mass of the ion on the low-energy side. In front of the bending magnet there are an electrostatic y-steerer and a magnetic quadrupole doublet for ion-optical beam corrections [Vockenhuber *et al.*, 2003]. After the energy selection by the ESA, the injector magnet selects the ions by mass for charge state -1.

Two offset Faraday cups are installed after the bending magnet to measure ion currents of interest on the low-energy side. In our case, the current for stable  $^{35}\text{Cl}^-$  ions was recorded.

For fast sequencing of ions of different mass, the injector magnet is equipped with a **multi beam switcher** (MBS), which can provide an additional accelerating voltage of 0-13 kV to the ions to give them the right magnetic rigidity to pass the bending magnet [Vockenhuber *et al.*, 2003]. After the magnet the ions are decelerated again. At VERA we can quickly (<1ms) switch between four different MBS voltages. The advantage of this method is that one can measure different isotopes on the high-energy side, which is needed to determine the transmission (see chapter 7.1.1) and isotopic ratios, without changing the magnetic field of the injector magnet.

Slits in x-direction (horizontal) and an insertable Faraday cup after the injector magnet are used to tune and optimize the beam at the low-energy side. In front of the accelerator there is an Einzel lens and a pair of steerers (x- and y-direction (vertical)) for focusing and corrections of the beam direction.

### 4.2.3 Accelerator

The VERA-facility consists of a tandem accelerator of the pelletron type. A tandem accelerator is an accelerator where the endpoints are on ground potential and the terminal in the middle of the accelerator is on a high positive potential. In case of VERA the maximal nominal terminal voltage is +3 MV. The terminal is charged by two chains which continuously transport electrons from the terminal (with maximal 230  $\mu\text{A}$ ) [Vockenhuber *et al.*, 2003]. A corona probe and a generating voltmeter are used for stabilizing the terminal voltage [Vockenhuber *et al.*, 2003]. The accelerator tube is mounted inside a vessel filled with  $\text{SF}_6$  (electrical isolation) to avoid electrical discharges from the terminal to the walls of the vessel. Permanent magnets around the accelerator tube and a lead shield suppress the emitted radiation to a level not significantly above the background [Priller *et al.*, 1997].

The positive high voltage at the terminal accelerates the negative ions towards the stripper. In the stripper the ions loose electrons and gain positive charge. By this process molecules are dissociated. At VERA, a gas-filled ( $\text{O}_2$ ) channel with a few  $\mu\text{bar}$  pressure, controlled by differential pumping with turbo pumps on both sides of the channel (gas stripping), or thin foils can be used as stripper (foil stripping). The combination of both strippers is also possible. For the Cl measurements thin carbon foils ( $2.6 \mu\text{g}/\text{cm}^2$ ) were used [Maier-Komor *et al.*, 1997], because foil stripping

provides a higher ionization yield for highly charged states (in our case  $^{36}\text{Cl}^{7+}$ ) [Steier *et al.*, 2005]. The high positive charge state is needed for a better separation of  $^{36}\text{Cl}^{7+}$  and its isobar  $^{36}\text{S}^{7+}$  in the detector. After the stripper the positive ions are again accelerated by the same voltage towards the end of the accelerator. After this acceleration the ions have an energy of:

$$E_{high} = (E_{low} + eU_T) \frac{m_{high}}{m_{low}} + qeU_T \quad (4.10)$$

Where  $m_{high}$  is the mass of the ion after stripping,  $U_T$  the terminal voltage and  $e$  is the elemental charge.

The charge states of the ions after the stripper are distributed. The distribution among the charge states depends on the cross-section for the loss of electrons and for recombination, on the energy of the ions and also on the pressure of the stripping gas or the thickness of the stripping foil. It also depends on these parameters if charge state equilibrium is achieved [Steier *et al.*, 2005]. No molecules survive if  $q \geq 3$  is selected.

#### 4.2.4 High-energy side

The components of the analyzer or high-energy side are a Wien-filter, which was not used for the Cl-measurements, an analyzing magnet, a high-energy ESA, a switching magnet, some ion-optical elements and several different detectors.

The analyzing magnet is a double focusing  $90^\circ$  bending magnet with a radius of 1.27 m and a maximal magnetic field strength of 1.53 T. This gives a magnetic rigidity of 1.94 Tm, or a maximal  $\frac{m_{high}E_{high}}{q^2}$  of 176 amuMV/e [Vockenhuber *et al.*, 2003]. A certain charge state can be selected by adjusting the magnetic field of the analyzing magnet. Molecular fragments and different charge states are filtered out. The remaining background are isobars in the selected charge state and ions which incidentally have the same magnetic rigidity.

Three offset Faraday cups mounted after the bending magnet are used to measure the currents of stable isotopes during fast sequencing (see chapter 7). In the case of Cl-measurements these were the  $^{35}\text{Cl}^{7+}$  and the  $^{37}\text{Cl}^{7+}$  currents.

The  $90^\circ$  high-energy side ESA, build by Danfysik, removes the isotopes with the right magnetic rigidity but a wrong  $E_{high}/q$  ratio. With a radius of 2.0 m and a maximal electric field strength of 4.4 MV/m, ions with a maximal  $E_{high}/q$  ratio of 4.4 MV can pass the ESA [Vockenhuber *et al.*, 2003]. The ESA focuses the beam in horizontal and vertical direction by its spherical electrodes [Vockenhuber *et al.*, 2003]. Background passing this filter are atomic isobars and ions that have undergone multiple charge changes and scattering so that they have passed all the filters in the right way. For the separation of these background, dedicated detectors are used [Vockenhuber *et al.*, 2003].

It is necessary to use different detectors for the different isotopes measured at VERA. Therefore, a switching magnet with a maximal magnetic field strength of 1.66 T was installed after the high-energy ESA, which can direct the ion beam to four

different beam lines where different detector systems can be mounted. The  $-20^\circ$  beam line is used for AMS- and PIXE measurements, the  $0^\circ$  beam line is equipped with a gas absorber cell and an energy sensitive detector and can be used for measurement of  $^{10}\text{Be}$ . The  $+20^\circ$  beam line is used for the identification and separation of heavy ions. It is equipped with a time-of-flight setup and an ionization chamber. Finally the  $+40^\circ$  beam line, featuring an ionization chamber and a silicon strip detector is used for AMS measurements where isobaric suppression is important, e.g. Cl-measurements.

### 4.2.5 Detector system

A combination of a split-anode ionization chamber and a silicon strip detector was used for the separation of  $^{36}\text{Cl}$  and its stable isobar  $^{36}\text{S}$ . These detectors are described in this section.

The split-anode ionization chamber is a gas-filled metal box with a cathode and a split anode constructed by [Forstner *et al.*, 2008], based on a design from ETH Zürich [Döbeli *et al.*, 2004], [Stocker *et al.*, 2005]. Charged particles entering the chamber through a thin silicon nitride foil (SiN-foil) of 50 nm thickness continuously lose energy through interactions with the counting gas (see section 2.3.2). The energy loss, mainly caused by ionization of the counting gas, depends on the atomic number of the ions and on the energy of the particles as can be seen from the Bethe-Bloch equation (see equ. 2.47), so it varies for different elements.

The number of produced electron-ion pairs is proportional to the energy loss. The applied high voltage avoids the recombination of the electrons and ions and accelerates them to the corresponding electrode. If the incoming particles are completely stopped in the split-anode ionization chamber one gets two energy signals for each incoming particle. The first one is the energy loss in the area covered by the first anode ( $\Delta E$ ), the second one is the residual energy which is lost in the area covered by the second anode ( $E_{res}$ ). In the case of Cl and S, the ions were not completely stopped, so we obtained two energy loss signals  $\Delta E_1$  and  $\Delta E_2$ . The residual energy was then measured with a subsequent silicon strip detector. These energy signals are then processed by the detector electronics and can be plotted in two-dimensional energy spectra, where one can separate the  $^{36}\text{Cl}$  and  $^{36}\text{S}$  events by their different energy losses and their residual energy deposited in the silicon strip detector (see chapter 7.2.1).

The double sided (n- and p-doped side) silicon strip detector is a semi-conducting detector. Semi-conducting detectors consist of a p- and a n-doped layer. By applying a voltage between the two layers (positive pole on n-side, negative pole on p-side) a depletion layer (electrons and holes recombine) forms on the p-n-junction. Ions hitting this layer create a number of electron hole pairs, proportional to their energy. The electrons are collected by the anode and the cathode collects the positive holes. The measured current is proportional to the energy of the incident ion.

Our double-sided silicon strip detector consists of 16 stripes on each side. The p- and n-doped side are rotated  $90^\circ$  against each other, which gives a detection area

with 256 pixels. The stripes have the dimension  $50 \times 3 \text{ mm}^2$ , the whole detector has a total sensitive area of  $50 \times 50 \text{ mm}^2$  [Orlowski *et al.*, 2010]. This detector geometry, additionally to the residual energy signal, provides two position signals (vertical and horizontal) for each incoming ion.

During the final tuning of the machine, which was performed with an attenuated  $^{36}\text{S}$  beam (see chapter 7.1.1) a silicon surface barrier detector was also used to check the particle count-rate before allowing the  $^{36}\text{S}$ -beam hit the strip detector, to avoid possible damage by a too high count-rate. The signals from all detectors are processed by the detector electronics (see chapter 7.1.3).



## 5 Neutron irradiations and activity measurements

The first experimental part of this thesis was the irradiation of NaCl pellets with cold, thermal and epithermal neutrons at three different facilities. At the Atominstitut der österreichischen Universitäten in Vienna (ATI) (see section 5.2.1) and at the Budapest Research Reactor (BRR) (see section 5.2.2) of the Hungarian Academy of Science we irradiated the samples which served as reference material, and at the Karlsruhe Institute of Technology, samples for the determination of the MACS for  $^{35}\text{Cl}(n,\gamma)^{36}\text{Cl}$  were irradiated prior to this work (see 5.2.3). In order to determine the neutron fluence (see equ. 5.35 and 5.37), gold in form of gold powder homogeneously mixed into the pellets and gold foils attached to them were used. Gold is a common neutron fluence monitor because it has only one stable isotope ( $^{197}\text{Au}$ ) and its thermal neutron capture  $\sigma_{^{197}\text{Au}(n,\gamma)^{198}\text{Au}}=98.65(9)$  b [Mughabghab, 1981] and the half-life of  $^{198}\text{Au}$ , ( $t_{1/2}(^{198}\text{Au})=2.69517(21)$  d [NNDC, 2005]) are both very well-known. The reaction  $^{197}\text{Au}(n,\gamma)^{198}\text{Au}$  is listed as a neutron standard for thermal energies. In the following the thermal neutron capture cross-section of  $^{197}\text{Au}$  will be written as  $\sigma_{Au}$ , the thermal neutron capture cross-section of  $^{35}\text{Cl}$  as  $\sigma_{Cl}$  and the decay constant of  $^{198}\text{Au}$  will be written as  $\lambda_{Au}$ .

### 5.1 Production of the NaCl-pellets

Altogether 13 NaCl pellets with different masses were prepared during this work. Three pellets BUD3, KIT1 and KIT2 were produced at the KIT (Karlsruhe Institute of Technology), the other 10 samples were pressed at VERA by myself. Two of the pellets ATI1 and ATI4 were broken during the production procedure. For the measurement of the neutron fluence all these samples were "equipped" with gold foils on their front- and backside. In seven samples gold powder mixed into the pellets was used as additional fluence monitor.

In general, the pellets were produced in the following way: A certain amount of NaCl powder (listed in tab. 5.1, Alfa Aesar, Sodium chloride, puratronic, with a purity of 99.999%, Art# 10862) was weighted with a Sartorius scale. The powder was put into a mortar and optionally a certain amount of gold powder (Alfa Aesar, gold powder, spherical, -325mesh 99.9% purity, Art# 43900, listed in tab. 5.1) was added. The powders were homogeneously mixed in the mortar and then pressed to pellets of 6 mm diameter with a sample press, which was constructed at the VERA workshop in course of another project, e.g. the production of iron pellets [Buczak,

2009]. The press consists of a short stamp, a long stamp (both 6 mm in diameter), a matrix (with a 6 mm aperture), a metal ring and three supporting metal cylinders in two different forms (a small one and two large cylinders)(see fig. 5.1. The outer matrix is made of carbid and the inner matrix is made of MACOR (Machinable Glass Ceramic) [Buczak, 2009]. At first the short stamp was inserted into the matrix, then the powder was added and the long stamp was inserted from the other side. The small supporting cylinder was mounted under the short stamp and on both side a large supporting cylinder was mounted (see fig. 5.2). By applying a pressure of some  $t/cm^2$  with a hydraulic press, the (NaCl+Au)-powder was pressed into pellets of 6 mm diameter. Then the support cylinders and the short stamp were removed and a metal ring was placed onto the inner matrix. With the help of the hydraulic press and the long stamp, the pellet was carefully removed from the matrix [Buczak, 2009] (see fig.5.1, 5.2, 5.3) .

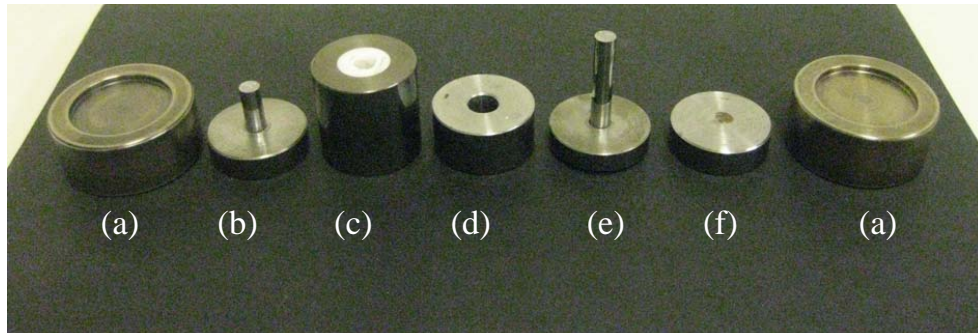


**Figure 5.1:** Components of the press used for the production of the NaCl pellets. The picture shows: the large supporting metal cylinders (a), the short stamp (b), the matrix (c), the metal ring (d), the long stamp (e) and the small supporting metal cylinder (f).

The pellets were weighted again and the mass of the NaCl and Au powder was calculated with the assumption, that the relative loss of the pellet mass equals the relative loss of the NaCl- and Au-mass. Losses during the pressing were in the range



**Figure 5.2:** Mounted sample press.



**Figure 5.3:** Pressed NaCl+Au-pellet.

of 2-16 % of the powder mass, with highest losses when pressing the thinnest pellets (difference between  $M_{pow}$  and  $m_{pel}$  in tab. 5.1).

$$\frac{M_{pow}}{m_{pel}} = \frac{M_{Au}}{m_{Au}} = \frac{M_{NaCl}}{m_{NaCl}} \quad (5.1)$$

where  $M_{pow}$  is the sum of the masses of the NaCl and Au powder,  $m_{pel}$  is the weighted mass of the pellet,  $M_{Au}$  and  $M_{NaCl}$  are the weighted masses of the Au and NaCl powder prior the pressing and  $m_{Au}$  and  $m_{NaCl}$  are the calculated masses of the gold and the sodium chloride after the mixing and pressing process (see tab. 5.1).

Sample	$M_{NaCl}$ [mg]	$M_{Au}$ [mg]	$M_{pow}$ [mg]	$m_{pel}$ [mg]	$m_{NaCl}$ [mg]	$m_{Au}$ [mg]
ATI1 broken	-	-	-	-	-	-
ATI2	-	-	-	43.16±0.01	43.16±0.01	-
ATI3	-	-	-	22.41±0.01	43.16±0.01	-
BUD1	50.70±0.01	9.74±0.01	60.44±0.01	59.03±0.01	49.51±0.02	9.51±0.01
BUD2	50.29±0.01	10.48±0.01	60.77±0.01	57.93±0.01	47.94±0.02	9.99±0.01
BUD3	82.67±0.01	-	-	82.65±0.01	82.65±0.01	-
KIT1	-	-	-	46.1±0.05	46.1±0.05	-
KIT2	-	-	-	46.1±0.05	46.1±0.05	-
ATI4 broken	25.42±0.01	9.20±0.01	34.62±0.01	31.25±0.01	22.95±0.01	9.51±0.01
ATI5	51.67±0.01	9.77±0.01	61.44±0.01	59.03±0.01	49.64±0.02	9.19±0.01
ATI6	52.56±0.01	10.16±0.01	62.72±0.01	58.38±0.01	48.92±0.02	9.45±0.01
ATI7	102.12±0.01	10.52±0.01	112.64±0.01	107.39±0.01	97.36±0.02	10.03±0.01
ATI8	26.78±0.01	9.54±0.01	36.32±0.01	30.21±0.01	22.27±0.01	7.93±0.01

**Table 5.1:** Overview of the masses of the NaCl pellets.

Here ATI1 to ATI8, BUD1 to BUD3 and KIT1 and KIT2 denote the (NaCl+Au)-pellet. After attaching gold foils to the samples, the whole sample stack was labeled with the same notation.

The first 3 samples (ATI1, ATI2, ATI3) were pressed with a pressure of 2.5 t/cm<sup>2</sup>. During this process the pellet ATI1 was broken. After pressing, gold foils (0.2-0.5 g/mm<sup>2</sup>, see tab. 5.2) were fixed onto the pellets with a tape. All the other ATI samples and the samples BUD1 and BUD2 were pressed with 5 t/cm<sup>2</sup>.

In the case of the BUD samples a gold foil, the sample and another gold foil (see tab. 5.2) were hold together with Al rings and were fixed with tape (see fig. 5.5). For the samples ATI2, ATI3, ATI5, ATI6, ATI7 and ATI8 only tape was used to fix the gold foils onto the pellets (see fig. 5.4). Sample ATI9, consisted of four gold (no NaCl powder) foils placed in an Al-holder and fixed with an elastic plastic ring (see fig. 5.6, see section 5.2.1). This sample was used to compare the neutron fluence measured by the outer foils with the fluence measured by the inner foils (see section 5.2.1).

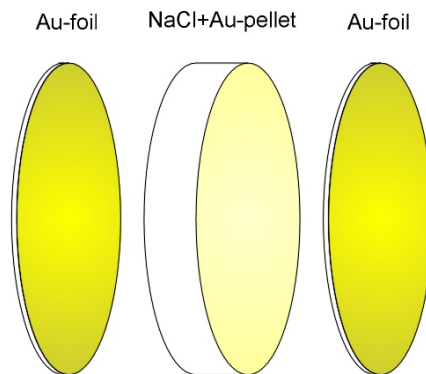


**Figure 5.4:** Schematic view of samples ATI2,3,5,6,7,8. The gold foils were attached to the pellet with tape. In case of ATI2 and ATI3 one of the foils was not circular.

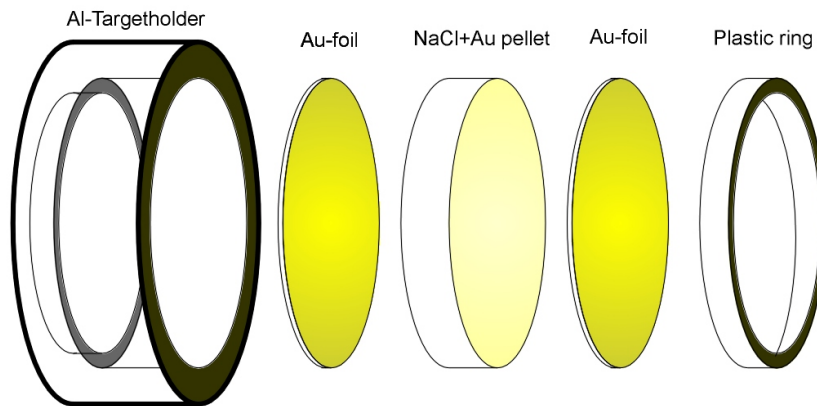


**Figure 5.5:** Schematic view of samples BUD1,2,3. The sample and the gold foils were mounted into the Al-holder and fixed with an elastic plastic ring and/or with tape.

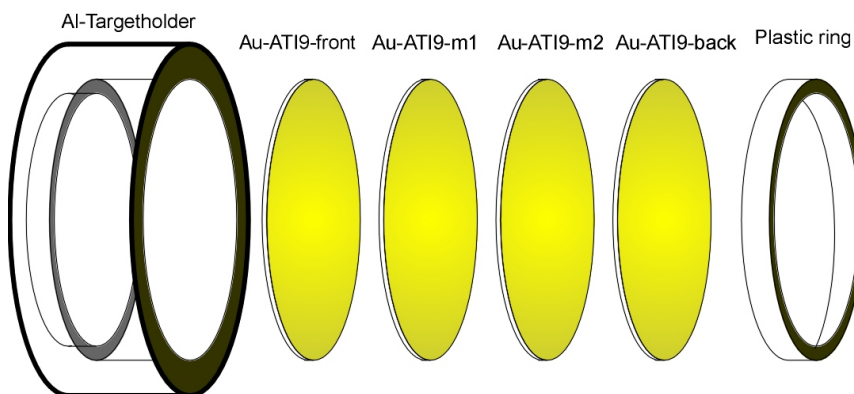


**Figure 5.6:** Schematic view of sample ATI9. The four gold foils were mounted into the Al-holder and fixed with an elastic plastic ring.

Foil	$m_{Au}$ [mg]	Comment
Au-ATI2-f	15.11(1)	
Au-ATI2-b	3.81(1)	irregular form
Au-ATI3-f	3.52(1)	irregular form
Au-ATI3-b	15.12(1)	
Au-BUD1-f	14.89(1)	
Au-BUD1-b	14.74(1)	
Au-BUD2-f	7.02(1)	
Au-BUD2-b	6.15(1)	
Au-BUD3-f	15.11(1)	
Au-BUD3-b	14.92(1)	
Au-KIT1-f	14.53(15)	
Au-KIT1-b	14.50(15)	
Au-230	11.68(12)	double-sandwich front
Au-KIT2-f1	11.47(11)	double-sandwich middle
Au-KIT2-b1	10.09(10)	double-sandwich back
Au-227	14.57(15)	double-sandwich front
Au-KIT2-f2	14.64(15)	double-sandwich middle
Au-KIT2-b2	14.85(15)	double-sandwich back
Au-234	16.44(16)	double-sandwich front
Au-KIT2-f3	16.21(16)	double-sandwich middle
Au-KIT2-b3	16.77(17)	double-sandwich back
Au-301	11.63(12)	double-sandwich front
Au-KIT2-f4	11.39(11)	double-sandwich middle
Au-KIT2-b4	11.35(11)	double-sandwich back
Au-ATI5-f	14.86(1)	
Au-ATI5-b	14.94(1)	
Au-ATI6-f	15.20(1)	
Au-ATI6-b	14.82(1)	
Au-ATI7-f	15.37(1)	
Au-ATI7-b	15.25(1)	
Au-ATI8-f	15.35(1)	
Au-ATI8-b	15.31(1)	
Au-ATI9-f	15.30(1)	independent sample
Au-ATI9-m1	14.73(1)	independent sample
Au-ATI9-m2	6.22(1)	independent sample
Au-ATI9-b	15.45(1)	independent sample

**Table 5.2:** Masses of the gold foils used as neutron fluence monitors during the neutron irradiations, f denotes front foils, m foils in the middle of a sample stack and b back foils. The comment "irregular" form means that the foils were not circular. Double-sandwich means that the foils were used during an irradiation, where two samples were irradiated in a stack (front foil, sample1, middle foil, sample2, back foil). The last four foils were not attached to a NaCl-sample, but were irradiated as an independent sample stack in the configuration Au-ATI9-front, Au-ATI9-m1, Au-ATI9-m2, Au-ATI9-back.

For the foils used in the irradiations at the Atominstitut, the labeling, f (front)

and b (back) do not indicate the real position, because the samples were not fixed during the irradiation and the positions of the foils relative to the reactor core were random.

## 5.2 Irradiations of NaCl-pellets

### 5.2.1 Irradiations at the ATI

The information given in this section was taken from [ATI, 2009]. The TRIGA (Training Research Isotope General Atomic) Mark-II Reactor is a reactor of the swimming pool type, installed by General Atomic in the years 1959-1962. It has a nominal maximum continuous thermal power output of 250 kW and consists of 80 fuel elements (8% uranium, 1% hydrogen and 91% zirconium by weight). The zirconium-hydrogen is the main moderator for the nuclear chain reaction. This material has a negative temperature coefficient, which means that the material moderates worse with rising temperature. Distilled and deionized water is used as coolant. With three control rods, which use boron-carbide as neutron absorber, the power output of the reactor can be sensitively regulated in the range of 5 mW - 250 kW. Two of the control rods are driven by electro motors and are able to shut down the reactor within 0.1 s. The third one can be shot in and out (duration a few ms) pneumatically with a pressure of 5 bar. An antimony-beryllium photoneutron source provides the neutrons to start the nuclear fission reaction [ATI, 2009]. In order to fulfill its goals as a research reactor the facility is equipped with several irradiation devices [ATI, 2009]. The NaCl samples for this work (ATI2 to ATI8) and the gold sample ATI9 were irradiated in one of the five reflector irradiations tubes (Weberrohr) at the outer region of the reactor core. The neutron flux in the central irradiation tube is about  $10^{13} \text{ cm}^{-2}\text{s}^{-1}$  and decreases to a value of approximately  $10^{12} \text{ cm}^{-2}\text{s}^{-1}$  at our irradiation position (for maximal power output) [ATI, 2009]. The neutron flux  $\phi$  is proportional to the power output of the reactor  $P$ .

$$\phi \propto P \tag{5.2}$$

The isotopic ratio of AMS-reference material has to be in the right order of magnitude. Within this work the  $^{36}\text{Cl}/^{35}\text{Cl}$ -ratio should be in the order of  $10^{-12}$ . This value is high enough to get AMS results with sufficient statistics in reasonable time and low enough to not overload the silicon detectors with high count-rates and to avoid cross-contamination of "real" samples in the ion source during AMS measurements (see chapter 7.2). According to equ. 2.4 the number of produced  $^{36}\text{Cl}$ -atoms is proportional to the neutron fluence and the number of  $^{35}\text{Cl}$ -atoms in the target. Assuming a constant neutron flux  $\phi$  this equation can be written as:

$$\frac{^{36}\text{Cl}}{^{35}\text{Cl}} = \sigma_{Cl}\Phi = \sigma_{Cl}\phi t_I \tag{5.3}$$

Where  $\sigma_{Cl} = 43.6(4) \text{ b}$  [Mughabghab, 1981] is the well-known thermal neutron

capture cross-section value for  $^{35}\text{Cl}$  and  $t_I$  is the irradiation time. Due to the long half-life of  $^{36}\text{Cl}$  the decay of  $^{36}\text{Cl}$  during the irradiation is negligible. Combining equations 5.2 and 5.3 one can see that by choosing the right power output and irradiation time one can obtain the right isotopic ratio in the sample. For an isotopic ratio of approximately  $5 \cdot 10^{-12}$  we choose a power output of 2 kW ( $\phi = 3.8 \cdot 10^9 \text{ cm}^{-2}\text{s}^{-1}$ ) and an irradiation time of 30 s.

This setting of the parameters also satisfied the second requirement on the samples, namely that the activity of the gold foils and the gold powder is in the right order of magnitude. With the thermal neutron capture cross-section for  $^{197}\text{Au}$   $\sigma_{Au} = 98.65(9)$  b [Mughabghab, 1981] and the decay constant of  $^{198}\text{Au}$ ,  $\lambda_{Au} = 2.97663(23)10^{-6}\text{s}^{-1}$  [NNDC, 2005] one can estimate (no corrections) the activity A of the gold foils after the irradiation by:

$$A = \lambda N_{198} = \lambda N_{197} \sigma_{Au} \Phi = \lambda \frac{m_{Au}}{m_{mol(Au)}} N_A \sigma_{Au} \Phi \quad (5.4)$$

With  $N_{197}$  and  $N_{198}$  being the number of  $^{197}\text{Au}$  and  $^{198}\text{Au}$  atoms,  $m_{Au}$  being the mass of the gold foils or the mass of gold powder,  $m_{mol(Au)} = 196.97 \text{ g/mol}$  [Magill *et al.*, 2006] being the molar mass of  $^{197}\text{Au}$ , and  $N_A = 6.0221 \cdot 10^{23}$  [Mohr *et al.*, 2008] being Avogadro's constant. After a 30 s irradiation in the reactor at 2 kW one should get gold activity values from 400 - 1600 Bq for the different samples. This assures count-rates which can be easily handled by the Ge-detector used for activity measurements.

The experimental procedure was the following: At first the power output of the reactor was set to 2 kW by positioning the control rods. An Eppendorf micro-test tube containing one sample was put in a plastic container and was let down into the reflector irradiation tube on a line. After approximately 30 s of irradiation, the reactor was shut down with the control rods (SCRAMed) for ATI2 and ATI3. ATI2 and ATI3 were irradiated on April, 4<sup>th</sup> 2009 one after the other. The other five ATI samples were irradiated on June, 17<sup>th</sup> 2010 at once. These samples were taken out of the reactor without "SCRAMing" it. All samples were transported to the VERA laboratory in a shielding Pb-container, and the activity of the gold foils and the gold powder in the pellets was measured with a high purity Ge-diode from the decay of  $^{198}\text{Au}$  (see chapter 2.31).

The advantage of the irradiations at ATI was that the irradiations were very short, easily accessible, because of the short distance to VERA, and the experimental arrangement was very simple. The disadvantage was that the neutrons have a broad energy distribution. Thermal neutrons ( $E_n \approx 25 \text{ meV}$ ) build the main fraction of the neutron spectrum, but there is also a significant epithermal background. The spectral distribution during the irradiations is not sufficiently known. This leads to difficulties in the determination of the exact neutron fluence (see 5.3.2).

Sample	$t_I$ [s]	End of irradiation
ATI2	30	04.04.2009, 11:28
ATI3	30	04.04.2009, 11:35
ATI5	30	17.06.2010, 09:21:19
ATI6	30	17.06.2010, 09:21:19
ATI7	30	17.06.2010, 09:21:19
ATI8	30	17.06.2010, 09:21:19
ATI9	30	17.06.2010, 09:21:19

**Table 5.3:** Irradiation of the ATI samples. The end of the irradiation is important for the calculation of the waiting time between the irradiation and the activity measurement. Here ATI2 to ATI8 label the whole 6 sample stacks ((NaCl+Au)-pellet and attached Au foils) and ATI9 labels the whole stack of four gold foils.

## 5.2.2 Irradiations at the BRR

To avoid the problems with a neutron energy distribution extending into the epithermal energy range, three samples were irradiated at the **B**udapest **R**esearch **R**eactor. This tank-type reactor is operational since 1959 and is light-water moderated [Tözsér, 2009]. After several upgrades it now has a maximum power output of 10 MW [Tözsér, 2009]. The thermal neutron flux in the core is about  $2.5 \cdot 10^{14} \text{ cm}^{-2}\text{s}^{-1}$  [Tözsér, 2009]. Twelve research stations are currently operational around the reactor [Tözsér, 2009].

The irradiations of the samples BUD1, BUD2 and BUD3 were performed at the PGAA (**P**rompt **G**amma **A**ctivation **A**nalysis) irradiation position (see fig. 5.7), which is normally used for the detection and analysis of prompt gammas after the capture of neutrons. This station was installed at the end of a neutron guide line at about 30 m distance from the reactor and got operational in 1996 [Molnár *et al.*, 1997]. The neutron guidelines are made of boron silicate glass covered with natural Ni and guide the neutrons by total reflection [Molnár *et al.*, 1997]. If the incident angle of the neutron-beam (wave-front) is smaller than the critical angle, total reflexion will occur. The critical angle is energy dependent and the geometry of the beam line strongly favors cold neutrons of a certain energy ( $E_n \approx 5 \text{ meV}$ ,  $v_n \approx 950 \text{ ms}^{-1}$ ). The neutron capture cross-section of both,  $^{35}\text{Cl}$  and  $^{197}\text{Au}$  does not have any resonances in this energy region and for both isotopes, it follow the  $\frac{1}{v}$ -law (see section 2.1.1). This allowed us to use the thermal neutron capture cross-sections of  $^{35}\text{Cl}$  and  $^{197}\text{Au}$  also for "cold neutron energies" because the proportionality factor between the cross-section for cold neutrons and thermal neutrons is equal for  $^{35}\text{Cl}$  and  $^{197}\text{Au}$  and cancels. After an upgrade in 2007, where the last section of the neutron guide line was changed by super mirror elements the thermal equivalent neutron flux at the PGAA station is in the range of  $10^{10} \text{ cm}^{-2}\text{s}^{-1}$  [Szentmiklósi *et al.*, 2010].

For estimating the irradiation time, the  $^{36}\text{Cl}/^{35}\text{Cl}$ -ratio to be obtained once again was  $5 \cdot 10^{-12}$ . With  $4 \cdot 10^{10} \text{ cm}^{-2}\text{s}^{-1}$  for the neutron flux at the PGAA station, I calculated an irradiation time of approximately 2800 s, nearly 100 times as long as

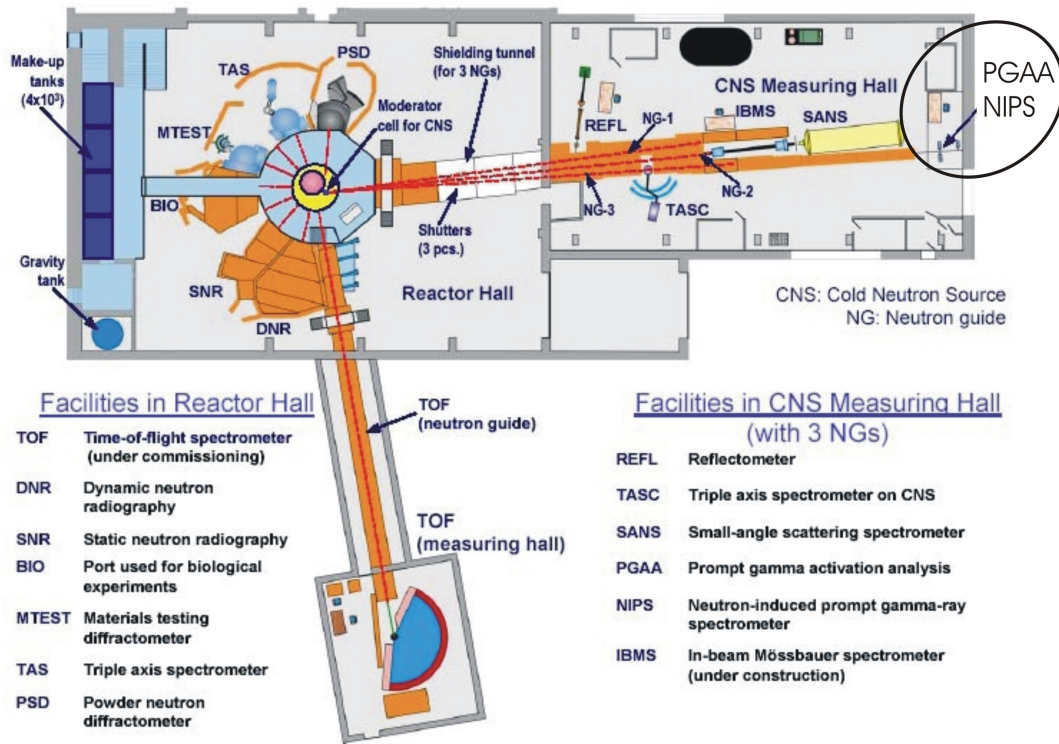


**Figure 5.7:** Scheme of the Budapest Research Reactor (BRR) taken from [Buczak, 2009] original from <http://www.kfki.hu/brr/indexen.htm>. The irradiations for this work were performed at the PGAA station of the NG-3 beamline.

the irradiations at ATI.

For the irradiations the samples, fixed in Al sample-holders, were packed into sealed teflon bags. These bags were placed to the irradiation position and were hold by teflon strings mounted in an aluminum framework. The holder was positioned perpendicular to the beam at the PGAA station.

Sample	$t_I$ [s]	End of irradiation
BUD1	2392	14.12.2009, 10:58:06
BUD2	2418	14.12.2009, 13:10:04
BUD3	2400	14.12.2009, 14:54:27

**Table 5.4:** Irradiation of the BUD samples. Here BUD1 to BUD3 label the whole stack ((NaCl+Au)-pellet and attached gold foils).

The labels f and b (see tab 5.2) of the gold foils indicate the position of the particular foil relative to the incoming neutron beam. In chapter 2.31 one can see that the fluence measured by the front foils is clearly higher than the fluence measured by the back foils.

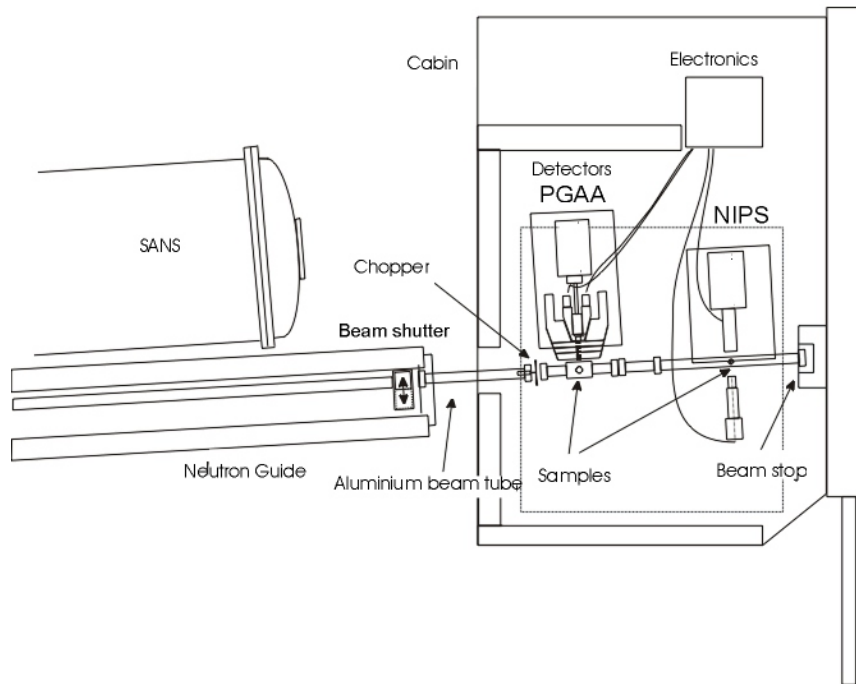


**Figure 5.8:** Schematic view of the NIPS and PGAA stations at BRR, taken from <http://www.bnc.hu/modules.php?name=News&file=article&sid=4>.

### 5.2.3 Irradiations at the KIT

At the Karlsruhe Institute of Technology neutron spectra of a quasi Maxwell-Boltzmann-distribution can be generated. For the determination of MACS it is necessary to either measure differential cross-sections (cross-sections for different neutron energies are measured separately) and calculate the mean over the Maxwell-Boltzmann distribution, or to irradiate the samples directly with a Maxwellian neutron spectrum. In the first case it is essential to measure all resonances in the energy range of the neutron distribution, whereas in the second case calculated values of differential cross-sections are used for weighting the experimentally deduced cross-section (see equ. 2.26, 2.27 and 2.28). We followed the second method. The irradiations of the samples for the determination of the MACS of  $^{35}\text{Cl}$ , with a quasi Maxwellian neutron-energy spectrum of 25 keV took place at the KIT.

The neutron spectrum was produced by bombarding a Lithium target (metallic Lithium for KIT1 and LiF for KIT2) with 1.912 MeV protons accelerated by a 3.7 MV Van de Graaff accelerator. This is just above the energy threshold of the reaction  $^7\text{Li}(p,n)$ . The produced neutrons have energies up to 114 keV and are collimated kinematically in a forward cone with an opening angle of  $120^\circ$ . This was a standard procedure at the KIT for a series of measurements across the chart of nuclides and is

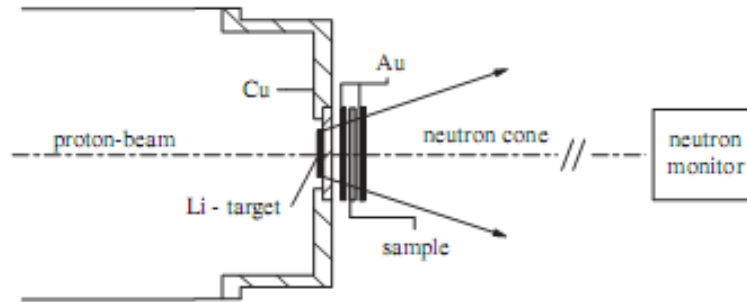


**Figure 5.9:** Schematic view of the irradiation assembly at KIT. Neutrons produced via the  ${}^7\text{Li}(p,n)$  reaction are kinematically collimated in a  $120^\circ$  forward cone. The gold foils are used as neutron fluence monitors. Figure taken from [Reifarth *et al.*, 2009].

described in [Beer & Käppeler, 1980] or [Dillmann *et al.*, 2009]. KIT1 was irradiated in one session as a single sample and KIT2 was irradiated together with a nickel-sample in a double-sandwich-stack in four sessions and two different distances from the neutron source. Details on the irradiations can be found in tab. 5.5 and fig. 5.9.

Sample	Au-foils	Distance to Li-target [mm]	$t_I$ [s]	Start of irradiation	End of irradiation
KIT1	Au-KIT1-f Au-KIT1-b	1.7	43218	05.04.2007, 16:30	10.04.2007, 16:30
KIT2	Au-KIT2-f1 Au-KIT2-b1	3.0	32778	20.07.2007, 15:02	24.07.2007, 10:05
KIT2	Au-KIT2-f2 Au-KIT2-b2	2.7	33282	24.07.2007, 14:51	28.07.2007, 11:18
KIT2	Au-KIT2-f3 Au-KIT2-b3	2.7	8028	28.07.2007, 13:59	29.07.2007, 12:17
KIT2	Au-KIT2-f4 Au-KIT2-b4	2.7	15594	29.07.2007, 14:20	31.07.2007, 09:39

**Table 5.5:** Irradiation of the KIT samples. Here KIT1 and KIT2 labels the whole sample stack (NaCl-pellet and attached gold foils, f denotes front foils and b back foils). Sample KIT2 was irradiated, together with a nickel sample in the back position of a double sandwich (sample order Au-Ni-Au-NaCl-Au) in four separate sessions where the gold monitor foils were changed. The distance between the Li-target and the NaCl sample was also changed between the first and the second irradiation session.

The energy distribution of the neutrons, produced during the bombardment of the lithium-targets was calculated by the Monte Carlo code PINO (Protons In Neutrons Out) [Reifarth *et al.*, 2009], considering the geometrical setup of the experiment and the energy-distribution of the protons after the acceleration. The program is accessible at <http://141.2.245.217/pino/>.

### 5.3 Activity measurements

An excited  $^{198}\text{Hg}$  nucleus is the result of the  $\beta^-$ -decay of  $^{198}\text{Au}$  (see fig. 2.4), which is produced by neutron capture on  $^{197}\text{Au}$ . With an absolute intensity of 95.62(6) % [Xiaolong, 2009] the  $^{198}\text{Hg}$  deexcites by emitting a single  $\gamma$  with an energy of 411.80205(17) keV ([Xiaolong, 2009]). These photons were counted to determine the activity of the irradiated gold.

The activity measurements were carried out with a high purity Ge-detector at the VERA-laboratory, for the activations with thermal and cold neutrons, whereas the activity of the gold foils irradiated in Karlsruhe was measured there. At VERA the gold foils were positioned on a plastic sample holder in 4 cm distance to the active area of the Ge-detector. The detector is shielded by lead to reduce background.

The incident photons may interact with the detector material by one of the three reactions described in section 2.3, transferring their energy to the so-produced electrons. These electrons produce secondary electron-hole pairs. The number of produced electron-hole pairs is proportional to the energy of the primary electrons. The signal caused by the electron-hole pairs in the detector is amplified (pre-amplifier and amplifier), digitized, with an ADC (**A**nalog to **D**igital **C**onverter) and measured by a MCA (**M**ulti **C**hannel **A**nalyzer). A typical spectrum, can be found in fig. 5.10 .

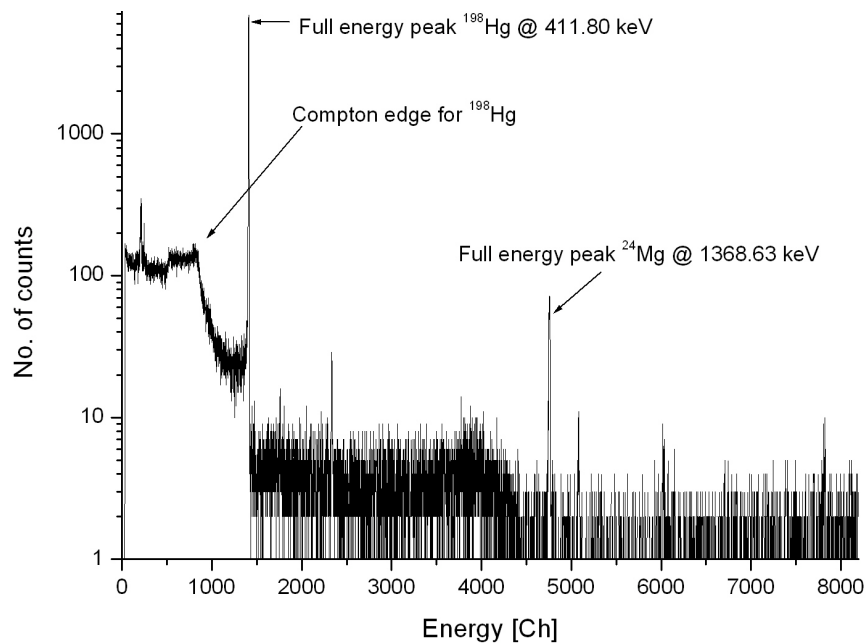


**Figure 5.10:** Typical spectrum of an irradiated (NaCl+Au)-pellet (BUD1) recorded with a Ge-detector. The full energy peaks of the photons from the reactions  $^{198}\text{Au} \xrightarrow{\beta^-} ^{198}\text{Hg}^* \xrightarrow{\gamma} ^{198}\text{Hg}$  and  $^{24}\text{Na} \xrightarrow{\beta^-} ^{24}\text{Mg}^* \xrightarrow{\gamma} ^{24}\text{Mg}$  can be clearly seen.

### 5.3.1 Calculation of the activity and the neutron fluence

The program WIRUKplus (Friedmann, private communication) was used to analyze the spectra (see 5.10). The bins (regions of interest) were defined at peak-maximum $\pm 2.5$  FWHM (Full-Width Half-Maximum). The measured count-rate  $c$  was determined by:

$$c = \frac{C}{t_M} \quad (5.5)$$

By taking into account the efficiency and the intensity of the 411.80 keV Hg  $\gamma$ -line one gets the measured activity of  $^{198}\text{Au}$ :

$$A = \frac{C}{t_M \varepsilon_{412} I_{412}} \quad (5.6)$$

With the activity one can calculate the number of produced  $^{198}\text{Au}$  nuclei:

$$N_{198} = \lambda_{Au} \frac{C}{t_M \varepsilon_{Au} I_{412}} \quad (5.7)$$

The number of  $^{197}\text{Au}$  nuclei can be calculated from the mass of the gold sample:

$$N_{197} = \frac{m_{Au}}{m_{mol(Au)}} N_A \quad (5.8)$$

Combining equations 2.4, 5.7, and 5.8 one gets

$$\Phi = \frac{m_{mol(Au)}}{m_{Au} N_A} \lambda_{Au} \frac{1}{\sigma_{Au}} \frac{C}{t_M \varepsilon_{412} I_{412}} \quad (5.9)$$

for the neutron fluence determined from the gold activity, where no (decay-, self attenuation- and dead time-) corrections were taken into account. This equation can be adapted for the the gold powder samples, mixed into the NaCl pellets by inserting equ. 5.1:

$$\Phi = \frac{m_{mol(Au)} M_{pow}}{M_{Au} m_{pel} N_A} \lambda_{Au} \frac{1}{\sigma_{Au}} \frac{C}{t_M \varepsilon_{412} I_{412}} \quad (5.10)$$

#### Correction factors

To determine the true value of the neutron fluence several correction factors have to be taken into account. These are the dead time correction, corrections for decaying nuclei during the irradiation time, the waiting time and the measurement, and the correction for self absorption in the foils and pellets.

- **Dead-time correction:** After every registered event the detector-software needs a certain time ( $t_{dead}$ ) to process the event data. In this time no other events can be measured. This time is called dead time. The total dead time during a measurement is then:

Constant	Value	Unit	Comment	Source
d <sub>412</sub>	3.729(18)		offset of efficiency-curve at 411.80 keV (see fig. 5.14)	calculated from [Wagner, 1991]
d <sub>1369</sub>	7.179(41)		offset of efficiency-curve at 1368.63 keV (see fig. 5.14)	calculated from [Wagner, 1991]
I <sub>412</sub>	9.562(6)*10 <sup>-1</sup>		intensity of the <sup>198</sup> Hg $\gamma$ -line at 411.80 keV	[Xiaolong, 2009]
I <sub>1369</sub>	9.99936(15)*10 <sup>-1</sup>		intensity of the <sup>24</sup> Mg $\gamma$ -line at 1368.63 keV	[Firestone, 2007]
k			integration constant	
k <sub>412</sub>	1.556(8)	cm <sup>-1</sup>	slope of efficiency-curve at 411.80 keV (see fig. 5.14)	calculated from [Wagner, 1991]
k <sub>1369</sub>	2.806(16)	cm <sup>-1</sup>	slope of efficiency-curve at 1368.63 keV (see fig. 5.14)	calculated from [Wagner, 1991]
$\lambda_{Au}$	2.97663(23)*10 <sup>-6</sup>	s <sup>-1</sup>	decay constant of <sup>198</sup> Au	[NNDG, 2005]
$\lambda_{Na}$	1.2839(10)*10 <sup>-5</sup>	s <sup>-1</sup>	decay constant of <sup>24</sup> Na	[NNDG, 2005]
m <sub>mol(Au)</sub>	1.9697*10 <sup>5</sup>	mg mol <sup>-1</sup>	molar mass of Au	[Magill <i>et al.</i> , 2006]
m <sub>mol(Cl)</sub>	3.545*10 <sup>4</sup>	mg mol <sup>-1</sup>	molar mass of Cl	[Magill <i>et al.</i> , 2006]
m <sub>mol(Na)</sub>	2.299*10 <sup>4</sup>	mg mol <sup>-1</sup>	molar mass of Na	[Magill <i>et al.</i> , 2006]
$\mu_{Au}$		mm <sup>-1</sup>	self-attenuation factor for photons in Au	
$\mu_{Cl}$		mm <sup>-1</sup>	self-attenuation factor for photons in Cl	
$\mu_{Na}$		mm <sup>-1</sup>	self-attenuation factor for photons in Na	
N <sub>A</sub>	6.0221*10 <sup>23</sup>	mol <sup>-1</sup>	Avogadro number	[Mohr <i>et al.</i> , 2008]
$\nu_{Au}$	2.083*10 <sup>-2</sup>	mm <sup>2</sup> mg <sup>-1</sup>	self-attenuation factor for 411.80 keV photons in Au	calculated from [NIST, 2009]
$\nu_{Au}^{1369}$	5.50*10 <sup>-3</sup>	mm <sup>2</sup> mg <sup>-1</sup>	self-attenuation factor for 1368.63 keV photons in Au	calculated from [NIST, 2009]
$\nu_{Cl}$	9.20*10 <sup>-3</sup>	mm <sup>2</sup> mg <sup>-1</sup>	self-attenuation factor for 411.80 keV photons in Cl	calculated from [NIST, 2009]
$\nu_{Cl}^{1369}$	5.25*10 <sup>-3</sup>	mm <sup>2</sup> mg <sup>-1</sup>	self-attenuation factor for 1368.63 keV photons in Cl	calculated from [NIST, 2009]
$\nu_{Na}$	9.07*10 <sup>-3</sup>	mm <sup>2</sup> mg <sup>-1</sup>	self-attenuation factor for 411.80 keV photons in Na	calculated from [NIST, 2009]
$\nu_{Na}^{1369}$	5.22*10 <sup>-3</sup>	mm <sup>2</sup> mg <sup>-1</sup>	self-attenuation factor for 1368.63 keV photons in Na	calculated from [NIST, 2009]
r	3	mm	radius of foils and pellets	given by radius of press
$\sigma_{Au}$	9.865(90)*10 <sup>-23</sup>	cm <sup>2</sup>	thermal neutron capture cross-section for <sup>197</sup> Au	[Mughabghab, 1981]
$\sigma_{Cl}$	4.36(4)*10 <sup>-23</sup>	cm <sup>2</sup>	thermal neutron capture cross-section for <sup>35</sup> Cl	[Mughabghab, 1981]
$\sigma_{SACS(Au)}$	5.86(8)*10 <sup>-24</sup>	cm <sup>2</sup>	spectrum averaged cross-section for <sup>197</sup> Au	[Ratynski & Käppeler, 1988]
$\sigma_{Na}$	5.30(5)*10 <sup>-25</sup>	cm <sup>2</sup>	thermal neutron capture cross-section for <sup>23</sup> Na	[Mughabghab, 1981]

**Table 5.6:** Constants and their uncertainties (in parenthesis) used for the determination of the neutron fluence during the irradiation. Values without uncertainties mean that these could be neglected. After the derivation of the correction for the photon-self-attenuation the self-attenuation factors in units of mm<sup>-1</sup> were replaced by the self-attenuation factors in units mm<sup>2</sup> mg<sup>-1</sup> ( $\nu$ ) by  $\nu = \mu/\rho$ .

Variable	Comment	Variable	Comment
A	activity, without corrections	$M_{NaCl}$	mass of NaCl powder
$A_I$	activity, corrected for dead- and irradiation time	$M_{pow}$	mass of NaCl + Au powder
$A_{IWM}$	activity, corrected for dead time, irradiation-, waiting- and measurement time	m	sample mass
$A_M$	activity, corrected for dead- and measurement time	$m_{Au}$	mass of Au in pellet
$A_{WM}$	activity, corrected for dead time, waiting- and measurement time	$m_{foil}$	Au foil mass
$A_t$	dead time corrected activity	$m_{pel}$	pellet mass
$A_{tot}$	activity, considering "all" correction factors	$N_{197}$	number of $^{197}\text{Au}$ in sample
$a_i$	activity per thin layer of sample	$N_{198}$	number of $^{198}\text{Au}$ in sample
$\alpha$	area density of sample	$\nu_{pel}$	self attenuation factor for pellet
C	number of detected counts in full energy peak	$\rho$	sample density
$C_{all}$	number of all detected counts	$T_{dead}$	total dead time
$C_t$	dead time-corrected number of counts in full energy peak	$t_0$	start point (time) of irradiation
c	count-rate in full energy peak	$t_I$	irradiation time
$c_t$	dead time corrected count-rate in full energy peak	$t_M$	measurement time
d	thickness of sample	$t_W$	waiting time between irradiation and measurement
$\Phi$	neutron fluence (no decay corrections)	$t_{dead}$	dead time of the detector after a registered event
$\Phi_{tot}$	neutron fluence, corrected for dead time, irradiation-, waiting- and measurement time	$t_{end}$	end of measurement time
$\phi$	"uncorrected" neutron flux	$t_{life}$	life time of detector
$I_{tot}$	total $\gamma$ -radiation intensity from sample	$t_s$	see correction factor for measurement time in section 5.3.1, page 56
$i_i$	$\gamma$ -radiation intensity from thin layer of sample	$t_{start}$	start of measurement
$K_{\nu,foil}$	self-attenuation correction factor for Au-foils	$w_{Au}$	relative mass of Au in pellet
$K_{\nu,pel}$	self-attenuation correction factor for pellets	$w_{Cl}$	relative mass of Cl in pellet
$M_{Au}$	mass of Au powder	$w_{Na}$	relative mass of Na in pellet

**Table 5.7:** Variables used for the determination of the neutron fluence during the irradiations.

$$T_{dead} = t_{dead}C_{all} \quad (5.11)$$

The difference between the true number of counts and the measured number of counts equals:

$$C_t - C = T_{dead} \frac{C_t}{t_M} \quad (5.12)$$

By some algebraic transformations one can find that the true count-rate can be calculated by:

$$c_t = \frac{C}{t_M - T_{dead}} = \frac{C}{t_{life}} \quad (5.13)$$

The dead time corrected activity is then given by:

$$A_t = \frac{C}{t_{life} \varepsilon_{412} I_{412}} \quad (5.14)$$

The life time of the detector is automatically measured by the detector electronics, if the dead time is dominated by the electronics.. Due to the fact that the count-rates in my measurements (ATI and BUD samples) were not very high (see tab. 5.9) the relative dead time for a measurement was in the range of 0.01-0.04 %, leading to a negligible dead time correction.

- **Decay correction factor for the measurement time**

The exponential character of the radioactive decay described in chapter 2.2 has to be considered in the calculation. The activity is the negative time-derivation of the number of radioactive nuclei, and changes exponentially. In the equations above this was not considered and the activity was assumed constant during the measurement. Taking this exponential change into account, one has to use the mean value theorem. Applied to the case of radioactive decay it says that there is a point in the time interval of the measurement  $t_s$ , at which the differential activity  $A(t_s) = A_M$  (slope of the tangent in a point of the measurement interval) equals the mean activity in this interval (negative slope of the secant between  $N_{198}(t_{end})$  and  $N_{198}(t_{start})$  see fig. 5.11). In this figure one can see that  $t_s \neq \frac{t_{end} + t_{start}}{2}$ . The correct activity for the measurement-time is the calculated activity at  $t_s$ .

$$A_M = \lambda_{Au} N_{198}(t_{start}) e^{-\lambda_{Au} t_s} = - \frac{N_{198}(t_{end}) - N_{198}(t_{start})}{t_{end} - t_{start}} \quad (5.15)$$

For the calculation of the correction factor one has to take the real measurement time and not the life time of the detector, but for the final correction one has

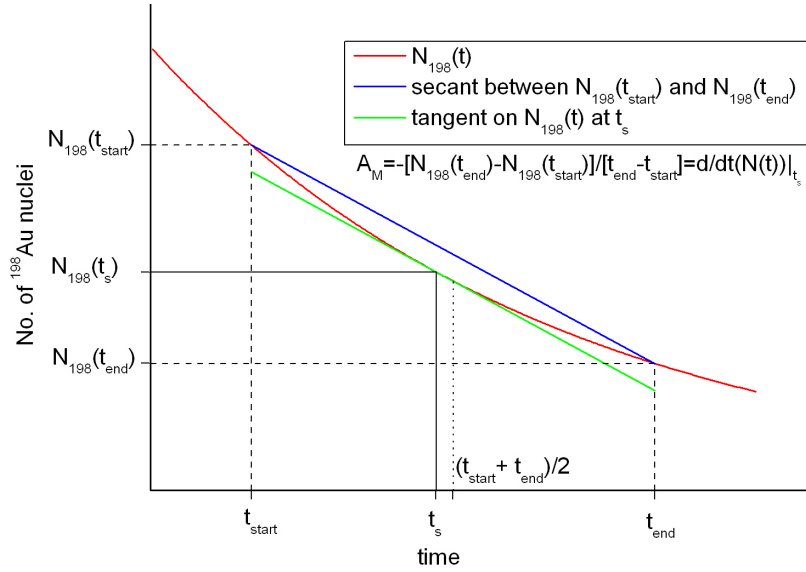


**Figure 5.11:** Illustration of the mean value theorem. The slope of the tangent at  $N_{198}(t_s)$  (negative activity at  $t_s$ ) is equal to the slope of the secant between the points  $N_{198}(t_{start})$  and  $N_{198}(t_{end})$ .

to take the value of the dead time corrected activity  $A_t$  again. With  $t_M = t_{end} - t_{start}$  the above equation can be used to calculate  $t_s$  by:

$$t_s = \frac{\ln(\lambda_{Au} t_M) - \ln(1 - e^{-\lambda_{Au} t_M})}{\lambda_{Au}} \quad (5.16)$$

The activity, corrected for the decay during the measurement time, is then:

$$A_M = A_t \frac{\lambda_{Au} t_M}{1 - e^{-\lambda_{Au} t_M}} \quad (5.17)$$

As one can see from the equation above the correction factor obviously depends on the product of the measurement time and the decay constant (ratio of measurement time and half-life of  $^{198}\text{Au}$ ). My activity measurements normally lasted between 900 and 12000 s resulting in measurement time corrections from 0.1-1.7 %.

- **Decay correction factor for the waiting time**

A certain amount of nuclei in the samples also decayed during the transport of the samples from the irradiation site to the Ge-detector and the waiting time till the measurement. To calculate the activity at the end of the neutron irradiation ( $A_{WM}$ ) one has to multiply  $A_M$  with a correction factor which considers the waiting time  $t_W$ . This is done by:

$$A_{WM} = A_M e^{\lambda_{Au} t_W} \quad (5.18)$$

Due to the fact that the foils and pellets were measured one by one and each sample was measured several times the values for the waiting time are distributed over a wide range (between 2.5 h to nearly 7.7 d), resulting in correction factors from 3 % up to 7 (700 %). Because the half-life of  $^{198}\text{Au}$  is well-known no significant additional uncertainty was introduced to the final values from such long waiting times.

- **Decay correction factor for the irradiation time**

Assuming a time constant neutron flux,  $^{198}\text{Au}$  atoms are continuously produced, during the irradiation of the samples but their number is also reduced by radioactive decay. In order to calculate the total amount of  $N_{198}$  produced during the irradiation, the measured activity has to be corrected for the number of atoms, which decayed during the irradiation. The differential equation which describes the production and decay of  $^{198}\text{Au}$  can be written as:

$$\frac{dN_{198}(t)}{dt} = \sigma_{Au} \phi N_{197} - \lambda_{Au} N_{198}(t) \quad (5.19)$$

The production of  $^{198}\text{Au}$ , by neutron capture on  $^{197}\text{Au}$  reduces the number of  $^{197}\text{Au}$  atoms ( $N_{197}$ ), but the relative change of  $N_{197}$  is so small that it can be neglected and  $N_{197}$  can be assumed constant. The general solution of the differential equation above is given by:

$$N_{198}(t) = k e^{-\lambda_{Au} t} + \frac{\sigma_{Au} \phi N_{197}}{\lambda_{Au}} \quad (5.20)$$

With the initial condition that at the beginning of the irradiation there are no  $^{198}\text{Au}$  atoms ( $N_{198}(t_0)=0$ ) and setting the value for the irradiation time to  $t_I$  one gets:

$$N_{198}(t_I) = \frac{\sigma_{Au} \phi N_{197}}{\lambda_{Au}} (1 - e^{-\lambda_{Au} t_I}) \quad (5.21)$$

for the number of  $^{198}\text{Au}$  atoms, and

$$A_I = \lambda_{Au} \frac{\sigma_{Au} \Phi N_{197}}{t_I \lambda_{Au}} (1 - e^{-\lambda_{Au} t_I}) \quad (5.22)$$

for the activity after the irradiation, which equals  $A_{WM}$ .

The factor  $\lambda_{Au} \sigma_{Au} \Phi N_{197} \equiv A_{IWM}$  is the activity, the sample would have after the irradiation, if no decay would take place (i.e.  $t_I$  is much shorter than the

half-life of the decay). This activity is needed if one wants to calculate the neutron fluence during the irradiation. Using  $A_I = A_{WM}$  one gets  $A_{IWM}$  by:

$$A_{IWM} = A_{WM} \frac{\lambda_{Au} t_I}{1 - e^{-\lambda_{Au} t_I}} \quad (5.23)$$

For the ATI samples, which were irradiated for about 30 s the correction factor for the irradiation time of 0.004 % can be neglected. The correction factor for the BUD samples is also only in the order of 0.4 %. However the correction for the irradiation time plays a important role for the KIT samples where it was in the range of 12 to 78 %. (For this case also other corrections had to be considered, see section 5.3.2, equ. 5.36 and tab. 5.13.

- **Correction for self attenuation**

As explained in section 2.3 there is a certain probability that an emitted photon is reabsorbed by the emitting material. This self attenuation needs to be taken into account.

To calculate the self attenuation factors for the foils and pellets, one can assume that a sample consists of an infinite number (l) of thin layers with thickness  $dx$ . The thickness of the sample is then:  $d = l * dx$ . Each layer emits an equal amount of photons  $i_i = I_{tot}/l$  and, respectively, the same activity per layer  $a_i = A_{tot}/l = A_{tot}dx/d$ , but each layer also absorbs photons with a certain probability. The intensity and also the measured activity decrease exponentially with the thickness of the penetrated material (see equ. 2.45). The measured activity "outside" the sample, is then given by the sum over the "attenuated" activities of all layers.

$$A_{IWM} = \int_0^d \frac{A_{tot}}{d} e^{-\mu x} dx \quad (5.24)$$

where  $\mu$  is the self attenuation factor in units of  $\text{mm}^{-1}$ . After the integration and some transformations one gets:

$$A_{tot} = A_{IWM} \frac{\mu d}{1 - e^{-\mu d}} \quad (5.25)$$

The equation above can be transformed by expressing the thickness of the sample by the samples area density ( $\alpha$ ) and its density and expressing the mass attenuation factor in units of  $\text{mm}^2 \text{mg}^{-1}$  ( $\nu = \mu/\rho$ ):

$$A_{tot} = A_{IWM} \frac{\nu \rho \frac{\alpha}{\rho}}{1 - e^{-\nu \rho \frac{\alpha}{\rho}}} = A_{IWM} \frac{\nu m}{r^2 \pi} \frac{1}{1 - e^{-\frac{\nu m}{r^2 \pi}}} \quad (5.26)$$

where  $\alpha = \frac{m}{r^2 \pi}$  is the area density of the circular shaped Au-foils. The values for the mass attenuation coefficient  $\nu$  for Au, Na and Cl were taken from [NIST,

2009] and interpolated for 411.80 keV photons. To calculate the mass attenuation factor of a combined (NaCl+Au)-pellet, one has to weight the single mass attenuation factors of the elements with the relative mass of the element in the pellet and add their weighted values.

$$\nu_{pel} = w_{Au}\nu_{Au} + w_{Na}\nu_{Na} + w_{Cl}\nu_{Cl} \quad (5.27)$$

where:

$$w_{Au} = \frac{m_{Au}}{m_{pel}} = \frac{M_{Au}}{M_{pow}} \quad (5.28)$$

$$w_{Na} = \frac{M_{NaCl}m_{mol(Na)}}{m_{mol(Na)} + m_{mol(Cl)}} \frac{1}{M_{pow}} \quad (5.29)$$

$$w_{Cl} = \frac{M_{NaCl}m_{mol(Cl)}}{m_{mol(Na)} + m_{mol(Cl)}} \frac{1}{M_{pow}} \quad (5.30)$$

Summarizing all these equations one gets the self attenuation factor of a gold foil  $K_{\nu,foil}$  by:

$$K_{\nu,foil} = \frac{\nu_{Au}m_{foil}}{r^2\pi} \frac{1}{1 - e^{-\frac{\nu_{Au}m_{foil}}{r^2\pi}}} \quad (5.31)$$

and the self attenuation factor for a pellet  $K_{\nu,pel}$  by:

$$K_{\nu,pel} = \frac{1}{M_{pow}} \left( M_{Au}\nu_{Au} + \frac{M_{NaCl}}{m_{mol(Na)} + m_{mol(Cl)}} (m_{mol(Na)}\nu_{Na} + m_{mol(Cl)}\nu_{Cl}) \right) \frac{m_{pel}}{r^2\pi} \frac{1}{1 - e^{-\frac{1}{M_{pow}} \left( M_{Au}\nu_{Au} + \frac{M_{NaCl}}{m_{mol(Na)} + m_{mol(Cl)}} (m_{mol(Na)}\nu_{Na} + m_{mol(Cl)}\nu_{Cl}) \right) \frac{m_{pel}}{r^2\pi}}} \quad (5.32)$$

### Total efficiency of a Ge-detector

The total efficiency strongly depends on the energy of the photons which should be detected and on the distance between the detector and the sample. The efficiency of the HP-Ge-detector used at VERA was studied in the early nineties by [Wagner, 1991] with a set of primary and secondary calibration standards ( $^{241}\text{Am}$ ,  $^{109}\text{Cd}$ ,  $^{57}\text{Co}$ ,  $^{139}\text{Ce}$ ,  $^{51}\text{Cr}$ ,  $^{113}\text{Sn}$ ,  $^{85}\text{Sr}$ ,  $^{137}\text{Cs}$ ,  $^{54}\text{Mn}$ ,  $^{88}\text{Y}$ ,  $^{65}\text{Zn}$  and  $^{60}\text{Co}$ ). It was measured for 14 different energies in the range of 59.5 keV to 1836 keV and for eight different distances between sample and active area of the detector (0-14.5 cm) Since then it was regularly checked with multi-element calibration sources (see e.g. [Buczak, 2009]).

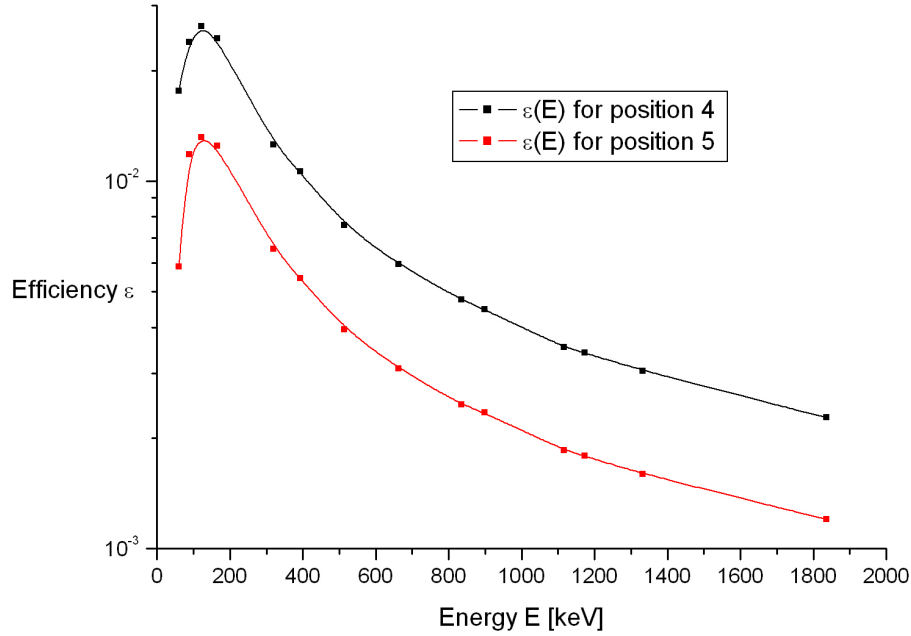


**Figure 5.12:** Efficiency of the Ge-detector at VERA as a function of photon-energy.  $\varepsilon(E_\gamma)$  is given for 2 different distances between the sample and the active area of the detector (position 4 is equal to a distance of 4 cm and position 5 is equal to a distance of 6.5 cm). The measurement data from [Wagner, 1991] was fitted by piecewise polynomial functions.

As one can see in fig. 5.13 there is a linear relation between distance and  $\frac{1}{\sqrt{\varepsilon}}$ . To get the efficiency for 411.80 keV at the sample position (distance to the active area of the detector  $y = 4 \text{ cm} + \text{half of the thickness of the sample}$ ) the values for the efficiency at 411.80 keV at all positions were taken from fig. 5.12. The uncertainty of the measurements was taken from [Wagner, 1991]. Linear fits of the data (distance versus  $-\frac{1}{\sqrt{\varepsilon}}$  at 411.80 keV and 1368.62 keV) were made. The slope  $k_{412}$  and the offset  $d_{412}$  of these functions were used to calculate the efficiency and its uncertainty at 411.80 keV and 1368.62 keV.

The calculated uncertainty for the efficiency was underestimated with this procedure, because the systematic uncertainty, was not considered here. So the final uncertainty of the efficiency was assumed to be 2 %.

$$\varepsilon_{412} = \frac{1}{(k_{412}y + d_{412})^2} \quad (5.33)$$

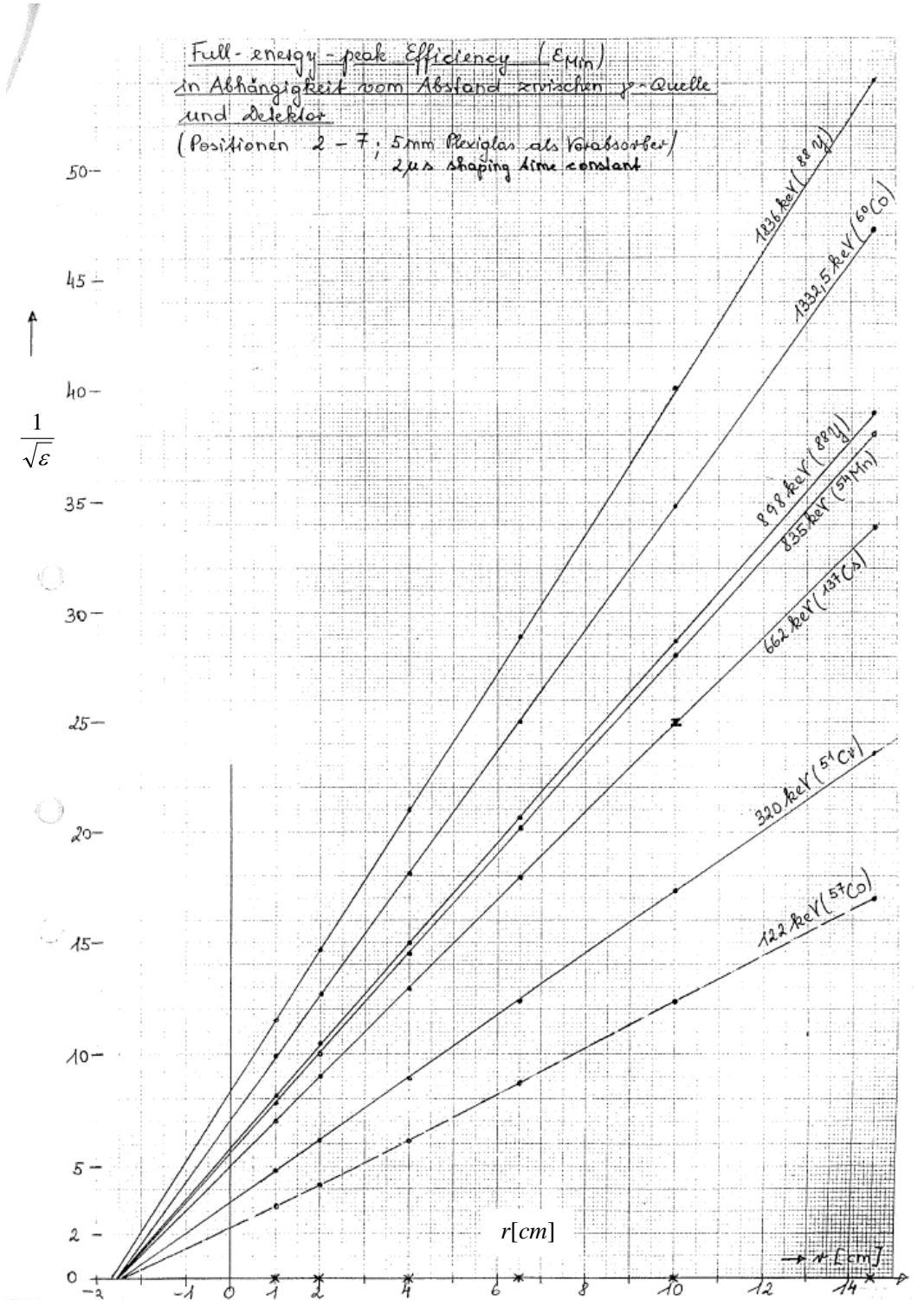


**Figure 5.13:** Efficiency of the Ge-detector at VERA as a function of the distance between sample and the active area of the detector.  $\epsilon(r)$  is given for 7 different energies. The data was taken from [Wagner, 1991].

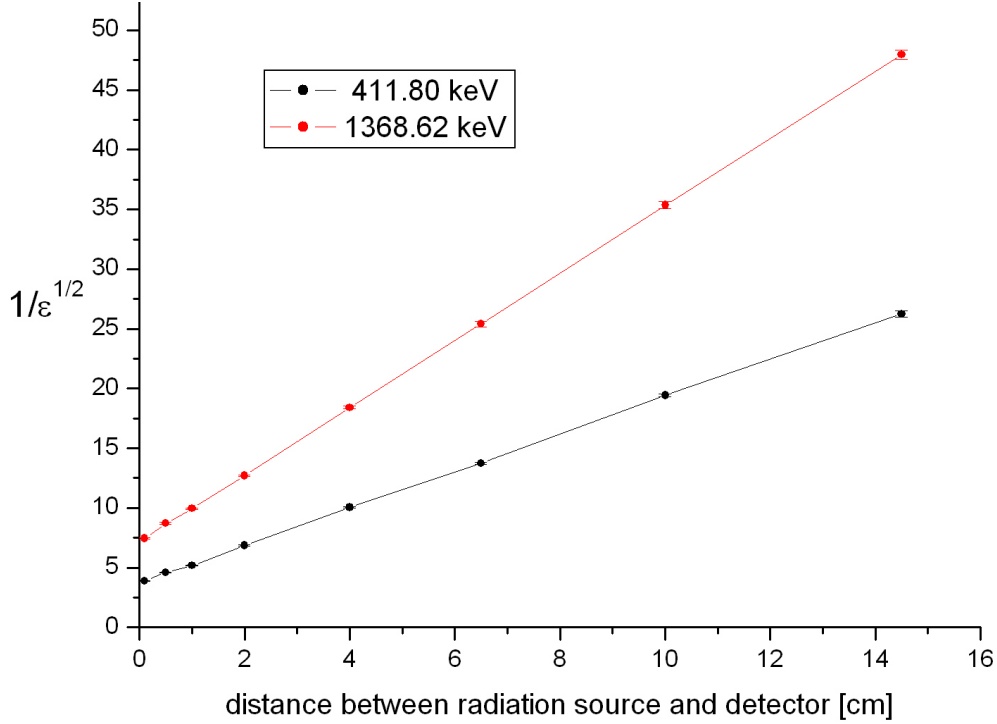


**Figure 5.14:** Efficiency of the high purity Ge-detector at VERA as a function of the distance between sample and active area of the detector for the two relevant photon energies for this work. The black line is the fitted curve for the photons emitted by deexcitement of  $^{198}\text{Hg}$  nuclei and the red line is the fit for the photons emitted by deexcitement of  $^{24}\text{Mg}$  nuclei. The data for the fit was taken from [Wagner, 1991] (see fig. 5.12).

### 5.3.2 Results and Discussion

Taking into account all these corrections the final equation for the total activity of a sample is:

$$A_{tot} = K_{\nu} \frac{\lambda_{Au} t_I}{1 - e^{-\lambda_{Au} t_I}} \frac{\lambda_{Au} t_M}{1 - e^{-\lambda_{Au} t_M}} e^{\lambda_{Au} t_W} \frac{C}{t_{life} \varepsilon_{412} I_{412}} \quad (5.34)$$

Combining this with equations 5.4, 5.8 and 5.7 one gets:

$$\Phi_{tot} = K_{\nu} \frac{t_I}{1 - e^{-\lambda_{Au} t_I}} \frac{\lambda_{Au} t_M}{1 - e^{-\lambda_{Au} t_M}} e^{\lambda_{Au} t_W} \frac{C m_{mol(Au)}}{t_{life} \varepsilon_{412} I_{412} N_A m \sigma_{Au}} \quad (5.35)$$

Where  $m$  is  $m_{foil}$  for the Au-foils and  $m_{Au} = \frac{m_{pel}}{M_{pow}} M_{Au}$  for the (NaCl+Au)-pellets. The activity of each sample was measured 1 to 7 times. The calculations done for each sample will be exemplified on the data for sample BUD1 and its Au- foils. The results for the activity of the BUD1 sample and its attached gold foils are listed in tab. 5.9. For all other samples the final results for the neutron fluence are listed in

the tables 5.10, 5.11, 5.12 and 5.13.

Sample	$t_I$ [s]	$\varepsilon_{412}$	rel. unc. $\varepsilon_{412}$ [%]	$K_\nu/m$ [mg <sup>-1</sup> ]	rel. unc. $K_\nu/m$ [%]
Au-BUD1-f	2392	0.0101	2	0.06752	0.07
BUD1	2392	0.0100	2	0.10634	0.12
Au-BUD1-b	2392	0.0101	2	0.06821	0.07

**Table 5.8:** Values for the irradiation time, the efficiency and the self attenuation correction factor for one specific sample.

Sample	Meas. No.	$t_W$ [s]	$t_M$ [s]	$t_{life}$ [s]	No. of Counts	$\Phi_{tot}$ [10 <sup>11</sup> cm <sup>-2</sup> ]	rel. unc. $\Phi_{tot}$ [%]
foil Au-BUD1-f	1	90800	1967	1967	40342 ± 201	2.11	2.3
	2	180100	2776	2775	42958 ± 210	2.08	2.3
	3	204200	2864	2864	41754 ± 207	2.10	2.3
	4	295600	3678	3677	40562 ± 204	2.09	2.3
	5	299400	3692	3691	40402 ± 204	2.10	2.3
	<b>mean</b>					<b>2.094</b>	<b>2.21</b>
foil Au-BUD1-b	1	87600	2852	2852	40673 ± 204	1.47	2.3
	2	176100	3734	3734	41051 ± 205	1.48	2.3
	3	200000	4025	4024	41581 ± 206	1.49	2.3
	4	313300	5487	5486	40324 ± 203	1.49	2.3
	5	318900	5786	5785	42218 ± 208	1.50	2.3
	6	646200	18000	17998	47716 ± 222	1.47	2.3
	7	664200	4067	4067	10507 ± 104	1.48	2.4
<b>mean</b>					<b>1.481</b>	<b>2.22</b>	
pellet BUD1	1	93300	4020	4019	41228 ± 203	1.70	2.3
	2	166400	5470	5469	44200 ± 210	1.67	2.3
	3	207300	5609	5608	41052 ± 207	1.71	2.3
	4	272600	7200	7199	43090 ± 204	1.70	2.3
	5	279800	7200	7199	41703 ± 204	1.68	2.3
	<b>mean</b>					<b>1.687</b>	<b>2.22</b>

**Table 5.9:** Data from the activity measurement of the Au powder in sample BUD1 and the attached Au foils (Au-BUD1-f, Au-BUD1-b). The uncertainty of the neutron fluence is the same for nearly each measurement, because the number of counts in the single measurements do not differ a lot. In addition, the uncertainty is dominated by the systematic uncertainty of the efficiency (see tab. 5.8). The statistical uncertainty (No. of counts) is in the range of 0.5 % and the uncertainties of the time intervals were neglected.

The uncertainty of the neutron fluence was calculated following the Gaussian error propagation law. Correlations were taken into account.

An absolute <sup>36</sup>Cl/<sup>35</sup>Cl-ratio was calculated for the ATI and BUD samples using the neutron fluence and the cross-section value for thermal energies  $\sigma_{Cl}=43.6(4)$  barn [Mughabghab, 1981] via equ. 5.3. <sup>36</sup>Cl-decay during irradiation-, waiting and

measurement time was negligible, due to the long half-life of  $^{36}\text{Cl}$  ( $t_{1/2}=3.01\cdot 10^5\text{a} \gg t_I, t_W, t_M$ ). These samples can be used as AMS reference material. The quality of these reference material will be discussed later in this chapter and in chapter 7.

Sample	$\langle \Phi_{tot} \rangle$ [ $10^{11} \text{ cm}^{-2}$ ]	calculated $\frac{^{36}\text{Cl}}{^{35}\text{Cl}}$ -ratio in pellet [ $10^{-12}$ ]
Au-ATI2-f	1.183±0.026	
Au-ATI2-b	1.217±0.028	
<b>mean value (foils)</b>	<b>1.200±0.027</b>	<b>5.23±0.13</b>
Au-ATI3-f	1.214±0.027	
Au-ATI3-b	1.283±0.029	
<b>mean value (foils)</b>	<b>1.248±0.028</b>	<b>5.44±0.13</b>

**Table 5.10:** Mean values for the neutron fluences during the irradiation of the first two ATI samples and the resulting  $^{36}\text{Cl}/^{35}\text{Cl}$ -ratios assuming a pure thermal spectrum.

Sample	$\langle \Phi_{tot} \rangle$ [ $10^{11} \text{ cm}^{-2}$ ]	$\frac{\langle \Phi_{tot, sample} \rangle}{\langle \Phi_{tot, MV foils} \rangle}$	calculated $\frac{^{36}\text{Cl}}{^{35}\text{Cl}}$ in pellet [ $10^{-11}$ ]
Au-BUD1-f	2.091±0.046	1.172	
Au-BUD1-b	1.480±0.033	0.828	
<b>mean value (foils)</b>	<b>1.783±0.039</b>	<b>1.000</b>	<b>0.778±0.019</b>
BUD1 $^{198}\text{Au}$ in pellet	1.678±0.037	0.941	0.732±0.018
BUD1 $^{24}\text{Na}$ in pellet	1.789±0.049	1.003	0.780±0.023
Au-BUD2-f	2.583±0.057	1.074	
Au-BUD2-b	2.226±0.049	0.926	
<b>mean value (foils)</b>	<b>2.405±0.053</b>	<b>1.000</b>	<b>1.048±0.025</b>
BUD2 $^{198}\text{Au}$ in pellet	2.324±0.052	0.967	1.013±0.024
BUD2 $^{24}\text{Na}$ in pellet	2.493±0.068	1.037	1.087±0.031
Au-BUD3-f	2.605±0.058	1.192	
Au-BUD3-b	1.766±0.039	0.808	
<b>mean value (foils)</b>	<b>2.186±0.048</b>	<b>1.000</b>	<b>0.953±0.023</b>
BUD3 $^{198}\text{Au}$ in pellet	no Au-powder	-	-
BUD3 $^{24}\text{Na}$ in pellet	not measured	-	-

**Table 5.11:** Mean values of the neutron fluence during the irradiation of the samples BUD1,2,3 and their calculated  $^{36}\text{Cl}/^{35}\text{Cl}$ -ratios. The value  $\frac{\langle \Phi_{tot, sample} \rangle}{\langle \Phi_{tot, MV foils} \rangle}$  is the ratio between the fluence value deduced from the particular sample and the mean fluence value deduced from the two foils of the particular sample stack (foil-pellet-foil).

The dominating uncertainty in all the activity measurements was the uncertainty of the Ge-detector efficiency. The  $^{36}\text{Cl}/^{35}\text{Cl}$ -ratio calculated for samples ATI2 and ATI3 might not be correct because:

1. The shape of the gold foils Au-ATI2-back and Au-ATI3-front was not circular and the geometry of these samples was not considered in the calculations (small

effect).

2. The neutron spectrum at ATI consists mainly of thermal neutrons, but contains also a significant epithermal fraction, and due to a different shape of the differential cross-section for  $^{35}\text{Cl}$  and  $^{197}\text{Au}$  it might not be correct to calculate the  $^{36}\text{Cl}/^{35}\text{Cl}$ -ratio from the thermal cross-section values of both isotopes.

The neutron fluence obtained for the front and back foil of the BUD samples differs much more than for the ATI samples. This is due to the geometry of the irradiation at the BRR, where all the neutrons came from the "forward" direction, whereas at the ATI the neutrons came from all directions. The decrease of the neutron flux in the sample is a combination of the exponential absorption losses (similar to photon-attenuation) and the decrease due to the increasing distance to the reactor ( $\frac{1}{r^2}$ ). For our samples a linear decrease of the neutron flux was estimated.

As shown in tab. 5.11 there are differences between 3.3 and 5.9 % for the neutron fluence measured by the gold foils (mean value) and the neutron fluence measured by the gold powder. However these values should be in agreement if a linear decrease of the neutron fluence is assumed. If an exponential decrease of the neutron fluence within the pellets is considered, the value determined by the gold in the pellet should be approximately 1-2 % smaller than the value determined by the gold foils. In this case the values would match within their uncertainties.

To investigate this discrepancies the peak at 1368.63 keV [Firestone, 2007] coming from the  $\gamma$ 's of the decay of  $^{24}\text{Na} \xrightarrow{\beta^-} ^{24}\text{Mg}^* \xrightarrow{\gamma} ^{24}\text{Mg}$ , in the full energy spectra of the pellets was also studied.  $^{24}\text{Na}$  was produced simultaneously via neutron capture on  $^{23}\text{Na}$  in the NaCl pellets. The calculation of the neutron fluence is the same as for Au-samples, only some constants have to be adapted. The statistics (number of counts in the peak) is worse because the thermal neutron capture cross-section of  $^{23}\text{Na}$  is a factor of 200 smaller than for  $^{198}\text{Au}$  (see tab. 5.6) and the half-life of  $^{24}\text{Na}$  is only a factor of 4 shorter than the half-life of  $^{198}\text{Au}$ , so the Na activity was much lower. However the fluence could be calculated with an accuracy of 2.7 %.

There are also discrepancies between the fluence values calculated from the  $^{24}\text{Na}$  activity and the mean values of the Au-foils but they are smaller (0.3-3.7 %). A remaining problem is that the values calculated by the Na-activity are greater than those calculated by the activity of the gold foils.

To further investigate if these discrepancies will be reproduced, samples ATI5 to ATI9 were prepared at VERA and irradiated at the TRIGA Mark II reactor. The aim was to see if this discrepancy, was caused by a wrong linear approximation of the decrease of the neutron flux in the sample, or due to limited accuracy during the production of the pellets (weighing and homogenizing of the powder). In the first case the measured neutron fluence should strongly depend on the thickness of the samples. With sample ATI9, which consisted of four Au-foils (the inner foils were the "old" Au-BUD1-back and Au-BUD2-back, ( $^{198}\text{Au}$  already fully decayed) and the outside gold foils were new ones not used in previous measurements), the validity of the fluence values measured by the "old" foils should be tested.

Tab. 5.12 demonstrates, that the difference in the fluence obtained from gold foils and from gold powder was smaller. Therefore, I obtained higher differences between the fluence determined by the Na in the pellets and by the Au-foils. For samples ATI5,6,7,8 this difference rises with the thickness of the target (see fig. 5.16). Due to neutron absorption (exponential decrease) the inner layers of the NaCl-pellet should not see as much neutrons as the outer layers. This neutron absorption was not considered in the calculation of the fluence and so the fluence obtained from the Na-powder should be smaller than the mean neutron fluence obtained by the gold foils. The explanation of the discrepancy between the gold powder and the gold foils (see fig. 5.15) of the BUD samples is a combination of the above mentioned possibilities. The activity of the gold powder is sensitive to a small loss of gold powder before the mixing procedure, because of the small amount of gold needed. Due to the larger mass of the NaCl powder used, the activity of the NaCl is not so sensitive to small losses of NaCl before the mixing process.

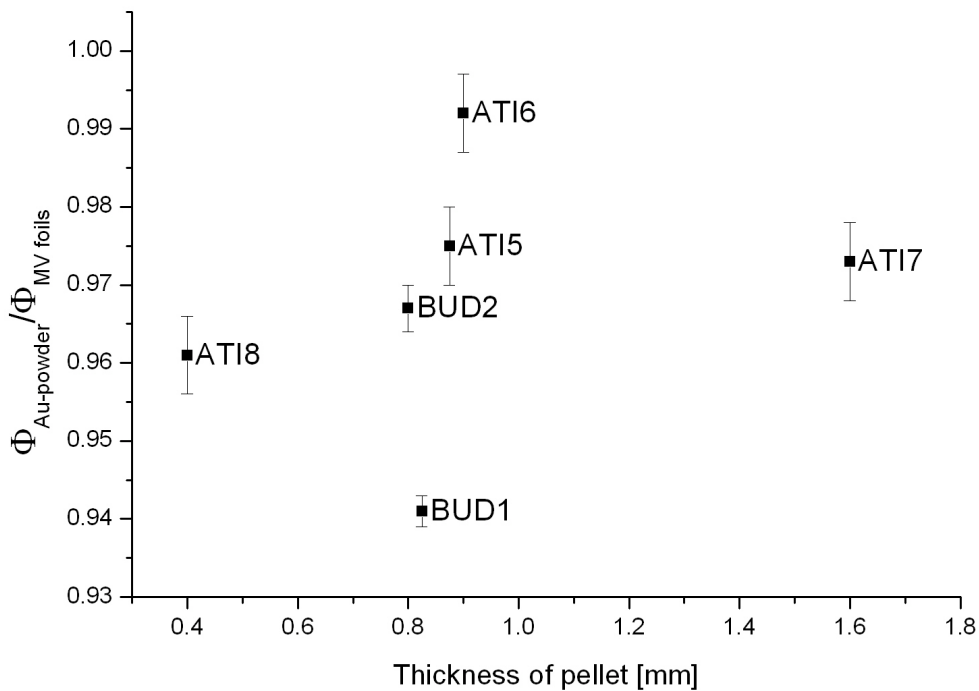


**Figure 5.15:**  $\frac{\langle \Phi_{tot, Au-powder} \rangle}{\langle \Phi_{tot, MV foils} \rangle}$ -ratios of the BUD1,2 and ATI5,6,7,8 samples. There is no obvious connection between this ratio and the thickness of the pellets.

It was the best choice to take the fluence and the  $^{36}\text{Cl}/^{35}\text{Cl}$ -ratio calculated from the mean value of the activities of the gold foils, and its uncertainty for the calculation of the  $^{36}\text{Cl}/^{35}\text{Cl}$ -ratio of the produced reference material BUD1, BUD2 and BUD3. These values are not sensitive to preparation procedures like the gold pow-

Sample	$\langle \Phi_{tot} \rangle$ [ $10^{11} \text{ cm}^{-2}$ ]	$\frac{\langle \Phi_{tot, sample} \rangle}{\langle \Phi_{tot, MV foils} \rangle}$	calculated $\frac{^{36}\text{Cl}}{^{35}\text{Cl}}$ in pellet [ $10^{-12}$ ]
Au-ATI5-f	1.156±0.026	1.014	
Au-ATI5-b	1.123±0.026	0.985	
<b>mean value (foils)</b>	<b>1.140±0.026</b>	<b>1.000</b>	<b>4.97±0.12</b>
ATI5 $^{198}\text{Au}$ in pellet	1.111±0.025	0.975	4.84±0.12
ATI5 $^{24}\text{Na}$ in pellet	1.096±0.026	0.961	4.79±0.11
Au-ATI6-f	1.206±0.028	1.000	
Au-ATI6-b	1.206±0.028	1.000	
<b>mean value (foils)</b>	<b>1.206±0.027</b>	<b>1.000</b>	<b>5.26±0.13</b>
ATI6 $^{198}\text{Au}$ in pellet	1.196±0.027	0.992	5.21±0.13
ATI6 $^{24}\text{Na}$ in pellet	1.167±0.029	0.968	5.10±0.13
Au-ATI7-f	1.073±0.025	1.005	
Au-ATI7-b	1.063±0.025	0.995	
<b>mean value (foils)</b>	<b>1.068±0.024</b>	<b>1.000</b>	<b>4.66±0.11</b>
ATI7 $^{198}\text{Au}$ in pellet	1.039±0.023	0.973	4.53±0.11
ATI7 $^{24}\text{Na}$ in pellet	1.001±0.023	0.937	4.38±0.10
Au-ATI8-f	1.145±0.027	0.999	
Au-ATI8-b	1.147±0.027	1.001	
<b>mean value (foils)</b>	<b>1.146±0.026</b>	<b>1.000</b>	<b>5.00±0.12</b>
ATI8 $^{198}\text{Au}$ in pellet	1.102±0.025	0.961	4.80±0.12
ATI8 $^{24}\text{Na}$ in pellet	1.130±0.028	0.986	4.94±0.12
Au-ATI9-f	1.236±0.029	1.006	
Au-ATI9-m1 foil	1.256±0.029	0.981	
Au-ATI9-m2 foil	1.217±0.028	1.022	
Au-ATI9-b	1.205±0.028	0.990	
<b>mean value (foils)</b>	<b>1.228±0.027</b>	<b>1.000</b>	

**Table 5.12:** Mean values of the neutron fluence during the irradiation of the second charge of ATI samples and the resulting  $^{36}\text{Cl}/^{35}\text{Cl}$ -ratios, assuming a pure thermal spectrum. The value  $\frac{\langle \Phi_{tot, sample} \rangle}{\langle \Phi_{tot, MV foils} \rangle}$  is the ratio between the fluence value deduced from the particular sample and the mean fluence value deduced from the two foils of the particular sample stack (foil-pellet-foil).

der. Furthermore, for samples BUD1 and BUD2 the statistics from the Na-decay measurements was low and for BUD3 no measurements of Na-decay were performed.

To study the attenuation of a neutron beam and its scattering in NaCl targets and Au foils, more samples with different thickness should be irradiated at the BRR, where all the neutrons are impinging from the forward direction. Additionally, a sample consisting of many Au-foils in a stack should be irradiated at the BRR and the activity of each foil should be measured.

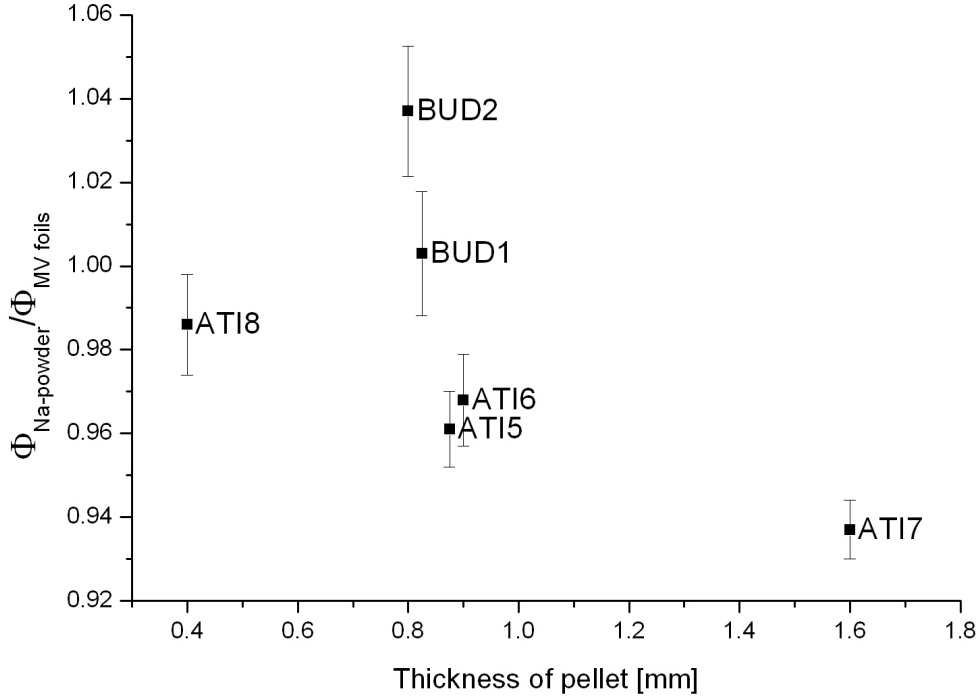


**Figure 5.16:**  $\frac{\langle \Phi_{tot, Na-powder} \rangle}{\langle \Phi_{tot, MV foils} \rangle}$ -ratios of the BUD1,2 and ATI5,6,7,8 samples. For the ATI samples the ratio decreases with the thickness.

The activity of the Au-foils used as fluence monitors for the KIT (Karlsruhe Institute of Technology) samples was measured directly at KIT. Long-term irradiation (several days) with an intense proton beam deteriorated the Li or LiF target. This decreased the efficiency of the production of neutrons, and the neutron flux could not be assumed constant during the irradiation. These change was taken into account with the so-called  $f_b$ -correction factor [Dillmann *et al.*, 2009], which combines the correction for the decay during the irradiation time and the correction for the variable neutron flux:

$$f_b = \frac{\int_0^{t_I} \phi(t) e^{-\lambda_{Au}(t-t_I)} dt}{\int_0^{t_I} \phi(t) dt} \quad (5.36)$$

The corrected neutron fluence for the Au foils is then given by:

$$\Phi_{tot} = K_\nu \frac{1}{f_b} \frac{\lambda_{Au} t_M}{1 - e^{-\lambda_{Au} t_M}} e^{\lambda_{Au} t_W} \frac{C m_{mol}(Au)}{t_{life} \varepsilon_{412} I_{412} N_A m \sigma_{SACS}(Au)} \quad (5.37)$$

$\frac{1}{f_b}$  replaces the factor  $\frac{t_I}{1 - e^{-\lambda_{Au} t_I}}$  from equ. 5.35 for the KIT samples.

The results from the activity measurements in Karlsruhe are listed in tab. 5.13

taking into account the uncertainties listed in tab. 5.14.

Sample	$f_b$	$\Phi_{tot}$ [ $10^{14} \text{ cm}^{-2}$ ]
Au-KIT1-f	0.5343	$13.13 \pm 0.072$
Au-KIT1-b	0.5343	$11.26 \pm 0.062$
<b>mean value (foils)</b>	<b>0.5343</b>	<b><math>12.20 \pm 0.047</math></b>
Au-KIT2-f1	0.6294	$4.60 \pm 0.25$
Au-KIT2-b1	0.6294	$4.10 \pm 0.23$
<b>mean value (foils 1)</b>	<b>0.6294</b>	<b><math>4.28 \pm 0.17</math></b>
Au-KIT2-f2	0.6277	$5.18 \pm 0.28$
Au-KIT2-b2	0.6277	$3.74 \pm 0.21$
<b>mean value (foils 2)</b>	<b>0.6277</b>	<b><math>4.46 \pm 0.18</math></b>
Au-KIT2-f3	0.9090	$1.10 \pm 0.06$
Au-KIT2-b3	0.9090	$0.77 \pm 0.04$
<b>mean value (foils 3)</b>	<b>0.9090</b>	<b><math>0.94 \pm 0.05</math></b>
Au-KIT2-f4	0.7942	$3.55 \pm 0.20$
Au-KIT2-b4	0.7942	$2.57 \pm 0.14$
<b>mean value (foils 4)</b>	<b>0.7942</b>	<b><math>3.06 \pm 0.17</math></b>
<b>sum of mean values 1,2,3,4</b>		<b><math>12.74 \pm 0.070</math></b>

**Table 5.13:** Neutron fluence values during the irradiation of the KIT samples. Sample KIT1 was irradiated in one session and sample KIT2 was irradiated in four parts. Between these four sessions for KIT2 the gold foils were replaced. The fluence data was taken from [Dillmann, 2010]

Quantity	rel. unc. [%]	Comment
$\sigma_{SACS(Au)}$	1.40	not included because it cancels in the calculation
divergence neutron flux	5.00	
efficiency of detector at KIT	2.00	
m	1.00	
$I_{412}$	0.06	taken from [Xiaolong, 2009]
counting statistics	0.19-0.35	given by $\frac{\sqrt{C}}{C} * 100$

**Table 5.14:** Uncertainties for the calculation of the neutron fluence at the KIT as provided by [Dillmann, 2010].  $\sigma_{SACS(Au)}$  is the spectrum averaged cross-section for Au (see section 2.1.3 and equ. 2.28).

## 6 Sample preparation for AMS

Chemical and mechanical pretreatment of the irradiated samples is necessary to remove as much sulfur as possible, and to bring the samples in a proper chemical form suitable for the AMS measurements. The chemical procedures, as described in section 6.1, are based on experiences of the VERA- and other laboratories for removal of the sulfur from the samples and for keeping the sulfur contamination of the target holders low.

In addition to our neutron-irradiated samples, blank material (in our case AgCl with not measurable  $^{36}\text{Cl}$  content) is needed for the AMS measurements. The pretreatment for the blank material was the same as for the other samples (except for the irradiation). Reference material from the ETH Zürich (ETH K381/4N) was used for the AMS measurements and for comparison with my reference material. Additionally, secondary standards from a dilution series (with  $^{36}\text{Cl}/\text{Cl}$ -ratios between  $10^{-12}$  and  $10^{-16}$ ) were produced at VERA from a NaCl master-solution from Munich with an isotopic-ratio of  $^{36}\text{Cl}/\text{Cl} = 10^{-10}$  and a known mass concentration, of 150 g/l. (In the following mass concentration will be denoted as Z.) A part of these dilution series ( $10^{-16}$  too low for measurement) was normalized to the ETH K381/4N reference material and had the purpose to provide standard material over a wide range of isotopic ratios. This is not so important for my work because of the expected high ratios of my samples but it is important for the measurement of  $^{36}\text{Cl}/\text{Cl}$ -ratios in geological samples which is presently also a subject of research at VERA and collaborating laboratories ([Merchel *et al.*, 2008], [Steier *et al.*, 2010]).

The chemical pretreatment, which is based on a standard method by [Conrad *et al.*, 1986] and [Stone *et al.*, 1996] and the mechanical pretreatment of the samples can be summarized in the following three steps:

1. Dissolution of the sodium chloride (NaCl) powder or pellet in nitric acid ( $\text{HNO}_3$ ).
2. Precipitation of the dissolved NaCl with silver nitrate ( $\text{AgNO}_3$ ) in  $\text{HNO}_3$  to silver chloride (AgCl). Washing and drying of the resulting powder.
3. Pressing of the resulting AgCl-powder into Cu-sample holders with a silver bromide (AgBr) backing.

For this purposes additional preparations were required:

- Dilution of  $\text{HNO}_3$
- Dissolution of potassium bromide (KBr) in  $\text{HNO}_3$

- Dissolution of  $\text{AgNO}_3$  in  $\text{HNO}_3$
- Precipitation of the dissolved  $\text{KBr}$  with  $\text{AgNO}_3$  in  $\text{HNO}_3$  to silver bromide ( $\text{AgBr}$ ). Washing and drying of the resulting powder.
- Pressing of the resulting  $\text{AgBr}$  on Cu-cathodes (backing)

## 6.1 Chemical pretreatment

The micro spoons, forceps, stamps, mortars, pipets, tubes, volumetric glasses and plastic containers, needed for the chemical and mechanical pretreatment of the sample material, were cleaned every time after treatment of a sample material. All tools and containers were washed with distilled water. Except for the volumetric glasses, all tools were cleaned in an ultrasonic bath with isopropanol and distilled water (spoons, forceps, stamps, mortars) or 1.4 molar nitric acid (pipets, plastic tubes and containers), washed with distilled water again and dried in an oven at  $70^\circ\text{C}$ . During the chemical treatment gloves were used all the time. The used chemicals are listed in the table below.

Material	Origin	Specifications
$\text{HNO}_3$	VWR, Prolabo Art# 20429.320	65%, 14 molar see <a href="http://de.vwr.com/app/Home">http://de.vwr.com/app/Home</a>
$\text{AgNO}_3$	Merck Art# 101512	see <a href="http://www.merck.de/en/index.html">http://www.merck.de/en/index.html</a>
$\text{KBr}$	Merck Art# 104905	see <a href="http://www.merck.de/en/index.html">http://www.merck.de/en/index.html</a>
$\text{NaCl}$	Alfa Aesar Art# 010862	Puratronic® (metals basis) 99.999% purity, see <a href="http://www.alfa.com/">http://www.alfa.com/</a>
$\text{Au}$	Alfa Aesar Art# 43900	Gold powder, spherical, -325 mesh, 99.9% purity (metals basis)

**Table 6.1:** Materials used for the chemical preparation of  $\text{AgCl}$ -samples and  $\text{AgBr}$ -backings for AMS.

### Dilution of $\text{HNO}_3$ :

A weak acid is needed to dissolve the samples. Therefore, nitric acid with a molarity of 14 mol/l was diluted with distilled water. To get nitric acid with a molarity of approximately 1.3 - 1.4 mol/l, which was used for the dissolution of  $\text{KBr}$ ,  $\text{AgNO}_3$  and  $\text{NaCl}$ , one part  $\text{HNO}_3$  was mixed with 9 parts of distilled  $\text{H}_2\text{O}$ . For flushing the precipitated  $\text{AgCl}$  and  $\text{AgBr}$  powder, nitric acid with a molarity of 0.5 mol/l was used. Therefore, 1 part of  $\text{HNO}_3$  was diluted with approximately 27 parts of distilled  $\text{H}_2\text{O}$ . Barium nitrate ( $\text{Ba}(\text{NO}_3)_2$ ) and quartz filters ( $r \approx 3$  mm) were added

for precipitation of sulfur to barium sulfate ( $\text{BaSO}_4$ ) ([Stone *et al.*, 1996]). The use of barium nitrate and filters was a standard procedure in the production of all dissolutions in this work.

Dilution	$\text{HNO}_3$ (14 molar) [ml]	$\text{H}_2\text{O}$ (destilated) [ml]	$\text{Ba}(\text{NO}_3)_2$ (powder) [mg]
$\text{HNO}_3$	1.87	50.72	30

**Table 6.2:** Dilution of 14 molar  $\text{HNO}_3$  to 0.5 molar  $\text{HNO}_3$  for the precipitation of S with  $\text{Ba}(\text{NO}_3)_2$  and quartz filters

### Dissolution of $\text{AgNO}_3$ in $\text{HNO}_3$ :

Due to their high reactivity halogens like  $\text{Cl}^-$  are not stable in nature in their pure form. To get homogeneous target material (mainly one chemical compound) a binder for the Cl is needed. Silver was selected as binder because in its pure form it had a low sulfur count-rate, in AMS measurements [Conrad *et al.*, 1986] and because dissolved Ag precipitates readily with Cl to AgCl. Additionally, AgCl provides a high and steady chlorine beam [Conrad *et al.*, 1986] in AMS. For this purpose  $\text{AgNO}_3$ -powder together with  $\text{Ba}(\text{NO}_3)_2$  was dissolved in 1.4 molar nitric acid. Table 6.3 shows an example of a produced  $\text{AgNO}_3$  solution. The produced  $\text{AgNO}_3$  was stored in plastic bottles and wrapped into Al-foil to avoid photochemical reactions.

### Dissolution of KBr in $\text{HNO}_3$ :

From previous AMS measurements of Cl at VERA it was known that AgBr has a lower sulfur background than any other backing material tried. So it was decided to use AgBr on Cu cathodes for the backing of my samples. The first step in the production of AgBr was the dissolution of KBr-powder in approximately 1.3 molar nitric acid. Table 6.3 shows an example of a produced KBr solution.

### Dissolution of the NaCl in $\text{HNO}_3$ :

The irradiated NaCl samples and blank material (from Alfa Aesar and Merck) was also dissolved in 1.4 molar nitric acid.  $\text{Ba}(\text{NO}_3)_2$  and quartz filters were added. Examples for the dissolution of NaCl blank material and the resulting solutions of my NaCl samples are listed in tab. 6.3.

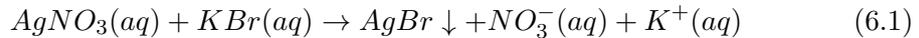
The samples ATI5 to ATI8 were mainly produced to clarify discrepancies in the fluence measurements of the BUD samples and so they were not prepared for AMS measurements yet.

Dissolution	AgNO <sub>3</sub> -, KBr- or NaCl-powder [mg]	HNO <sub>3</sub> (14 molar) [ml]	H <sub>2</sub> O (destilated) [ml]	Ba(NO <sub>3</sub> ) <sub>2</sub> (powder) [mg]	Z [g/l]
AgNO <sub>3</sub>	6622	1.89	17.03	28	360
KBr	3000	2.0	20.0	13	136
NaCl( $\alpha$ -Aesar)	125	0.500	4.500	1	25
KIT1(sol)	50	0.400	3.600	0.5	12.5
KIT2(sol)	46	0.370	3.300	10	12.5
ATI2(sol)	43	0.350	3.160	5	12.3
ATI3(sol)	22	0.180	1.580	4	15.5
BUD1(sol)	50	0.400	3.570	4	12.6
BUD2(sol)	48	0.380	3.450	4	12.5
BUD3(sol)	83	0.660	5.950	5	12.6

**Table 6.3:** Dissolution of AgNO<sub>3</sub>, KBr and NaCl in HNO<sub>3</sub>. In the last column the concentration of the resulting solution is shown. Other NaCl-blank solutions and other AgNO<sub>3</sub>- and KBr-solutions were produced in the same way.

#### Precipitation of the dissolved KBr to AgBr:

AgBr-powder, pressed on conic Cu-sample-holders (Cu-cathodes), was used as target backing during my AMS measurements in nearly all cases. Only during the first beam session conic Ta-disks, heated in hydrogen and pressed into Al-cathodes (Al-sample-holders), were used. For the precipitation of KBr a filter was tamped into a pipet tip which was fixed with a clamp and positioned above an Eppendorf tube. With a pipet a certain amount of AgNO<sub>3</sub> dissolved in HNO<sub>3</sub> was filled into the tip. The dripping of the solution through the filter into the Eppendorf tube was speed up by using nitrogen gas with a pressure of 1.5-2 bar to press the solution through the filter. This procedure was repeated with the KBr in HNO<sub>3</sub>, after changing both tips (the one on the pipet and the one with the filter). The two solutions reacted and AgBr precipitated as yellow powder in the following reaction:

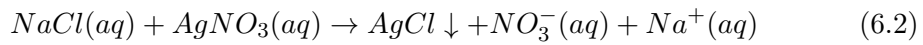


The ratio between the amount of used AgNO<sub>3</sub> and KBr was chosen so that all the silver atoms precipitate, which means that there had to be an excess of Br atoms (see tab 6.4). To separate the powder from the remaining solution the samples were centrifuged (with 4000 rpm for 10 minutes at a radius of 150 mm). During this process the powder was compressed and hardened. Afterwards the remaining solution was decanted. In the next step 1 ml of 0.5 molar HNO<sub>3</sub> was used to wash the samples. In the same way as the solutions before, the nitric acid was pressed through the tip (equipped with a filter) into the tube by using nitrogen gas. The solid AgBr was dispersed to powder again by putting the closed plastic tubes into an ultra sonic bath for several minutes. Then the centrifugation was repeated. The AgBr powder

took its solid form again and the nitric acid was decanted. The produced AgBr in the plastic tubes was dried in an oven at a temperature of 75-80 °C for several hours (5-20 h).

### Precipitation of the dissolved NaCl to AgCl:

The procedure for the precipitation of AgCl was the same as described above. With the exception that the NaCl (dissolved in HNO<sub>3</sub>) was pressed into the tube first and then the AgNO<sub>3</sub> (dissolved in HNO<sub>3</sub>) was added. AgCl precipitated as white powder immediately:



In the case of the irradiated samples an excess ( $\sim 10\%$ ) of Ag over Cl atoms was used to ensure that all of the Cl precipitates to AgCl (see tab 6.4). For the standards (AMS reference material) and the blanks this was not so important. The next preparation steps were the same as for AgBr.

Backing or sample material	AgNO <sub>3</sub> solution [ml]	Z (AgNO <sub>3</sub> ) [g/l]	No. of Ag atoms [mmol]	KBr or NaCl solution [ml]	Z (KBr or NaCl) [g/l]	No. of Br or Cl atoms [mmol]
Br100-106	0.40	350	0.82	1.20	136	1.37
Br107,108	0.40	350	0.82	1.23	136	1.41
Br110-113	0.35	350	0.72	1.20	136	1.37
Br120-129	0.40	350	0.82	0.90	136	1.02
$\alpha$ -blank 1-7	0.45	70	0.19	0.40	25	0.17
ATI2/1-4	0.25	70	0.10	0.40	12.5	0.09
ATI3/1-4	0.25	70	0.10	0.40	12.5	0.09
BUD1/1,2	0.25	70	0.10	0.40	12.5	0.09
BUD2/1,2	0.25	70	0.10	0.40	12.5	0.09
BUD3/1,2	0.25	70	0.10	0.40	12.5	0.09
KIT1/1,2	0.25	70	0.10	0.40	12.5	0.09
KIT1/3	0.25	70	0.10	0.40	12.5	0.09
KIT2/1,2	0.25	70	0.10	0.40	12.5	0.09

**Table 6.4:** Precipitation of Br to AgBr and Cl to AgCl for different backing and sample material. The material labeled with Br is AgBr, all the other material is AgCl (the blanks  $\alpha$ -blank 1-7 (NaCl from Alfa Aesar, see tab. 6.2) and the samples ATI,BUD and KIT). Br100-106 stands for AgBr-material produced in seven precipitations of the same Br. In the case of the AgCl material the numbers behind the slash indicate the number of precipitated AgCl material from the same solution.

$\alpha$ -blank (see tab. 6.4) is the denotation for the blanks produced from the NaCl from Alfa Aesar (see tab. 6.2). (Blanks from other NaCl-material were also produced but they were not used for my measurements.) The concentration of the KIT1 solution

changed between the precipitation of KIT1/2 on March 19 2009 and the precipitation of KIT1/3 on June 30 2009 due to vaporisation of  $\text{HNO}_3$  to an unknown level (no influence on isotopic ratios).

## 6.2 Mechanical pretreatment

For most targets Cu-sample-holder (Cu-cathodes) 6 mm in diameter with a conic drilling (5.5 mm in diameter) were used. These cathodes are bigger than the cathodes normally used at VERA, and do not fit into the standard target wheel. So a new aluminum target wheel with forty positions for the cathodes was manufactured at the VERA workshop.

### Pressing of the AgBr-powder on Cu-cathodes:

The required Cu cathodes were washed with distilled water and cleaned in an ultrasonic bath in  $\text{HNO}_3$  (for one minute) and then in isopropanol, diluted with distilled water. Afterwards, the cathodes were washed with distilled  $\text{H}_2\text{O}$  again and dried in an oven at 80 °C for several hours. Other tools (stamps, mortars, micro spoons, forceps) were also cleaned.

In a first step solid AgBr was pestled to powder in a mortar. Some mg of this powder were pressed into each Cu-sample-holder with a mechanical press and a force of approximately 200 N. A conical shaped polished stamp made of hardened stainless steel was used for the pressing.

### Pressing of the AgCl-powder on the AgBr backing:

After the pressing of the backing material the tools were cleaned again and the different AgCl materials were pestled in the mortar one after the other. The AgCl material was pressed into the sample-holders, beginning with the material with the lowest  $^{36}\text{Cl}$ -content, to avoid contamination of material with low  $^{36}\text{Cl}$ -content. Additionally, different micro-spoons were used for the different AgCl materials and the mortar and the stamp were washed with distilled water each time the material was changed. Approximately 1-4 mg of the AgCl material was put on the AgBr layer and pressed on the backing mechanically with a force of 60-80 N using a truncated stamp made of hardened stainless steel and a press.

The targets were stored in plastic or glass tubes. Different combinations of backing materials (AgBr from different batches) and AgCl material were used. Tab. 7.7 gives a summary of the sputter targets produced from irradiated samples.

Additionally to AgBr backings, Ta-plates on Al-cathodes were used as backing in previous Cl-beam-times at VERA. It was found that their sulfur background was higher than from the AgBr backing [Martschini, 2011]. One of my samples was pressed on a Ta backing but due to the high  $^{36}\text{Cl}/\text{Cl}$ -ratios, this higher sulfur background did not influence the precision of the measurement. For samples with lower  $^{36}\text{Cl}/\text{Cl}$ -ratio the choice of the right backing material is more important.

## 7 AMS-measurements and reference material

The  $^{36}\text{Cl}/^{35}\text{Cl}$ -ratios of the produced samples were measured in 6 beam-time sessions between March 2009 and April 2010. The final values were normalized relative to the standard ETH K381/4N ( $^{36}\text{Cl}/^{35}\text{Cl} = 2.26 \cdot 10^{-11}$  [Alfimov *et al.*, 2009]) from ETH Zürich. Neither the small uncertainty (0.35 %) given in [Alfimov *et al.*, 2009], nor the absolute uncertainty of the reference material were taken into account for further calculations. Blanks were used for background corrections, sulfur corrections (see section 7.2.2), for centering the targets relative to the Cs-beam and as tuning targets. In later beam-time sessions a cathode with a small drilling (1 mm in diameter) for AgCl blank material was used for the centering of the target wheel. The main challenge during all the beam-time sessions was to separate  $^{36}\text{Cl}$  from its stable isobar  $^{36}\text{S}$ . To achieve this aim high kinetic energies of the isotopes are advantageous. Measurements were performed with terminal voltages between 3.0 and 3.3 MV (10% above the nominal value of the tandem) and the 7+ charge state was chosen. This resulted in kinetic energies of 24.0 - 26.4 MeV for the  $\text{Cl}^{7+}$  ions. The actual choice of the terminal voltage for a measurement series depended on the accelerator status and the time required for the conditioning of the accelerator to higher voltages. A combination of an ionization chamber and a silicon strip detector was used to separate the two isobars by both, their different energy losses in a gas and their different residual energies.

In the following chapters the prearrangements for the measurements, the beam-tuning of VERA, the data processing and the evaluation of the measured AMS data will be described.

### 7.1 Prearrangements for the AMS measurement

The prearrangements included the proper positioning of the targets in the target-wheel in such a way, that possible cross contamination was minimized (targets with similar isotopic ratios in adjacent positions), mounting of the target wheel in the source S1, the tuning of the beam through the AMS facility, the positioning of the stripper foils and the setup of the particle detectors and their electronics.

#### 7.1.1 The tuning

The process to optimize the parameters of all the components of VERA to guide the ion beam from the source to the detector with minimal losses is called tuning. It is

done section by section for the isotopes of interest. The beam optical elements are scanned and optimized via current measurements with Faraday cups and beam profile monitors or via count-rate measurements in particle detectors. The  $^{36}\text{Cl}$  current is too small to be measured with Faraday cups, so in this work a pilot beam of stable  $^{37}\text{Cl}$  was used for the tuning from the source to FC 04 (Faraday cup 04, see fig. 7.1). For the tuning of the ion optical components between FC 04 and the strip detector and the final tuning, all ion optical components were scaled from mass 37u to 36u and finally the count-rate in the strip detector is maximized. The parameters of some ion optical components (e.g. MBS-, steerer-, ESA-voltages and the terminal voltage 7.1) can be optimized separately for four different masses, to allow fast sequencing (see section 4.2.2). These parameters are called register-dependent (reg0, reg1, reg2, reg3). During the first steps of the tuning, VERA is operated in maintenance mode, i.e. not switching between the registers. If the facility is operated in norm mode (during measurements) it switches quickly (milliseconds) between the registers, which leads to injection of isotopes with different masses into the accelerator. These register-dependent parameters were also optimized during the tuning by maximizing  $^{35}\text{Cl}^{7+}$  and  $^{37}\text{Cl}^{7+}$  currents in the offset Faraday cups MFC 04-2 and MFC 04-3 after the analyzing magnet BM 03 (see fig. 7.1).

### Setup of the ion source

The initial settings for the source parameters are based on empirical data from previous measurements. These parameters are: the line heater (LNH 01), which controls the temperature of the cesium capillary (which connects the Cs oven and the ionizer) and regulates the amount of cesium reaching the source, the ionizer power (ION S1), regulating the temperature on the tantalum surface where the cesium is ionized, the potential of the cathode (CAT S1), which accelerates the  $\text{Cs}^+$  ions to the target, the voltage applied to the cesium Einzel lens (CSF S1) which focuses the  $\text{Cs}^+$  beam, the extracting voltage (EXT S1), the voltage of the source Einzel lens (FOC S1) and the high voltage of the source (HSV S1) (pre-acceleration). The last three parameters are for accelerating and focusing the extracted ion beam. Due to the self sputtering effect of chlorine the extracted  $\text{Cl}^-$  current was regulated automatically by adapting the ionizer power [Steier *et al.*, 2010].

### Initial tuning of the low-energy side and adjustment of the high-energy side

Empirical values from previous measurements were used as starting points for the tuning. For the following tuning steps ions of mass 37u were used ( $^{37}\text{Cl}^-$  ions). The location of the beam optical elements and the beam analyzing instruments can be found in fig. 7.1. The current measured in FC 02 was maximized with respect to the voltage applied to the low-energy side ESA (ESA 01). In the next step the target wheel was centered by scanning the ion current in FC 02 with respect to the x- (horizontal) and y (vertical)-position of the centering target. Independent scans of the current measured in FC 03 (after the tandem accelerator) for different voltages

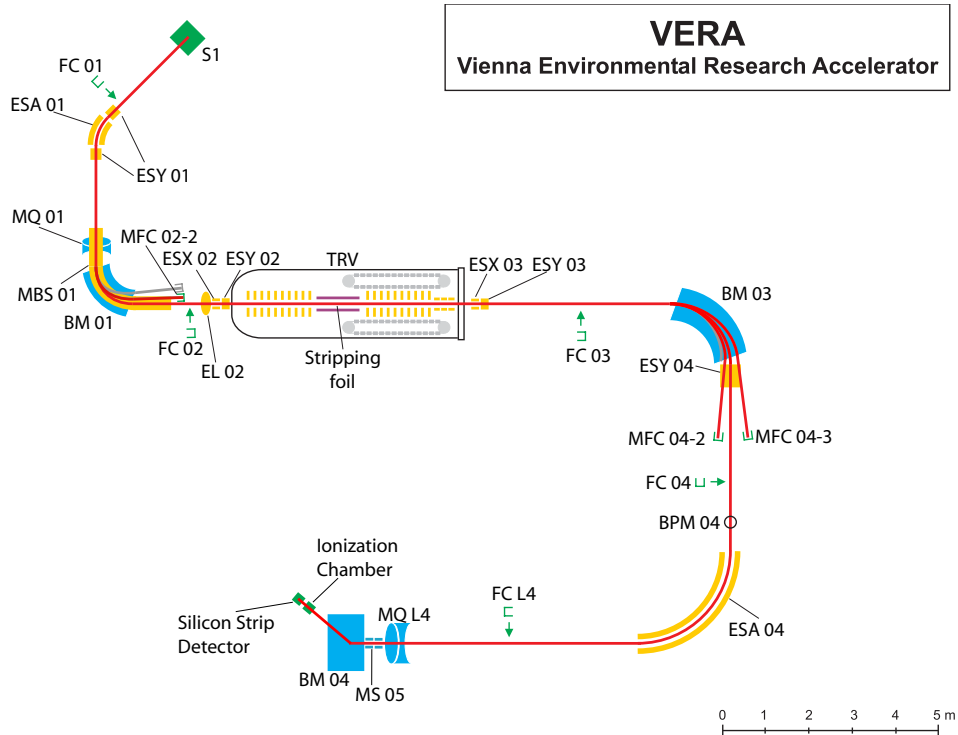


**Figure 7.1:** Schematic view of VERA, which shows the ion source S1, the beam optical components, used in my the measurements (electrostatic analyzers (ESA), electrostatic steerers for horizontal- (ESX) and vertical-direction (ESY), multi beam switcher (MBS), electrostatic lens (EL), the terminal of the tandem accelerator (TRV), magnetic quadrupoles (MQ) and magnetic steerers) and Faraday cups (FC and MFC), beam profile monitors (BPM), the ionization chamber and the silicon strip detector. The injector magnet (BM 01), the analyzing magnet (BM 03) and the switching magnet (BM 04) are also shown.

applied to the steerers ESX 02 and ESY 02, and the MBS 01-1reg3 were performed to find optimal values. The current in FC 04 (after the analyzing magnet) was maximized by optimizing the settings for the ESA 01, the multi beam switcher for mass 37u (MBS 01 reg3), the cesium focus (FOC S1) and the electrostatic steerers, magnetic quadrupoles, and Einzel lens on the low-energy side (before accelerator). Because the individual components are not independent from each other an optimized combination of the settings had to be found. This was done automatically by a program called AUTOMAX developed by [Steier, 2000].

The beam on the high-energy side is centered by means of a beam profile monitor (BPM 04), by varying the terminal voltage (centering in horizontal-direction) and the voltage applied to ESY 03 (centering in vertical-direction). The ion current of mass 37u in FC L4 is maximized by optimizing the voltage applied to the ESA 04 (high-energy side electric analyzer) and ESY 04.

In the next step the mass 35u current is maximized in the offset Faraday cup MFC

02-2 by optimizing MBS 01reg2. The  $^{35}\text{Cl}^{7+}$ -current in MFC 04-2 is maximized, by optimizing MBS 01reg0 and reg0 of the electrostatic steerers at the low-energy side. MBS 01reg1 is optimized by maximizing the  $^{37}\text{Cl}^{7+}$  current in MFC 04-3. These currents are necessary for the determination of the transmission through the accelerator (see text below) and serve as control parameters during the measurement.

### Tuning of the high-energy side

For the tuning of the high-energy side we switched from gas to foil-stripping and the electric components were scaled from the  $^{37}\text{Cl}^{7+}$  pilot beam to mass 36 in the charge state 7+. Both detectors (ionization chamber and silicon strip detector) were set into operation mode. The ionization chamber was filled with 45-55 mbar (see tab. 7.1) of isobutane ( $\text{C}_4\text{H}_{10}$ ) or with 70 mbar of an isobutane argon-methane mixture (beam-time session in April 2010), which served as counting gas. The density of the gas needs be constant during a measurement. A varying gas density changes the position of the  $^{36}\text{S}$ - and the  $^{36}\text{Cl}$ -peak in the energy spectrum and complicates the separation of the close-lying peaks. The setup of the data processing is described in section 7.1.3.

The tuning of the high-energy side was done by maximizing the  $^{36}\text{S}$  count-rate in the strip detector. Attention had to be paid to the count-rate. It should be in the range of several 1000 counts per second, to not overload the strip detector while keeping the time needed for the count-rate tuning acceptable. This was achieved with an attenuated  $^{36}\text{S}$  beam, extracted from a steel target. An attenuator may also change the profile of the beam, therefore, AgCl-blank targets, which gave a  $^{36}\text{S}$  count-rate of some hundred counts per second, were also used. With the AUTOMAX-program the values for the high-energy ESA (ESA 04), the electrostatic steerer ESY 04, the magnetic quadrupoles MQ L4 and the magnetic steerers MS 05 (horizontal- and vertical-direction) were optimized, via maximizing the count-rate in the strip detector. In an additional AUTOMAX-tuning the ESA 04, MS 05X, ESX 03 and the terminal voltage were optimized by maximizing the  $^{36}\text{S}$  count-rate. In a final AUTOMAX-tuning ESY 04, MSY 05 and ESY 03 were optimized.

### The particle transmission

At the end of the tuning the transmission was checked. The transmission  $T$  gives the percentage of the ions entering the accelerator which are detected in the selected charge state at the high-energy side. In our case it is given by the ratio of the number of  $^{35}\text{Cl}^{7+}$  ions measured e.g. as current in the high-energy offset Faraday cup MFC 04-2 and the number of  $^{35}\text{Cl}^-$  ions measured as current in the low-energy offset Faraday cup MFC 02-2.

$$T = \frac{N_{^{35}\text{Cl}^{7+}}}{N_{^{35}\text{Cl}^-}} = \frac{|I_{^{35}\text{Cl}^{7+}}|}{7 |I_{^{35}\text{Cl}^-}|} \quad (7.1)$$

Where  $N$  denotes the number of particles and  $I$  the current. Normally, the measurements were carried out at transmissions between 11 and 16 % for  $7^+$  ions. The transmission strongly depended on the stripper foil and on the residence time of the foil in the ion beam. At first it gets better with ongoing residence time (warming up), but then it reaches a maximum and drops due to the damage caused by the ion beam.

### 7.1.2 The settings

Component	Value
ESA 01	$\pm 11.30$ kV
BM 01	5297 G
TRV	3.302 MV
BM 03	4945 G
ESA 04	$\pm 84.04$ kV
BM 04	8978 G

**Table 7.1:** Example for the settings of the main components of the accelerator for mass 36. (beam-time session Feb. 2010).

### 7.1.3 Electronic signal processing

Canberra HV 3102D and Ortec 556 HV high voltage power supplies were used for the two detectors. The signals from both anodes (see section 4.2.5) in the ionization chamber and the eight signals from the silicon strip detector (4 position - and 4 energy signals) were digitized, analyzed and counted by the controlling computer of VERA if a gate for the signals was created (see fig. 7.2). The Ortec 550A SCA (single channel analyzer), the Ortec GG8010 (gate generator), the Pegelwandler WW/UR 381, the sequencer (AXEL GATE 1-8) and the Ortec C04020 Quad 4-input logic assured that a gate for the signals was only created if one of the detectors registered an event, and if VERA was in the right register for count-rate measurements (see section 7.1.1). The signal from the silicon strip detector is used as trigger for the gates because it is faster than the signals from the ionization chamber. During the count-rate tuning of the high-energy side the Ortec quad logic was bypassed (see tune gate in fig. 7.2 and only signals from the strip detector were counted with the ratemeter (Ortec 449). For my measurements only the energy signals from the ionization chamber (ADC1, ADC2) and the residual energy of the ions measured with the silicon strip detector (ADC3) were important.

The data from the three important ADCs was displayed and analyzed in two dimensional histograms (see fig. 7.3).

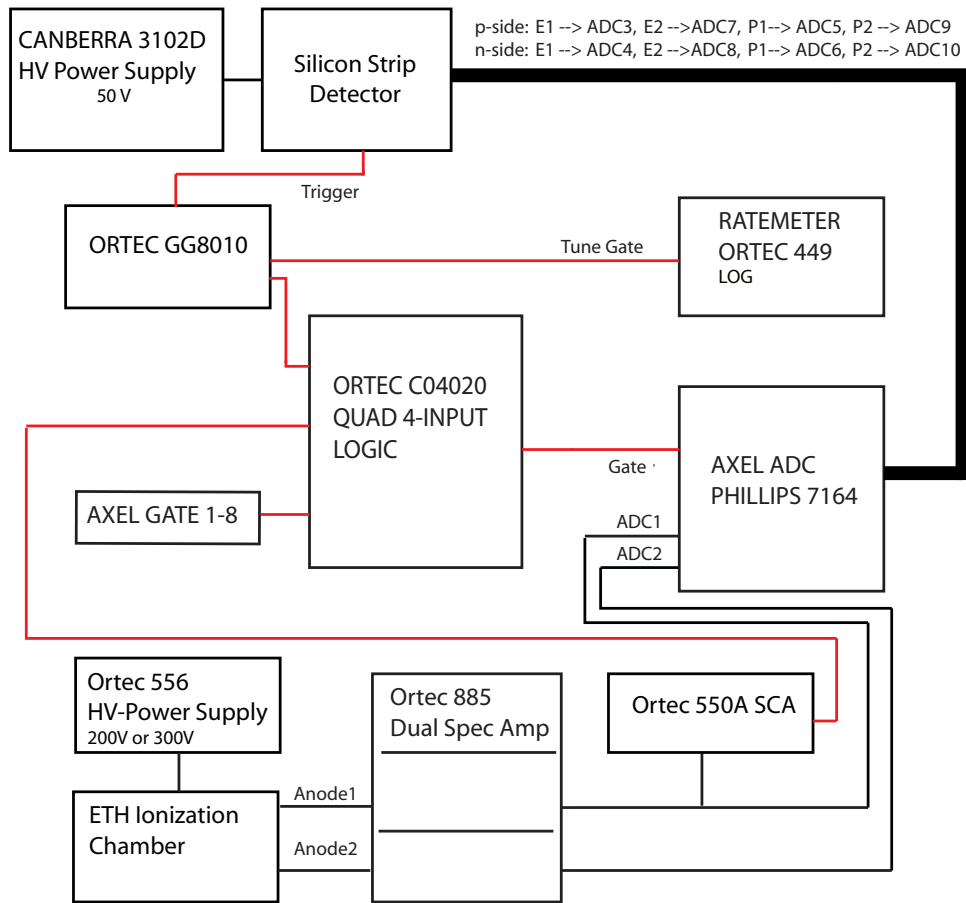


**Figure 7.2:** Simplified schematic view of the signal processing electronics (based on a fig. from Martschini). The connections for the energy and position signals from the silicon strip detector and for the energy signals from the ionization chamber are shown in black. The connections for the gate signals are shown in red. The Ortec 550A SCA analyzes the signal from the first anode of the ionization chamber and gives an output signal if the amplitude of the incoming signal is higher than a predefined lower level. The Pegelwandler and the Ortec GG8010 transform the incoming gate signals to fast negative impulses. The Ortec C04020 Quad 4-input logic assures that a gate is created only for times the sequencer is set to mass 36 (injecting and counting of  $^{36}\text{Cl}$ ).

## 7.2 Measuring the $^{36}\text{Cl}/^{35}\text{Cl}$ -ratio

### 7.2.1 Measured data

In a beam-time session several measurements (runs) were performed on each cathode. A run is divided into cycles (in my case 1000-5000). During a cycle, which lasted approximately 0.20 s, the counts dominantly from particles with mass 36u (registered with the ionization chamber ( $C_{ion}$ ) and the strip detector ( $C_{strip}$ )), the low-energy

side  $^{35}\text{Cl}^-$  current ( $I_{^{35}\text{Cl}}^{le,cy}$ )<sup>1</sup>, the high-energy side  $^{35}\text{Cl}^{7+}$  current ( $I_{^{35}\text{Cl}}^{he,cy}$ ) and the high-energy side  $^{37}\text{Cl}^{7+}$  current ( $I_{^{37}\text{Cl}}^{he,cy}$ ) were measured by switching between the registers. The mass "36u" counts were measured most of the time of a cycle (0.196 s). The advantage of dividing a run into short measurement periods is, that these cycles can be controlled independently by some parameters and "bad" cycles can be removed automatically.

With the help of  $^{36}\text{Cl}$  blank-material, bins (regions of interest) for  $^{36}\text{Cl}$  and  $^{36}\text{S}$  were set in the two dimensional  $\Delta E_1 - \Delta E_2$  histograms. This allowed the identification of  $^{36}\text{Cl}$  and  $^{36}\text{S}$  events, although the peaks were not completely separated (see fig 7.3). The number of counts in the bin for  $^{36}\text{Cl}$  during a cycle will be denoted as  $C_{^{36}\text{Cl}}^{cy}$  and the counts in the sulfur bin will be denoted as  $C_{^{36}\text{S}}^{cy}$ .

To get the raw data for a run ( $C_{^{36}\text{Cl}}$ ,  $C_{^{36}\text{S}}$ ,  $C_{ion}$ ,  $C_{strip}$ ,  $I_{^{35}\text{Cl}}^{le}$ ,  $I_{^{35}\text{Cl}}^{he}$  and  $I_{^{37}\text{Cl}}^{he}$ ) one has to sum counts or take the average currents of the raw data of all "good" cycles of the run. Poisson statistic was assumed as random uncertainty for the number of counted events. The uncertainties of the current measurement were neglected. An example for the raw data of several runs on a sample is given in tab. 7.2.

The life-time of the detector ( $t_{life}$ ) was also taken into account. Another important value is the transmission of the ions through the ionization chamber  $\varepsilon_{strip}$  (percentage of ions which is detected in the ionization chamber and also in the strip detector.)

$$\varepsilon_{strip} = \frac{C_{strip}^{cy}}{C_{ion}^{cy}} \quad (7.2)$$

From these raw data a first  $^{36}\text{Cl}/^{35}\text{Cl}$  isotope ratio was calculated (see tab.7.3).

From the measured high-energy side currents (see tab. 7.2), the  $^{37}\text{Cl}/^{35}\text{Cl}$ -ratio was calculated. It was measured in the range of 0.289-0.296. This is 9.7-7.5 % lower than the natural  $^{37}\text{Cl}/^{35}\text{Cl}$ -ratio of 0.320(3) [NNDC, 2005]. For AMS reference materials the same  $^{37}\text{Cl}/^{35}\text{Cl}$ -ratios were measured and so this systematic difference is taken into account (cancels) during the normalization to the reference material (see section 7.2.2, page 86).

<sup>1</sup>Measured quantities of single cycles will be indicated with cy. Currents measured on the low-energy side will be indicated with le and currents measured on the high-energy side with he.

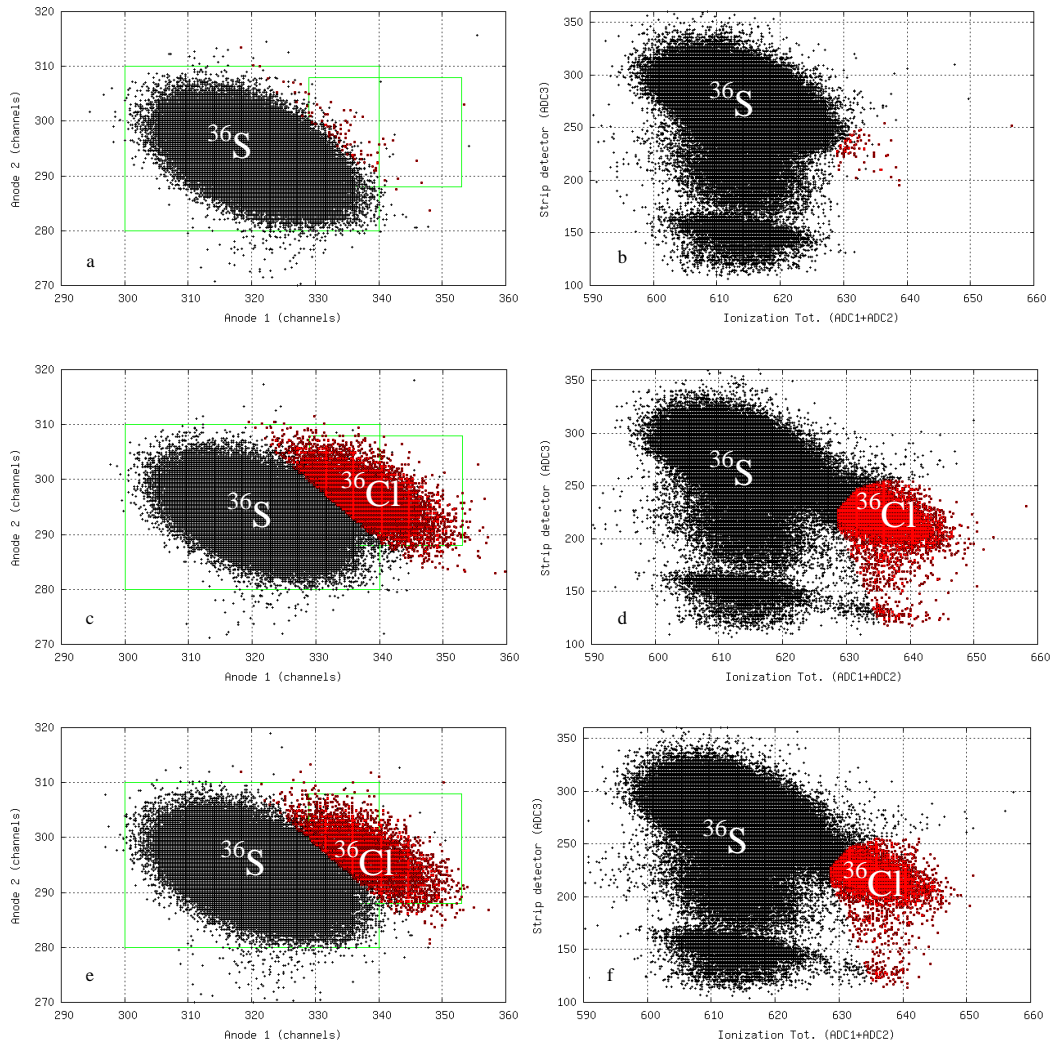


**Figure 7.3:** Two dimensional energy-spectra of (upper row) blank- ( $\alpha$ -blank), (middle row) reference- (ETH) and (lower row) neutron irradiated material (KIT1). The spectra on the left side show the energy loss of the ions in the area covered by anode 1 of the ionization chamber against their energy loss in the area covered by anode 2. In the spectra on the right side the total energy deposit (Ionization Tot. (ADC1+ADC2)) of the ions in the ionization chamber (x-axis) is plotted against their residual energy measured by the strip detector (y-axis). All energies are given in units of channels. The data was taken in the beam-time session in Apr. 2010.

Runs on KIT1 (25keV, neutron-activated sample)								
run	$t_{life}$ [s]	$C_{^{36}\text{Cl}}$ [counts]	$C_{^{36}\text{S}}$ [counts]	$I_{^{35}\text{Cl}}^{he}$ [ $\mu\text{A}$ ]	$I_{^{35}\text{Cl}}^{he}$ [ $\mu\text{A}$ ]	$I_{^{37}\text{Cl}}^{he}$ [ $\mu\text{A}$ ]	$C_{ion}$ [counts]	$C_{strip}$ [counts]
266	392	6404	482467	4.08	3.69	1.07	497186	398538
297	394	6969	276149	4.21	3.76	1.09	288723	230262
328	399	6355	197582	4.01	3.51	1.02	208524	165744
359	399	6076	169965	4.16	3.59	1.04	180354	142258
390	396	6243	186574	4.15	3.58	1.05	197362	154681
421	395	6739	191683	4.37	3.71	1.09	203084	160312
452	399	6706	169396	4.52	3.76	1.11	180732	142135
483	400	6002	149239	4.14	3.38	1.00	159077	125288
514	399	6643	188785	4.60	3.67	1.09	200091	157507
545	399	6135	179846	4.55	3.57	1.06	190312	148721

**Table 7.2:** Measured raw data on cathode KIT1 from Apr. 2010. The variables used in the table are described on page 83. Poisson statistics was assumed as random uncertainty for the number of counted events. The uncertainties of the other quantities were neglected.

## 7.2.2 Preconsiderations and Corrections

### Sulfur correction

Even with maximum particle energies of 28.4 MeV, the  $^{36}\text{Cl}$  and the  $^{36}\text{S}$  peaks in the two dimensional histograms were overlapping (see fig 7.3) and sulfur events were counted as "chlorine". To correct for these additional counts the sulfur correction factor ( $f_{sup}$ ) was introduced. This factor is the ratio of the counts in the  $^{36}\text{Cl}$ -bin to the total sulfur counts on blank materials (no  $^{36}\text{Cl}$  counts expected,  $f_{sup} = (\text{number of sulfur counts counted as "chlorine"}/\text{total number of sulfur counts})$ ). It was determined in such a way, that the final mean  $^{36}\text{Cl}/^{35}\text{Cl}$ -ratios (ratios after all corrections) of the blank materials of a measurement equal zero within their uncertainties. The sulfur corrected chlorine counts are then given by:

$$C_{^{36}\text{Cl},S} = C_{^{36}\text{Cl}} - f_{sup} * C_{^{36}\text{S}} \quad (7.3)$$

In the following, absolute uncertainties will be denoted as  $\delta$  with their associated quantity in parenthesis. The uncertainty of  $C_{^{36}\text{Cl},S}$  was calculated according to Gaussian error propagation, considering the uncertainties of chlorine and sulfur counts ( $\delta(C_{^{36}\text{Cl}})$ ,  $\delta(C_{^{36}\text{S}})$ ). The uncertainty of  $f_{sup}$  was not considered, because it has no significant influence to the final results of my samples. The uncertainty of the sulfur correction factor, which was in the order of  $10^{-5}$ , would have had to be 30%, to cause an additional uncertainty of 1% in the final results for the isotopic ratios of my samples, which were in the range of  $(0.5-2.2)*10^{-11}$ .

$$\delta(C_{^{36}\text{Cl},S}) = \sqrt{[\delta(C_{^{36}\text{Cl}})]^2 + f_{sup}^2 * [\delta(C_{^{36}\text{S}})]^2} \quad (7.4)$$

According to Poisson statistics  $\delta(C_{36S}) = \sqrt{C_{36S}}$  and  $\delta(C_{36Cl}) = \sqrt{C_{36Cl}}$ , but in the case of  $C_{36Cl}$ ,  $\sqrt{C_{36Cl} + 1}$  was assumed as uncertainty, to not underestimate this uncertainty on runs with a low number of chlorine events (runs on blank material). In the next step the sulfur corrected  $^{36}\text{Cl}/^{35}\text{Cl}$ -ratio and its uncertainty were calculated by:

$$\left(\frac{^{36}\text{Cl}}{^{35}\text{Cl}}\right)_S = \frac{C_{36Cl,S}}{\frac{I_{35Cl}^{he} \cdot t_{life}}{qe}} \quad (7.5)$$

$$\delta\left(\left(\frac{^{36}\text{Cl}}{^{35}\text{Cl}}\right)_S\right) = \frac{\delta(C_{36Cl,S})}{\frac{I_{35Cl}^{he} \cdot t_{life}}{qe}} \quad (7.6)$$

Where  $q = 7+$  is the charge state and  $e$  is the elemental charge. The uncertainties of  $I_{35Cl}^{he}$ ,  $t_{life}$ ,  $q$  and  $e$  are negligible and were not considered in further calculations.

### Normalization to standard

At least two sputter targets of the same AMS reference material (with known isotopic ratio) were used in all beam-times. The normalization factor  $f_n$  was determined for each turn<sup>2</sup>:

$$f_n = \frac{\mathcal{S}_{nom}}{\left\langle \left(\frac{^{36}\text{Cl}}{^{35}\text{Cl}}\right)_S \right\rangle_{stand}} \quad (7.7)$$

$\mathcal{S}_{nom}$  is the nominal  $^{36}\text{Cl} / ^{35}\text{Cl}$ -ratio of the standard and  $\left\langle \left(\frac{^{36}\text{Cl}}{^{35}\text{Cl}}\right)_S \right\rangle_{stand}$  is the weighted mean of the  $^{36}\text{Cl} / ^{35}\text{Cl}$ -ratios measured on all cathodes with the same standard material within a single turn. In equations 7.8, 7.9 and 7.10  $n$  is the number of runs within a turn on a certain standard material.

$$\left\langle \left(\frac{^{36}\text{Cl}}{^{35}\text{Cl}}\right)_S \right\rangle_{stand} = \frac{\sum_{i=1}^n \frac{1}{\delta\left(\left(\frac{^{36}\text{Cl}}{^{35}\text{Cl}}\right)_{S,i}\right)^2} \left(\frac{^{36}\text{Cl}}{^{35}\text{Cl}}\right)_{S,i}}{\sum_{i=1}^n \frac{1}{\delta\left(\left(\frac{^{36}\text{Cl}}{^{35}\text{Cl}}\right)_{S,i}\right)^2}} \quad (7.8)$$

The internal (statistical) and external (scatter of individual runs) uncertainties of the  $\left\langle \left(\frac{^{36}\text{Cl}}{^{35}\text{Cl}}\right)_S \right\rangle_{stand}$  were calculated:

$$\delta_{int}\left(\left\langle \left(\frac{^{36}\text{Cl}}{^{35}\text{Cl}}\right)_S \right\rangle_{stand}\right) = \sqrt{\frac{1}{\sum_{i=1}^n \frac{1}{\delta\left(\left(\frac{^{36}\text{Cl}}{^{35}\text{Cl}}\right)_{S,i}\right)^2}}} \quad (7.9)$$

---

<sup>2</sup>A turn is a repeated measuring sequence on several cathodes. Normally at least one run on each relevant target (standards, blanks, unknown samples) is performed, before starting the next sequence on this set of samples.

$$\delta_{ext}\left(\left\langle\left(\frac{^{36}\text{Cl}}{^{35}\text{Cl}}\right)_S\right\rangle_{stand}\right) = \sqrt{\frac{\sum_{i=1}^n \left[ \frac{(\frac{^{36}\text{Cl}}{^{35}\text{Cl}})_{S,i} - \left\langle\left(\frac{^{36}\text{Cl}}{^{35}\text{Cl}}\right)_S\right\rangle_{stand}}{\delta((\frac{^{36}\text{Cl}}{^{35}\text{Cl}})_{S,i})} \right]^2}{(n-1) \sum_{i=1}^n \frac{1}{\delta((\frac{^{36}\text{Cl}}{^{35}\text{Cl}})_{S,i})^2}}} \quad (7.10)$$

For further calculations the maximum of these two uncertainties ( $\delta(\left\langle\left(\frac{^{36}\text{Cl}}{^{35}\text{Cl}}\right)_S\right\rangle_{stand})$ ) was used. The uncertainty of the normalization factor was calculated by:

$$\delta(f_n) = f_n \frac{\delta(\left\langle\left(\frac{^{36}\text{Cl}}{^{35}\text{Cl}}\right)_S\right\rangle_{stand})}{\left\langle\left(\frac{^{36}\text{Cl}}{^{35}\text{Cl}}\right)_S\right\rangle_{stand}} \quad (7.11)$$

Each  $(\frac{^{36}\text{Cl}}{^{35}\text{Cl}})_S$ -ratio was multiplied with the normalization factor for the respective turn. The normalized and sulfur corrected  $^{36}\text{Cl}/^{35}\text{Cl}$ -ratios ( $(\frac{^{36}\text{Cl}}{^{35}\text{Cl}})_{S,n}$ ) and their uncertainties were then calculated by <sup>3</sup>:

$$\left(\frac{^{36}\text{Cl}}{^{35}\text{Cl}}\right)_{S,n} = f_n * \left(\frac{^{36}\text{Cl}}{^{35}\text{Cl}}\right)_S \quad (7.12)$$

$$\delta\left(\left(\frac{^{36}\text{Cl}}{^{35}\text{Cl}}\right)_{S,n}\right) = \left(\frac{^{36}\text{Cl}}{^{35}\text{Cl}}\right)_{S,n} * \sqrt{\left[\frac{\delta(f_n)}{f_n}\right]^2 + \left[\frac{\delta\left(\left(\frac{^{36}\text{Cl}}{^{35}\text{Cl}}\right)_S\right)}{\left(\frac{^{36}\text{Cl}}{^{35}\text{Cl}}\right)_S}\right]^2} \quad (7.13)$$

To ensure reasonable measurement results, some parameters were checked for each run:  $I_{^{35}\text{Cl}}^{le}$  had to be within a certain range (maximal two times the mean  $I_{^{35}\text{Cl}}^{le}$  current of the respective beam-time, see tab. 7.4), the  $^{36}\text{S}/^{35}\text{Cl}$  value had to be smaller than  $2 \cdot 10^{-9}$  (this value was defined as "sulfur threshold value" ( $S_{th}$ )) and the yield had to be bigger than 10 %. Runs which did not satisfy these conditions were not considered for further evaluations.

Tab. 7.4 lists quality and measurement parameters for all measurement series of this work.

From the data of the "good" runs the weighted mean of the normalized and sulfur corrected  $^{36}\text{Cl}/^{35}\text{Cl}$ -ratio for one target and its internal (statistical) and external (scatter of individual runs) uncertainty were then calculated by:

$$\left\langle\left(\frac{^{36}\text{Cl}}{^{35}\text{Cl}}\right)_{S,n}\right\rangle = \frac{\sum_{i=1}^R \frac{1}{\delta((\frac{^{36}\text{Cl}}{^{35}\text{Cl}})_{S,n,i})^2} \left(\frac{^{36}\text{Cl}}{^{35}\text{Cl}}\right)_{S,n,i}}{\sum_{i=1}^R \frac{1}{\delta((\frac{^{36}\text{Cl}}{^{35}\text{Cl}})_{S,n,i})^2}} \quad (7.14)$$

<sup>3</sup>In fact, the nominal value of the standard ETH K381/4N was originally given as  $^{36}\text{Cl}/\text{Cl}$ -ratio where Cl stands for both stable chlorine isotopes ( $^{35}\text{Cl}$  and  $^{37}\text{Cl}$ ). This value can be easily converted into a  $^{36}\text{Cl}/^{35}\text{Cl}$ -ratio by dividing it by the natural abundance of  $^{35}\text{Cl}$  (see page 4).

Runs on KIT1 (25keV, neutron-activated sample)								
run	$\frac{^{36}\text{Cl}}{^{35}\text{Cl}}$ [ $10^{-12}$ ]	$C_{^{36}\text{Cl},S}$ [counts]	$(\frac{^{36}\text{Cl}}{^{35}\text{Cl}})_S$ [ $10^{-12}$ ]	$f_n$	$(\frac{^{36}\text{Cl}}{^{35}\text{Cl}})_{S,n}$ [ $10^{-12}$ ]	$T$ [%]	$\frac{^{36}\text{S}}{^{35}\text{Cl}}$ [ $10^{-10}$ ]	$\varepsilon_{strip}$ [%]
266	4.98±0.062	6368±80	4.95±0.06	1.61±0.01	7.99±0.11	12.9	3.75	80.2±0.2
297	5.28±0.063	6948±83	5.26±0.06	1.61±0.02	8.47±0.15	12.8	2.09	79.8±0.3
328	5.09±0.064	6340±80	5.08±0.06	1.65±0.01	8.37±0.12	12.5	1.58	79.5±0.3
359	4.75±0.061	6063±78	4.74±0.06	1.65±0.01	7.81±0.11	12.3	1.33	78.9±0.4
390	4.95±0.063	6229±79	4.94±0.06	1.74±0.03	8.58±0.18	12.3	1.48	78.4±0.3
421	5.16±0.063	6725±82	5.15±0.06	1.76±0.03	9.04±0.17	12.1	1.47	78.9±0.3
452	5.01±0.061	6693±82	5.00±0.06	1.75±0.01	8.74±0.12	11.9	1.27	78.6±0.4
483	4.98±0.064	5991±77	4.97±0.06	1.67±0.01	8.29±0.12	11.7	1.24	78.8±0.4
514	5.08±0.062	6629±82	5.07±0.06	1.73±0.02	8.80±0.16	11.4	1.45	78.7±0.3
545	4.83±0.062	6122±78	4.82±0.06	1.76±0.04	8.49±0.21	11.2	1.42	78.1±0.3

**Table 7.3:** Sulfur corrected ( $(\frac{^{36}\text{Cl}}{^{35}\text{Cl}})_S$ ) and normalized ( $(\frac{^{36}\text{Cl}}{^{35}\text{Cl}})_{S,n}$ )  $^{36}\text{Cl}/^{35}\text{Cl}$ -ratios from the runs on KIT1 from Apr. 2010.  $T$  is the transmission through the accelerator,  $\varepsilon_{strip}$  is the transmission through the ionization chamber and  $f_n$  is the normalization factor. Each run in the table is from a different turn.

$$\delta_{int}\left(\left\langle\left(\frac{^{36}\text{Cl}}{^{35}\text{Cl}}\right)_{S,n}\right\rangle\right) = \sqrt{\frac{1}{\sum_{i=1}^R \frac{1}{\delta\left(\left(\frac{^{36}\text{Cl}}{^{35}\text{Cl}}\right)_{S,n,i}\right)^2}}} \quad (7.15)$$

$$\delta_{ext}\left(\left\langle\left(\frac{^{36}\text{Cl}}{^{35}\text{Cl}}\right)_{S,n}\right\rangle\right) = \sqrt{\frac{\sum_{i=1}^R \left[\frac{\left(\frac{^{36}\text{Cl}}{^{35}\text{Cl}}\right)_{S,n,i} - \left\langle\left(\frac{^{36}\text{Cl}}{^{35}\text{Cl}}\right)_{S,n}\right\rangle}{\delta\left(\left(\frac{^{36}\text{Cl}}{^{35}\text{Cl}}\right)_{S,n,i}\right)}\right]^2}{(R-1) \sum_{i=1}^R \frac{1}{\delta\left(\left(\frac{^{36}\text{Cl}}{^{35}\text{Cl}}\right)_{S,n,i}\right)^2}}} \quad (7.16)$$

Where  $R$  is the number of runs on the particular target. For further calculations the maximum of the two uncertainties of each target ( $\delta\left(\left\langle\left(\frac{^{36}\text{Cl}}{^{35}\text{Cl}}\right)_{S,n}\right\rangle\right)$ ) was used.

### Correction for the transmission through the ionization chamber

In the following I will write  $\mathcal{S}_{S,n}$ ,  $\mathcal{L}_{S,n}$  and  $\mathcal{T}_{S,n}$  for the sulfur corrected and normalized mean  $^{36}\text{Cl}/^{35}\text{Cl}$ -ratio ( $\left\langle\left(\frac{^{36}\text{Cl}}{^{35}\text{Cl}}\right)_{S,n}\right\rangle$ ) of a standard, a blank and other targets.  $\mathcal{R}$  will stand for the normalized sulfur corrected weighted mean  $^{36}\text{Cl}/^{35}\text{Cl}$ -ratio of any target. The indices  $S$ ,  $n$ ,  $\varepsilon$ , and  $b$  will stand for sulfur corrected, normalized to standard, corrected for the transmission through the ionization chamber (see equ. 7.2) and blank corrected. The transmission through the ionization chamber appeared to be different for different targets (differences of about 2%). The correction for this difference was done by:

Beam time	No. of "good" runs	Counting gas	Pressure [mbar]	Terminal voltage [MV]	$\langle \varepsilon_{strip} \rangle$ [%]	$f_{sup}$ [ $10^{-5}$ ]	$I_{^{35}\text{Cl}}^{le,max}$ [ $\mu\text{A}$ ]
Mar. 2009	685	$\text{C}_4\text{H}_{10}$	45.0	3.00	65.00	4.21	2.0
Jul. 2009	326	$\text{C}_4\text{H}_{10}$	50.0	3.30	$68.14 \pm 0.05$	2.30	6.0
Sep. 2009/1	143	$\text{C}_4\text{H}_{10}$	55.0	3.30	$58.61 \pm 0.13$	3.01	7.0
Sep. 2009/2	576	$\text{C}_4\text{H}_{10}$	50.0	3.33	$69.24 \pm 0.08$	1.40	7.0
Nov. 2009	306	$\text{C}_4\text{H}_{10}$	45.0	3.00	$88.54 \pm 0.06$	3.76	7.0
Feb. 2010	367	$\text{C}_4\text{H}_{10}$	50.0	3.30	$89.63 \pm 0.09$	1.18	8.0
Apr. 2010	321	$\text{C}_4\text{H}_{10}$ +Ar+CH <sub>4</sub>	70.0	3.0	$78.93 \pm 0.08$	7.50	8.0

**Table 7.4:** Measurement parameters and control quantities for all beam-time sessions. These control parameters were set to identify "bad" runs and are described in the text on page 87. The data evaluation of the beam-time in Sep. 2009 was split because we measured with two different counting gas pressures. The uncertainty of the pressure in the ionization chamber was in the range of 0.1-0.2 mbar and was compensated in the evaluation. Due to the change of the distance of the strip detector to the ionization chamber (between Sept. and Nov. 2009) the geometrical losses of the beam were reduced and a higher percentage of the ions detected in the ionization chamber reached the strip detector. Normally, isobutane ( $\text{C}_4\text{H}_{10}$ ) was used as counting gas. Only in the last beam-time a mixture of  $\text{C}_4\text{H}_{10}$  and Ar+CH<sub>4</sub> was used. This gas is heavier and the angular straggling of the ions in the ionization chamber increased. Therefore, the transmission through the ionization chamber dropped, but the peak separation of the  $^{36}\text{Cl}$  and  $^{36}\text{S}$  was better.

$$\mathcal{R}_{S,n,\varepsilon} = \mathcal{R}_{S,n} \frac{\langle \varepsilon_{strip} \rangle}{\varepsilon_{strip}} \quad (7.17)$$

$$\delta(\mathcal{R}_{S,n,\varepsilon}) = \mathcal{R}_{S,n,\varepsilon} \sqrt{\left[ \frac{\delta(\mathcal{R}_{S,n})}{\mathcal{R}_{S,n}} \right]^2 + \left[ \frac{\delta(\varepsilon_{strip})}{\varepsilon_{strip}} \right]^2 + \left[ \frac{\delta(\langle \varepsilon_{strip} \rangle)}{\langle \varepsilon_{strip} \rangle} \right]^2} \quad (7.18)$$

Here  $\varepsilon_{strip}$  is the mean transmission through the ionization chamber for the runs on a particular target and  $\langle \varepsilon_{strip} \rangle$  is the transmission through the ionization chamber calculated by all runs on reference material (standards, normally two targets per beam-time)<sup>4</sup>. These two transmissions and their uncertainties were calculated by:

$$\varepsilon_{strip} = \frac{\sum_i C_{strip,i}}{\sum_i C_{ion,i}} \quad (7.19)$$

$$\delta(\varepsilon_{strip}) = \varepsilon_{strip} \sqrt{\left[ \frac{1}{\sum_i C_{ion,i}} \right]^2 + \left[ \frac{1}{\sum_i C_{strip,i}} \right]^2} \quad (7.20)$$

<sup>4</sup> $\langle \varepsilon_{strip} \rangle$  was a different constant for each beam-time.

$$\langle \varepsilon_{strip} \rangle = \frac{\sum_i C_{strip,i}}{\sum_i C_{ion,i}} \quad (7.21)$$

$$\delta(\langle \varepsilon_{strip} \rangle) = \langle \varepsilon_{strip} \rangle * \sqrt{\left[\frac{1}{\sum_i C_{ion,i}}\right]^2 + \left[\frac{1}{\sum_i C_{strip,i}}\right]^2} \quad (7.22)$$

In equ. 7.19 and 7.20 the summations are over all runs on a single target and in 7.21 and 7.22 the summations are over all runs on standard material. Tab. 7.6 shows that this correction is also negligible for my targets. The change from  $\mathcal{R}_{S,n}$  to  $\mathcal{R}_{S,n,\varepsilon}$  is within the uncertainty.

### Blank correction

At least two blank targets made of the same blank material<sup>5</sup> (see tab. 7.5) were used in each beam-time. For the blank correction, at first the weighted mean of the  $\mathcal{L}_{S,n,\varepsilon}$ -values (normalized and corrected weighted mean  $^{36}\text{Cl}/^{35}\text{Cl}$ -ratio of a blank) of all blanks and the maximum of its internal and external uncertainty were calculated. This was done in analogy to equations 7.14, 7.15, 7.16, This mean value and its uncertainty will be written as  $\langle \mathcal{L}_{S,n,\varepsilon} \rangle$  and  $\delta(\langle \mathcal{L}_{S,n,\varepsilon} \rangle)$ .

Beam time	Used blank material	No.	$\langle \mathcal{L}_{S,n,\varepsilon} \rangle$ [ $10^{-15}$ ]	Used ref. material	No.	$\mathcal{S}_{nom}$ [ $10^{-11}$ ]	$\mathbf{f}_n$
Mar. 2009	$\alpha$ -blank	3	$5.5 \pm 2.5$	ETH K381/4N	2	2.262	3.44-4.39
Jul. 2009	$\alpha$ -blank	2	$1.7 \pm 1.4$	DiluSe-II	5	0.167	2.35-5.34
	Br80	1					
	Br100	1					
Sep. 2009/1	$\alpha$ -blank	2	$6.8 \pm 2.2$	ETH K381/4N	2	2.262	2.51-4.33
Sep. 2009/2	$\alpha$ -blank	2	$7.4 \pm 1.0$	ETH K381/4N	2	2.262	2.60-2.70
Nov. 2009	$\alpha$ -blank	2	$6.7 \pm 0.6$	ETH K381/4N	2	2.262	1.68-2.11
Feb. 2010	$\alpha$ -blank	2	$5.1 \pm 0.9$	ETH K381/4N	2	2.262	1.57-1.78
Apr. 2010	$\alpha$ -blank	2	$17.0 \pm 0.9$	ETH K381/4N	2	2.262	1.61-1.79

**Table 7.5:** Blank and reference materials used in all beam-times. For informations on the blank materials see section 6, tab. 6.2 and 6.4. The third column gives the number of blank cathodes and the sixth column gives the number of standard cathodes.  $\langle \mathcal{L}_{S,n,\varepsilon} \rangle$  is the mean value of the corrected and normalized  $^{36}\text{Cl}/^{35}\text{Cl}$ -ratios of the blanks and  $\mathcal{S}_{nom}$  is the nominal  $^{36}\text{Cl}/^{35}\text{Cl}$ -ratios of the reference materials. The uncertainty of these nominal values was not considered for further calculations. In the last column the lowest and highest values for the normalization factor (changed from turn to turn) for the beam-times are listed.

The blank corrected isotopic ratio of a sample ( $\mathcal{R}_{S,n,\varepsilon,b}$ ) and its uncertainty were then calculated by:

<sup>5</sup> $^{36}\text{Cl}$ -blank material is material which contains no or negligible amounts of  $^{36}\text{Cl}$

$$\mathcal{R}_{S,n,\varepsilon,b} = \mathcal{R}_{S,n,\varepsilon} - \langle \mathcal{L}_{S,n,\varepsilon} \rangle \quad (7.23)$$

$$\delta(\mathcal{R}_{S,n,\varepsilon,b}) = \sqrt{[\delta(\mathcal{R}_{S,n,\varepsilon})]^2 + [\delta(\langle \mathcal{L}_{S,n,\varepsilon} \rangle)]^2} \quad (7.24)$$

These values for blanks and standards for all beam-times are listed in tab. 7.5.

In tab. 7.6 one can see, that the sulfur correction, the correction for the transmission of the ionization chamber and the blank correction had almost no effect on the  $^{36}\text{Cl}/^{35}\text{Cl}$ -ratio of my samples (the change is within the uncertainty of the measurements). But the corrections are important for samples with lower  $^{36}\text{Cl}/^{35}\text{Cl}$ -ratios (blanks). The normalization to a reference material increased the final  $^{36}\text{Cl}/^{35}\text{Cl}$ -ratios by factors of 1.6-5.3 (see tab. 7.5).

Targets during beam-time session Apr.2010						
Sample	n	$\mathcal{R}$ [ $10^{-12}$ ]	$\mathcal{R}_S$ [ $10^{-12}$ ]	$\mathcal{R}_{S,n}$ [ $10^{-12}$ ]	$\mathcal{R}_{S,n,\varepsilon}$ [ $10^{-12}$ ]	$\mathcal{R}_{S,n,\varepsilon,b}$ [ $10^{-12}$ ]
ETH/1@20	11	10.06±0.03	10.03±0.13	22.56±0.10	22.61±0.11	22.59±0.11
BUD2/1@25	10	4.91±0.02	4.90±0.06	10.91±0.07	10.93±0.08	10.91±0.08
KIT2/2@32	10	4.00±0.02	3.99±0.04	8.88±0.09	8.93±0.10	8.91±0.10
KIT1@33	10	5.01±0.02	4.99±0.05	11.05±0.16	11.01±0.16	10.99±0.16
ATI3/2@35	10	2.29±0.01	2.29±0.03	5.11±0.06	5.11±0.06	5.09±0.06
α-blank2@12	20	0.018±0.001	0.011±0.001	0.024±0.002	0.024±0.002	0.001±0.002

**Table 7.6:** Calculated isotopic ratios for some targets (beam-time session Apr. 2010). n is the number of "good" runs on the particular target. A number after the slash was used if more than one cathode of the same material was loaded into the ion source. The number behind the "@" indicates the position on the target wheel.  $\mathcal{R}$  is the weighted mean value of the  $^{36}\text{Cl}/^{35}\text{Cl}$ -ratios of all runs performed on a particular target (standard, blank or unknown sample). The indices S, n,  $\varepsilon$  and b denote sulfur corrected, normalized to reference material, transmission corrected (transmission through ionization chamber) and blank corrected, respectively. The data shows that all the correction factors are negligible for my samples, but they do matter for blanks and for targets with low isotopic ratios. In general the normalization reduced the scattering of the  $^{36}\text{Cl}/^{35}\text{Cl}$ -values, which can reduce the uncertainty of the mean value.

beam-time	Target name	$\overline{\mathcal{T}}_{S,\varepsilon,b,n}$ [ $10^{-12}$ ]	rel. unc. [%]
Mar. 2009	KIT1/1@11	10.44 ± 0.19	1.8
	KIT1/2@35	10.86 ± 0.13	1.2
Jul. 2009	ATI2/1@19	5.01 ± 0.10	1.9
	ATI3/1@20	4.98 ± 0.07	1.5
Jul. 2009	ATI2/2@22	5.26 ± 0.08	1.5
	KIT1/1@31	11.07 ± 0.14	1.3

continued on next page

beam-time	Target name	$\mathcal{T}_{S,\varepsilon,b,n}$ [ $10^{-12}$ ]	rel. unc. [%]
	KIT1/2@32	$11.28 \pm 0.14$	1.3
Sep. 2009/1	ATI2@20	$4.67 \pm 0.08$	1.7
	ATI3@21	$4.88 \pm 0.09$	1.8
Sep. 2009/2	ATI2@20	$4.55 \pm 0.05$	1.1
	ATI3@21	$4.75 \pm 0.04$	0.9
Nov. 2009	KIT1/1@18	$10.72 \pm 0.09$	0.8
	KIT1/2@19	$10.62 \pm 0.07$	0.7
	ATI3/1@20	$4.91 \pm 0.04$	0.8
	ATI3/2@21	$4.88 \pm 0.03$	0.7
	ATI2/1@22	$4.76 \pm 0.03$	0.6
	ATI2/2@23	$4.71 \pm 0.03$	0.7
Feb. 2010	BUD2/1@13	$10.66 \pm 0.06$	0.6
	BUD2/2@14	$10.68 \pm 0.07$	0.6
	BUD3/1@15	$9.73 \pm 0.07$	0.7
	BUD3/2@16	$9.71 \pm 0.08$	0.8
	BUD1/1@17	$7.62 \pm 0.06$	0.7
	BUD1/1@18	$7.77 \pm 0.08$	1.0
	KIT1@19	$10.76 \pm 0.11$	1.0
	KIT2/1@20	$8.79 \pm 0.06$	0.7
	KIT2/2@21	$8.78 \pm 0.05$	0.6
	ATI3@23	$4.93 \pm 0.04$	0.8
	ATI2@24	$4.73 \pm 0.03$	0.6
Apr. 2010	BUD1/1@24	$7.81 \pm 0.10$	1.3
	BUD2/1@25	$10.91 \pm 0.08$	0.7
	BUD3/1@26	$9.72 \pm 0.08$	0.9
	BUD1/2@27	$7.87 \pm 0.06$	0.8
	BUD2/2@28	$10.54 \pm 0.07$	0.7
	BUD3/2@29	$10.10 \pm 0.10$	1.0
	KIT2/1@31	$8.86 \pm 0.08$	0.9
	KIT2/2@32	$8.91 \pm 0.10$	1.1
	KIT1@33	$10.99 \pm 0.16$	1.5
	ATI3/1@34	$5.08 \pm 0.06$	1.1
	ATI3/2@35	$5.09 \pm 0.06$	1.1
	ATI2/1@36	$4.88 \pm 0.06$	1.2
	ATI2/2@37	$4.63 \pm 0.04$	1.0

**Table 7.7:** Corrected and normalized isotopic ratios for all targets during all beam-time session. For the nomenclature of the targets see tab. 7.6.

### Weighted means for the final $^{36}\text{Cl}/^{35}\text{Cl}$ -ratios of target materials

The final step in the evaluation of the AMS data was to calculate the mean isotopic ratios ( $(\frac{^{36}\text{Cl}}{^{35}\text{Cl}})_{\text{VERA}}$ ), usually by means of the reference material ETH K381/4N, for the different target materials. This was done by weighting and summing-up the data of all sputter targets of a particular material, analogous to the equations 7.14, 7.15 and 7.16. The reduced  $\chi^2$ -value (written as  $\chi_{red}^2$ ) and the reproducibility R, (relative uncertainty of an single measurement) of the results were calculated by:

$$\chi_{red}^2 = \frac{\delta_{ext}((\frac{^{36}\text{Cl}}{^{35}\text{Cl}})_{\text{VERA}})}{\delta_{int}((\frac{^{36}\text{Cl}}{^{35}\text{Cl}})_{\text{ETH}})} \quad (7.25)$$

$$R = 100 \frac{\delta((\frac{^{36}\text{Cl}}{^{35}\text{Cl}})_{\text{VERA}})}{((\frac{^{36}\text{Cl}}{^{35}\text{Cl}})_{\text{ETH}})} \sqrt{N} \quad (7.26)$$

Where N is the number of measured targets from a certain target material. The maximum of the internal and external uncertainty ( $\delta(\frac{^{36}\text{Cl}}{^{35}\text{Cl}})_{\text{VERA}}$ ) was used as final uncertainty for the  $(\frac{^{36}\text{Cl}}{^{35}\text{Cl}})_{\text{VERA}}$ -values.

The final result are summarized in the tables and figures in the next section.

### 7.2.3 Final AMS results and conclusions

Sample material	$(\frac{^{36}\text{Cl}}{^{35}\text{Cl}})_{\text{VERA}}$ [ $10^{-12}$ ]	$\chi_{red}^2$	R [%]
KIT1	$10.78 \pm 0.08$	2.0	2.0
KIT2	$8.81 \pm 0.03$	0.8	0.8
ATI2	$4.74 \pm 0.04$	3.1	2.8
ATI3	$4.91 \pm 0.04$	2.2	2.1
BUD1	$7.75 \pm 0.06$	1.8	1.6
BUD2	$10.69 \pm 0.07$	2.1	1.3
BUD3	$9.79 \pm 0.08$	2.0	1.6

**Table 7.8:** Final  $^{36}\text{Cl}/^{35}\text{Cl}$ -ratios for the neutron activated samples measured by AMS, and normalized to the reference material ETH K381/4N.

Sample material	$(\frac{^{36}\text{Cl}}{^{35}\text{Cl}})_{VERA}$ [ $10^{-12}$ ]	rel. unc. $(\frac{^{36}\text{Cl}}{^{35}\text{Cl}})_{VERA}$ [%]	$(\frac{^{36}\text{Cl}}{^{35}\text{Cl}})_{(n,\gamma)therm}$ [ $10^{-12}$ ]	rel. unc. $(\frac{^{36}\text{Cl}}{^{35}\text{Cl}})_{(n,\gamma)therm}$ [%]	$\frac{(\frac{^{36}\text{Cl}}{^{35}\text{Cl}})_{VERA}}{(\frac{^{36}\text{Cl}}{^{35}\text{Cl}})_{(n,\gamma)therm}}$
ATI2	4.74	0.92	5.23	2.41	0.912
ATI3	4.91	0.73	5.44	2.41	0.916
BUD1	7.75	0.80	7.78	2.39	1.008
BUD2	10.69	0.66	10.48	2.40	1.021
BUD3	9.79	0.82	9.53	2.39	1.037

**Table 7.9:** Comparison of the  $^{36}\text{Cl}/^{35}\text{Cl}$ -ratios measured by AMS (normalized to the reference material ETH K381/4N)  $(\frac{^{36}\text{Cl}}{^{35}\text{Cl}})_{VERA}$ , with calculated  $^{36}\text{Cl}/^{35}\text{Cl}$ -ratios deduced from neutron activations (using the well known thermal cross-section values for  $^{197}\text{Au}(n,\gamma)^{198}\text{Au}$  and  $^{35}\text{Cl}(n,\gamma)^{36}\text{Cl}$  (see chapter 2.31))  $(\frac{^{36}\text{Cl}}{^{35}\text{Cl}})_{(n,\gamma)therm}$ . For the BUD samples the values differ between 1-4 % and for the ATI samples about 9%.

Sample material	$\frac{(\frac{^{36}\text{Cl}}{^{35}\text{Cl}})_{VERA,sample}}{(\frac{^{36}\text{Cl}}{^{35}\text{Cl}})_{VERA,BUD1}}$	$\frac{(\frac{^{36}\text{Cl}}{^{35}\text{Cl}})_{(n,\gamma)therm,sample}}{(\frac{^{36}\text{Cl}}{^{35}\text{Cl}})_{(n,\gamma)therm,BUD1}}$
ATI2	0.61±0.01	0.67±0.02
ATI3	0.63±0.01	0.70±0.02
BUD1	1.00±0.01	1.00±0.02
BUD2	1.38±0.01	1.35±0.03
BUD3	1.26±0.01	1.23±0.03

**Table 7.10:** Comparison of the  $^{36}\text{Cl}/^{35}\text{Cl}$ -ratios measured by AMS (normalized to the reference material ETH K381/4N)  $(\frac{^{36}\text{Cl}}{^{35}\text{Cl}})_{VERA}$ , with calculated  $^{36}\text{Cl}/^{35}\text{Cl}$ -ratios deduced from neutron activations (using the well known thermal cross-section values for  $^{197}\text{Au}(n,\gamma)^{198}\text{Au}$  and  $^{35}\text{Cl}(n,\gamma)^{36}\text{Cl}$  (see chapter 2.31))  $(\frac{^{36}\text{Cl}}{^{35}\text{Cl}})_{(n,\gamma)therm}$ . The uncertainties were estimated from the systematical and statistical uncertainties of the  $(\frac{^{36}\text{Cl}}{^{35}\text{Cl}})_{VERA}$ - and  $(\frac{^{36}\text{Cl}}{^{35}\text{Cl}})_{(n,\gamma)therm}$ -ratios.

Tables 7.8, 7.9, 7.10 and fig. 7.4 show three things:

1. The reduced  $\chi^2$  demonstrates that the internal and external uncertainties of the measured  $(\frac{^{36}\text{Cl}}{^{35}\text{Cl}})_{VERA}$  are in the same order. The scattering of the measured values is larger than the statistical uncertainty.
2. The  $^{36}\text{Cl}/^{35}\text{Cl}$ -ratios measured by AMS, relative to the reference material ETH K381/4N and the  $^{36}\text{Cl}/^{35}\text{Cl}$ -ratios calculated from the neutron fluence (activity measurements of gold monitor foils) and the well-known thermal cross-section value of  $^{35}\text{Cl}(n,\gamma)^{36}\text{Cl}$  are in good agreement for the BUD samples. For samples BUD1 and BUD2 the values are consistent within their uncertainties of

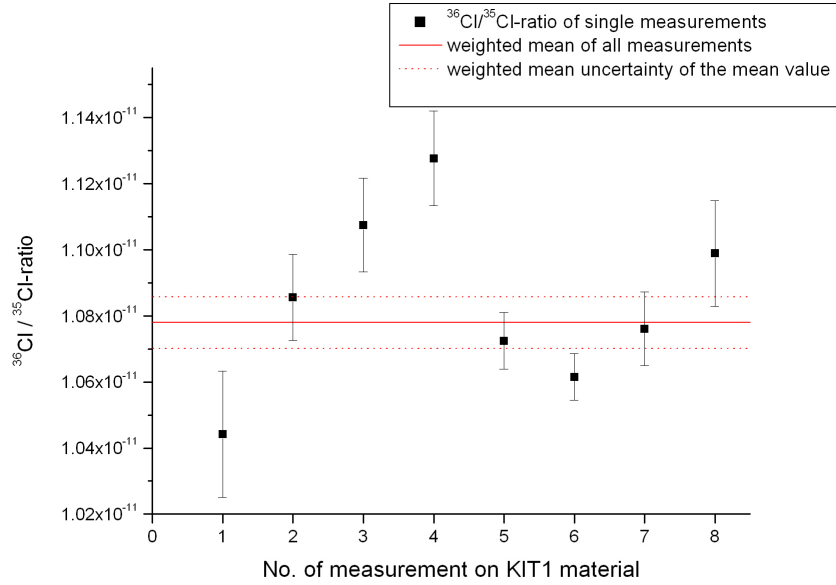


**Figure 7.4:** Comparison of the final results for KIT1 (25 keV neutron activated sample).

2-3%. Tab. 7.10 shows that the ratios between the  $(\frac{^{36}\text{Cl}}{^{35}\text{Cl}})_{VERA,samples}$  and  $(\frac{^{36}\text{Cl}}{^{35}\text{Cl}})_{VERA,BUD1}$  are consistent with the factors between the  $(\frac{^{36}\text{Cl}}{^{35}\text{Cl}})_{(n,\gamma)therm,samples}$  and  $(\frac{^{36}\text{Cl}}{^{35}\text{Cl}})_{(n,\gamma)therm,BUD1}$  for the BUD samples. The ratios are different for the ATI samples. The ratios between the  $(\frac{^{36}\text{Cl}}{^{35}\text{Cl}})_{VERA}$  values from the three BUD samples are equal to the  $(\frac{^{36}\text{Cl}}{^{35}\text{Cl}})_{(n,\gamma)therm}$ , within their uncertainties. The results from the AMS measurements on the BUD samples, which serve as AMS independent reference material, confirm the reference material ETH K381/4N.

3. The  $^{36}\text{Cl}/^{35}\text{Cl}$ -ratios of the ATI samples calculated from neutron-fluence and the well-known thermal neutron capture cross-section of  $^{35}\text{Cl}$  are not consistent with the results from AMS measurements using the ETH K381/4N standard for normalization. The fact that the  $(\frac{^{36}\text{Cl}}{^{35}\text{Cl}})_{VERA}$ -ratios are about 8-9 % lower than the  $(\frac{^{36}\text{Cl}}{^{35}\text{Cl}})_{(n,\gamma)therm}$  for both samples indicates a systematic deviation in the measurement. Due to the fact that this discrepancy only occurred for the ATI samples and the AMS measuring procedure was the same for the BUD and ATI samples, the different conditions during the neutron irradiations are most likely the source of this difference. As described in section 5.2.1 the neutron spectrum at ATI extends into the epithermal region. The neutron capture cross-section depends on the energy and for the calculation of the neutron fluence and the  $^{36}\text{Cl}/^{35}\text{Cl}$ -ratio only the thermal capture cross-section was considered. This would not matter, if the capture cross-section of all isotopes scales with  $1/v$

(like in nonresonant energy regions), because then the two factors would cancel. But as it can be seen in fig. 2.3 (gold, chlorine) there is a huge resonance in the neutron capture cross-section of  $^{197}\text{Au}$  at an energy of 5 eV and more resonances in the region of some 10 eV. These resonances lead to the overestimation of the neutron fluence, because the probability of capturing a neutron in the resonant energy regions is much bigger, than for pure thermal conditions. The overestimated fluence lead to a higher  $^{36}\text{Cl}/^{35}\text{Cl}$ -ratio, because  $^{35}\text{Cl}$  does not have resonances in the same energy region and the scaling factors for  $^{197}\text{Au}$  and  $^{35}\text{Cl}$  did not cancel.

## Conclusions

1. Five AMS reference materials were produced during the irradiations at the ATI and the BRR. These materials were compared to the reference material ETH K381/4N. This reference material is in agreement with the reference material produced in Budapest. The samples produced in Vienna show a systematic deviation of 8-9 % which is most probably caused by the non negligible contribution of epithermal neutrons at the TRIGA Mark II-reactor. To measure the fraction of epithermal neutrons, NaCl-samples with gold monitors shielded by cadmium and samples without Cd-shield should be irradiated at the ATI.  $^{113}\text{Cd}$  with a natural abundance of 12.22 % [Magill *et al.*, 2006] and a thermal neutron capture cross-section of  $2.06 \cdot 10^4$  barn [Magill *et al.*, 2006] would capture all thermal neutrons. The epithermal and thermal contribution to the neutron flux can be calculated from the measured activities of the gold foils and the capture cross-sections for thermal and epithermal neutrons of Au.
2. Differences between the calculated fluence values from the gold powder, the gold foils and the NaCl powder (see section 5.3.2) should be investigated by irradiating more (NaCl+Au)-pellets, of different thicknesses and equipped with gold foils, at the BRR. More targets would provide better statistics and an additional target which consists only of some thin gold foils would provide information on neutron scattering and neutron attenuation in the samples.

## 8 The MACS of $^{35}\text{Cl}$

### 8.1 Determination of the MACS

In order to calculate the Maxwellian averaged cross-section of  $^{35}\text{Cl}$  the experimental neutron capture cross-section was determined by combining the values for the neutron fluence (see section 5.3.2) of the KIT-samples and their isotopic ratios with the following equation:

$$\sigma_{exp} = \left(\frac{^{36}\text{Cl}}{^{35}\text{Cl}}\right)_{VERA} \frac{1}{\langle\Phi_{tot}\rangle} \quad (8.1)$$

Sample material	$\langle\Phi_{tot}\rangle$ [ $10^{15}$ ]	rel. unc. $\langle\Phi_{tot}\rangle$ [%]	$\left(\frac{^{36}\text{Cl}}{^{35}\text{Cl}}\right)_{VERA}$ [ $10^{-12}$ ]	rel. unc. $\left(\frac{^{36}\text{Cl}}{^{35}\text{Cl}}\right)_{VERA}$ [%]	$\sigma_{exp}$ [mbarn]	rel.unc. $\sigma_{exp}$ [%]
KIT1	1.220	5.5	10.78	0.72	8.84	5.5
KIT2	1.274	5.5	8.81	0.38	6.88	5.5

**Table 8.1:** Experimental neutron capture cross-section for the two NaCl-pellets.  $\left(\frac{^{36}\text{Cl}}{^{35}\text{Cl}}\right)_{VERA}$  denotes the final AMS-values measured at VERA.

One can see that there is a difference of 22 % between the two values for the experimental cross-section. Up to now no corrections for the different geometry in the irradiation were applied. In the following, the differential cross-section data were taken from the ENDF/B-VII.0 database ([NEA, 2010]) and the neutron spectrum used for the irradiation was simulated with the programm PINO (see section 5.2.3). Due to the discrete character of the PINO- and differential cross-section data, equations 2.27 and 2.28 were adapted to:

$$\langle\sigma\rangle_{MB} = \frac{\sum_{E_{min1}}^{E_{max1}} \sigma(E) E e^{-\frac{E}{kT}} \Delta E}{\sum_{E_{min1}}^{E_{max1}} E e^{-\frac{E}{kT}} \Delta E} \quad (8.2)$$

$$\langle\sigma\rangle_{SACS} = \frac{\sum_{E_{min2}}^{E_{max2}} \sigma(E) N(E) \Delta E}{\sum_{E_{min2}}^{E_{max2}} E N(E) \Delta E} \quad (8.3)$$

These calculations were done with a Linux-based computer program "a.out", provided by Alberto Mengoni. In the case of  $\langle\sigma\rangle_{MB}$  the upper and lower limits of the sums are given by the limits of the energy of the differential cross-section data

( $E_{max1}=20$  MeV,  $E_{min1}=10$   $\mu\text{eV}$ ). The relevant energy region for the calculation of  $\langle\sigma\rangle_{MB}$  goes up to approximately 500 keV. The energy steps for the MB-distribution are automatically adapted to the energy steps of the differential cross-section data. The energy steps  $\Delta E$  for the  $\langle\sigma\rangle_{SACS}$  are limited by PINO to 1 keV and the upper energy of the neutrons at the KIT was calculated by PINO to  $E_{max2}=114$  keV. The lower energy limit was  $E_{min2}=0$  keV.

Sample material	Distance to neutron source [mm]	$\langle\sigma\rangle_{MB}$ [mbarn]	$\langle\sigma\rangle_{SACS}$ [mbarn]
KIT1	1.7	8.18	8.49
KIT2 pos1	2.7	8.18	7.98
KIT2 pos2	3.0	8.18	7.81

**Table 8.2:** Values for the spectrum averaged cross-section and the theoretical Maxwellian averaged cross-section calculated with the ENDF/B-VII.0 data (Evaluated Nuclear Data File <http://www-nds.iaea.org/exfor/endl.htm>). Sample KIT2 was irradiated in four parts (see tab. 5.13) in two different distances to the neutron source (pos1 and pos2).

The final values for the Maxwellian averaged cross-section for sample material KIT1 was calculated by:

$$\sigma_{MACS} = \frac{2}{\sqrt{\pi}} \frac{\langle\sigma\rangle_{MB}}{\langle\sigma\rangle_{SACS}} * \sigma_{exp} \quad (8.4)$$

For sample material KIT2 the two different neutron spectra for the two irradiation positions had to be considered and the above equation had to be modified:

$$\sigma_{MACS} = \frac{2}{\sqrt{\pi}} \frac{\langle\sigma\rangle_{MB}}{f_{2.7} \langle\sigma\rangle_{SACS2.7} + f_{3.0} \langle\sigma\rangle_{SACS3.0}} * \sigma_{exp} \quad (8.5)$$

Where  $\langle\sigma\rangle_{SACS2.7}$  and  $\langle\sigma\rangle_{SACS3.0}$  are the spectrum averaged cross-sections for a distance of 2.7 mm and 3.0 mm from the neutron sources. The weighting factors  $f_{2.7}$  and  $f_{3.0}$  are given by:

$$f_{2.7} = \frac{\Phi_{2.7}}{\Phi_{tot}} \quad (8.6)$$

$$f_{3.0} = \frac{\Phi_{3.0}}{\Phi_{tot}} \quad (8.7)$$

Here  $\Phi_{tot}$  is the total neutron fluence for sample KIT2.  $\Phi_{2.7}$  and  $\Phi_{3.0}$  are the neutron fluences in the particular position.

Source	Sample material	$\sigma_{MACS}$ [mbarn]	rel. unc. $\sigma_{MACS}$ [%]	type of work
this work	KIT1	10.47	5.5	experimental
this work	KIT2	8.79	5.5	experimental
[Bao <i>et al.</i> , 2000]	-	11.7	3	compilation
[Guber <i>et al.</i> , 2002]	-	11.0	2.7	experimental
[KADoNiS, 2006]	-	11.3	3.1	compilation

**Table 8.3:** Final values for the MACS of  $^{35}\text{Cl}$  obtained in this work and compared to values from literature. The data for the calculation of the KADoNiS value is the weighted result from the values of [Macklin, 1984] and [Guber *et al.*, 2002].

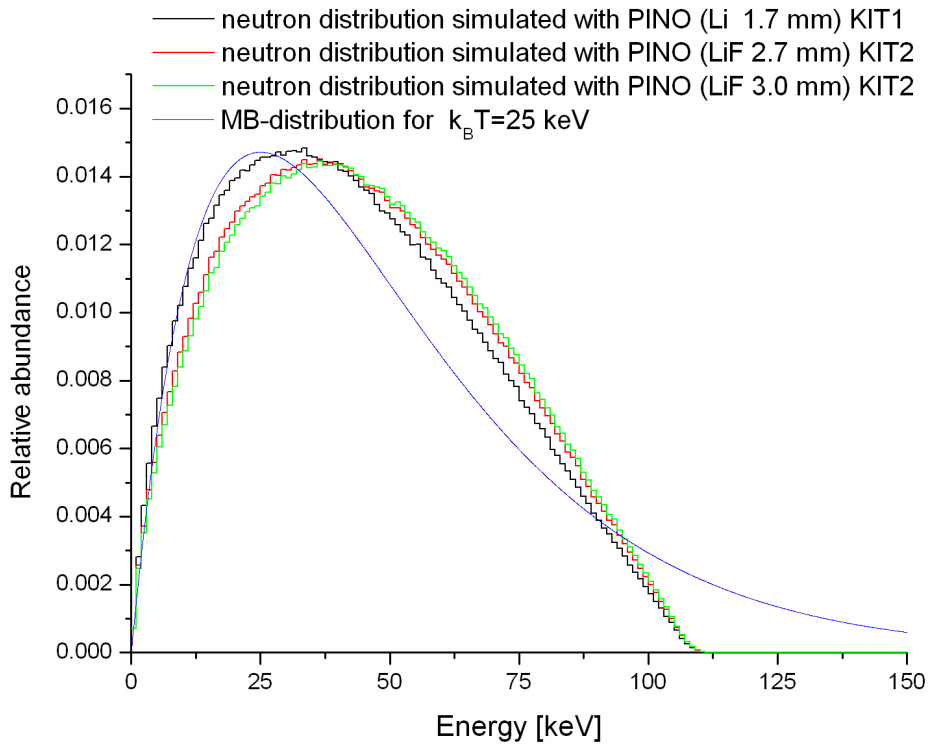


**Figure 8.1:** Comparison of a theoretical 25 keV Maxwell-Boltzmann neutron-spectrum with the experimental spectra, as simulated by PINO. The target for the  $\text{Li}(p,n)$  reaction (Li or  $\text{LiF}$ ) and the distance of the  $\text{NaCl}$  pellet from the neutron source is indicated in the legend.

## 8.2 Discussion

The following conclusions can be made from the results in the table above:

- The difference between the two measured  $\sigma_{MACS}$  values for KIT1 and KIT2 of this work has decreased to 19 %, taking into account the different geometry in the neutron activation. The reason for this still existing discrepancy is unknown. The relative big uncertainty of the measured values which is mainly caused by the uncertainty of the neutron fluence, cannot explain this deviation.
- The  $\sigma_{MACS}$  deduced from KIT1 is 5 % smaller than the value of [Guber *et al.*, 2002] but the values are in agreement within their uncertainties. The MACS in [Guber *et al.*, 2002] was calculated by pointwise measurements of the neutron capture cross-section for different energies (from 100 eV to 600 keV), taking into account 122 resonances [Guber *et al.*, 2002], at the ORELA facility in Oak Ridge. The value for KIT1 is also 12 % smaller than the value from [Bao *et al.*, 2000], which is based on energy-differential measurements of the neutron capture cross-section [Macklin, 1984]. The MACS calculated from KIT2 is 25 % smaller than the value from [Guber *et al.*, 2002] and 33 % smaller than the value given in [Bao *et al.*, 2000]. The recommended value for the  $\sigma_{MACS}$  given in [KADoNiS, 2006] (**K**arlsruhe **D**atabase of **N**ucleosynthesis in **S**tars) is 8 % bigger than the value determined from KIT1, and 29% bigger than the value determined from KIT2.

Possible sources of the discrepancies are:

- the altering of the neutron spectrum caused by target aging was not fully taken into account correctly.
- the neutron absorption and scattering in the geometry for KIT2 was not taken into account correctly.

To clarify the discrepancies of  $\sigma_{MACS}(\text{KIT2})$  to  $\sigma_{MACS}(\text{KIT1})$  and to literature values, additional NaCl samples should be irradiated with quasi Maxwellian neutron spectra. A new MACS value calculated from the data from KIT2 would cause a significant change (29%) in the stellar production rate of  $^{36}\text{Cl}$ .

## Bibliography

At the end of each citation the page(s) where the citation was used is/are given.

- Alfimov, V., Synal, H.A., Finkel, R., & Wilck, K. 2009. Re-Calibration of ETH chlorine-36 standards, Improving the quality of  $^{36}\text{Cl}/\text{Cl}$  ratio measurements. *Ion Beam Physics, ETH Zürich, Annual report*. 77
- Allen, B. J., Gibbons, J. H., & Macklin, R. L. 1971. Nucleosynthesis and neutron-capture cross sections. *Advances in Nuclear Physics*, **4**, 205–259. 13
- Arnett, D. 1996. *Supernovae and Nucleosynthesis: An Investigation of the History of Matter from the Big Bang to the Present*. Princeton University Press, 41 William Street, Princeton, New Jersey 08540. 23
- ATI. 2009. [http://www.ati.ac.at/fileadmin/files/general/Reaktor/E\\_Text\\_Bilder.PDF](http://www.ati.ac.at/fileadmin/files/general/Reaktor/E_Text_Bilder.PDF); *The TRIGA Mark-II Reaktor*. 46
- Audi, G., Wapstra, A.H., & Thibault, C. 2003. The 2003 atomic mass evaluation: (II). Tables, graphs and references. *Nuclear Physics A*, **729**, 337 – 676. 7
- Bao, Z. Y., Beer, H., Käppeler, F., Voss, F., Wisshak, K., & Rauscher, T. 2000. Neutron cross sections for nucleosynthesis studies. *Atomic Data and Nuclear Data Tables*, **76**, 70 – 154. 99, 100
- Beer, H., & Käppeler, F. 1980. Neutron capture cross sections on  $^{138}\text{Ba}$ ,  $^{140,142}\text{Ce}$ ,  $^{175,176}\text{Lu}$ , and  $^{181}\text{Ta}$  at 30 keV: Prerequisite for investigation of the  $^{176}\text{Lu}$  cosmic clock. *Phys. Rev. C*, **21**, 534–544. 51
- Berger, M. J., Hubbell, J. H., Seltzer, S.M., Chang, J., Coursey, J. S., Sukumar, R., Zucker, D. S., & Olsen, K. 1990. XCOM: Photon Cross Section Database, NIST Standard Reference Database 8 (XGAM); <http://physics.nist.gov/cgi-bin/Xcom/xcom2>. xi, 19
- Boyd, R.N. 2007. *An introduction to nuclear astrophysics*. The University of Chicago Press, Ltd, London. 23, 24, 25, 27
- Buczak, K. 2009. *Preparation of a  $^{55}\text{Fe}$ -AMS standard and the precise measurement of the neutron capture cross-section of  $^{54}\text{Fe}(n, \gamma)$* . Thesis, Universität Wien. 41, 42, 49, 60

- Conrad, N.J., Elmore, D., Kubik, P. W., Gove, H. W., Tubbs, L. E., Chrunyk, B. A., & Wahlen, M. 1986. The chemical preparation of AgCl for measuring  $^{36}\text{Cl}$  in polar ice with accelerator mass spectrometry. *Radiocarbon*, **28**, 556–560. 71, 73
- Conte, M., MacKay W. W. 2008. *An Introduction to the Physics of Particle Accelerators (2<sup>nd</sup> edition)*. World Scientific Publishing Co. Pte. Ltd 5 Toh Tuck Link, Singapore 596224. 31, 32
- Döbeli, M., Kottler, C., Stocker, M., Weinmann, S., Synal, H. A., Grajcar, M., & Suter, M. 2004. Gas ionization chambers with silicon nitride windows for the detection and identification of low energy ions. *Nuclear Instruments and Methods in Physics Research B*, **219-220**, 415 – 419. 38
- Dillmann, I. 2010. *Private communication*. ix, 70
- Dillmann, I., Domingo-Pardo, C., Heil, M., Käppeler, F., Wallner, A., Forstner, O., Golser, R., Kutschera, W., Priller, A., Steier, P., Mengoni, A., Gallino, R., Paul, M., & Vockenhuber, C. 2009. Determination of the stellar ( $n, \gamma$ ) cross section of  $^{40}\text{Ca}$  with accelerator mass spectrometry. *Phys. Rev. C*, **79**, 065805. 51, 69
- Elmore, D., Fulton, B. R., Clover, M. R., Marsden, J. R., Gove, H. E., Naylor, H., Purser, K. H., Kilius, L. R., Beukens, R. P., & Litherland, A. E. 1979. Analysis of  $^{36}\text{Cl}$  in environmental water samples using an electrostatic accelerator. *Nature*, **277**, 22–25. 27
- Endt, P. M. 1990. Energy levels of  $A = 21-44$  nuclei (VII). *Nuclear Physics A*, **521**, 1 – 400. 17
- Ferry, James A. 1993. Recent developments in electrostatic accelerator technology at NEC. *Nuclear Instruments and Methods in Physics Research A*, **328**, 28 – 33. 35
- Firestone, R.B. 2007. Nuclear Data Sheets for  $A = 24$ . *Nuclear Data Sheets*, **108**(11), 2319 – 2392. 54, 66
- Forstner, O., Michlmayr, L., Auer, M., Golser, R., Kutschera, W., Priller, A., Steier, P., & Wallner, A. 2008. Applications of a compact ionization chamber in AMS at energies below 1 MeV/amu. *Nuclear Instruments and Methods in Physics Research B*, **266**, 2213 – 2216. 38
- Guber, K. H., Sayer, R. O., Valentine, T. E., Leal, L. C., Spencer, R. R., Harvey, J. A., Koehler, P. E., & Rauscher, T. 2002. New Maxwellian averaged neutron capture cross sections for  $^{35,37}\text{Cl}$ . *Phys. Rev. C*, **65**, 058801. 99, 100
- Hou, X., Østergaard, L.F., & Nielsen, S.P. 2007. Determination of  $^{36}\text{Cl}$  in Nuclear Waste from Reactor Decommissioning. *Analytical Chemistry*, **79**(8), 3126–3134. 27, 28

- IAEA. 2007-2010. <http://www-nds.iaea.org/relnsd/vchart/index.html>; *IAEA Nuclear Data Service*. 6, 25
- KADoNiS. 2006. *KADoNiS*, <http://www.kadonis.org/>. 99, 100
- Kutschera, W., Collon, P., Friedmann, H., Golser, R., Hille, P., Priller, A., Rom, W., Steier, P., Tagesen, S., Wallner, A., Wild, E., & Winkler, G. 1997. VERA: A new AMS facility in Vienna. *Nuclear Instruments and Methods in Physics Research B*, **123**, 47 – 50. 33
- Linde, David R., National Institute of Standards & Technology Gaithersburg Maryland USA (ed). 2009. *CRC Handbook of chemistry and physics 90<sup>th</sup> edition, Internet version 2010*. CRCnetBASE, Taylor and Francis Group, LLC. 3, 4
- Litherland, A. E. 1980. Ultrasensitive mass spectrometry with accelerators. *Annual Review of Nuclear and Particle Science*, **30**, 437–473. 29
- Litherland, A.E. 1984. Accelerator mass spectrometry. *Nuclear Instruments and Methods in Physics Research B*, **5**, 100 – 108. 29, 31, 32
- Macklin, R. L. 1984. Resonance neutron capture by  $^{35,37}\text{Cl}$ . *Phys. Rev. C*, **29**, 1996–2000. 99, 100
- Magill, J., Pfennig, G., & Galy, J. 2006. *Karlsruher Nuklidkarte 7<sup>th</sup> edition*. European Communities. 4, 47, 54, 96
- Maier-Komor, P., Bergmaier, A., Dollinger, G., Frey, C. M., & Körner, H. J. 1997. Improvement of the preparation procedure of carbon stripper foils from the laser plasma ablation-deposition process. *Nuclear Instruments and Methods in Physics Research A*, **397**, 131 – 136. 36
- Martschini, Martin. 2011. Ph.D. thesis, Work in preparation, Universität Wien. 76
- Merchel, S., Arnold, M., Aumaître, G., Benedetti, L., Bourlès, D.L., Braucher, R., Alfimov, V., Freeman, S.P.H.T., Steier, P., & Wallner, A. 2008. Towards more precise  $^{10}\text{Be}$  and  $^{36}\text{Cl}$  data from measurements at the 10-14 level: Influence of sample preparation. *Nuclear Instruments and Methods in Physics Research Section B*, **266**, 4921 – 4926. 71
- Milton, G.M., Andrews, H.R., Causey, S.E., Chant, L.A., Cornett, R.J., Davies, W.G., Greiner, B.F., Koslowsky, V.T., Imahori, Y., Kramer, S.J., McKay, J.W., & Milton, J.C.D. 1994. Chlorine-36 dispersion in the Chalk River area. *Nuclear Instruments and Methods in Physics Research B*, **92**, 376 – 379. 27
- Mohr, P.J., Taylor, B.N., & Newell, D.B. 2008. CODATA recommended values of the fundamental physical constants: 2006. *Rev. Mod. Phys.*, **80**, 633–730. 47, 54

- Molnár, G., Belgya, T., Dabolczi, L., Fazekas, B., Révay, Z., Veres, Á., Bikit, I., Kiss, Z., & Östör, J. 1997. The new prompt gamma-activation analysis facility at Budapest. *Journal of Radioanalytical and Nuclear Chemistry*, **215**, 111–115. 10.1007/BF02109886. 48
- Mughabghab, S.F., Divadeenam M. Holden N.E. 1981. *Neutron Cross Sections from Neutron Resonance Parameters and Thermal Cross Sections*; <http://isotopes.lbl.gov/ngdata/sig.htm>. Academic Press, New York (1981). 41, 46, 47, 54, 64
- NEA. 2010 (10). <http://www.nea.fr/janis/>, *NEA databank, JANIS3.2*. 14, 97
- NIST. 2006. <http://physics.nist.gov/cgi-bin/cuu/Category?view=pdf&Atomic+and+nuclear.x=122&Atomic+and+nuclear.y=12>, *Fundamental physical constants*. 6
- NIST. 2009. <http://physics.nist.gov/PhysRefData/XrayMassCoef/tab3.html>. 26, 54, 59
- NNDC. 2005. <http://www.nndc.bnl.gov/chart>; *Interactive chart of nuclides*. 4, 41, 47, 54, 83
- Orlowski, T., Forstner, O., Golser, R., Kutschera, W., Merchel, S., Martschini, M., Priller, A., Steier, P., Vockenhuber, C., & Wallner, A. 2010. Comparison of detector systems for the separation of  $^{36}\text{Cl}$  and  $^{36}\text{S}$  with a 3-MV tandem. *Nuclear Instruments and Methods in Physics Research B*, **268**, 847 – 850. 39
- Priller, A., Golser, R., Hille, P., Kutschera, W., Rom, W., Steier, P., Wallner, A., & Wild, E. 1997. First performance tests of VERA. *Nuclear Instruments and Methods in Physics Research B*, **123**, 193 – 198. 36
- Priller, A., Melber, K., Forstner, O., Golser, R., Kutschera, W., Steier, P., & Wallner, A. 2010. The new injection beamline at VERA. *Nuclear Instruments and Methods in Physics Research B*, **268**, 824 – 826. 35
- Ratynski, W., & Käppeler, F. 1988. Neutron capture cross section of  $^{197}\text{Au}$ : A standard for stellar nucleosynthesis. *Phys. Rev. C*, **37**, 595–604. 13, 14, 54
- Reifarth, R., Heil, M., Käppeler, F., & Plag, R. 2009. PINO—a tool for simulating neutron spectra resulting from the  $^7\text{Li}(p,n)$  reaction. *Nuclear Instruments and Methods in Physics Research A*, **608**, 139 – 143. 51
- Schaller, G., Schaerer, D., Meynet, G., & Maeder, A. 1992. New grids of stellar models from 0.8 to 120 solar masses at  $Z = 0.020$  and  $Z = 0.001$ . *Astronomy and Astrophysics Supplement Series*, **96**(Dec.), 269–331. 24, 25
- Segré, Emilio. 1977. *Nuclei and Particles, second edition*. Addison-Wesley Publishing Company, Inc. 5, 6, 7, 8, 9, 10, 11, 18, 20, 21

- Seki, R., Matsuihiro, T., Nagashima, Y., Takahashi, T., Sasa, K., Sueki, K., Tosaki, Y., Bessho, K., Matsumura, H., & Miura, T. 2007. Isotopic ratios of  $^{36}\text{Cl}/\text{Cl}$  in Japanese surface soil. *Nuclear Instruments and Methods in Physics Research B*, **259**, 486 – 490. 27
- Steier, P. 2000. *Exploring the limits of VERA: A universal facility for accelerator mass spectrometry*. Ph.D. thesis, Universität Wien. 79
- Steier, P., Golser, R., Liechtenstein, V., Kutschera, W., Priller, A., Vockenhuber, C., & Wallner, A. 2005. Opportunities and limits of AMS with 3-MV tandem accelerators. *Nuclear Instruments and Methods in Physics Research B*, **240**, 445 – 451. 37
- Steier, P., Forstner, O., Golser, R., Kutschera, W., Martschini, M., Merchel, S., Orłowski, T., Priller, A., Vockenhuber, C., & Wallner, A. 2010.  $^{36}\text{Cl}$  exposure dating with a 3-MV tandem. *Nuclear Instruments and Methods in Physics Research B*, **268**, 744 – 747. 35, 71, 78
- Stocker, M., Döbeli, M., Grajcar, M., Suter, M., Synal, H. A., & Wacker, L. 2005. A universal and competitive compact AMS facility. *Nuclear Instruments and Methods in Physics Research B*, **240**, 483 – 489. 38
- Stone, J.O., Allan, G.L., Fifield, L.K., & Cresswell, R.G. 1996. Cosmogenic chlorine-36 from calcium spallation. *Geochimica et Cosmochimica Acta*, **60**(4), 679 – 692. 71, 73
- Szentmiklósi, L., Belgya, T., Révay, Z., & Kis, Z. 2010. Upgrade of the prompt gamma activation analysis and the neutron-induced prompt gamma spectroscopy facilities at the Budapest research reactor. *Journal of Radioanalytical and Nuclear Chemistry*, **286**, 501–505. 10.1007/s10967-010-0765-4. 48
- Tikhomirov, D., & Blinov, A. 2009. Cosmogenic  $^{36}\text{Cl}$  as a tool for dating permafrost ice. *Bulletin of the Russian Academy of Sciences: Physics*, **73**, 384–386. 10.3103/S1062873809030319. 27
- Tözsér, S. 2009. <http://www.kfki.hu/brr/indexen.htm> Full-scale reconstruction and upgrade of the Budapest Research Reactor. 48
- Vockenhuber, C., Ahmad, I., Golser, R., Kutschera, W., Liechtenstein, V., Priller, A., Steier, P., & Winkler, S. 2003. Accelerator mass spectrometry of heavy long-lived radionuclides. *International Journal of Mass Spectrometry*, **223-224**, 713 – 732. 33, 35, 36, 37
- Wagner. 1991. *Kalibrierung des HP-Ge Detektors*. 54, 60, 61, 62, 63
- Wallerstein, G., Iben, Jr., I., Parker, P., Boesgaard, A.M., Hale, G.M., Champagne, A.E., Barnes, C.A., Käppeler, F., Smith, V.V., Hoffman, R.D., Timmes, F.X.,

## Bibliography

---

- Snedden, C., Boyd, R.N., Meyer, B.S., & Lambert, D.L. 1997. Synthesis of the elements in stars: forty years of progress. *Reviews of Modern Physics*, **69**, 995–1084. 24, 25, 26, 27
- Weaver, T.A., Zimmerman, G.B., & Woosley, S.E. 1978. Presupernova evolution of massive stars. *Astrophysical Journal*, **225**, 1021–1029. 24, 25
- Wilson, E., J. N. 2001. *An introduction to Particle Accelerators*. Oxford University Press Inc., New York. 31, 32
- Wittkower, A. B., & Ryding, G. 1971. Equilibrium Charge-State Distributions of Heavy Ions (1-14 MeV). *Phys. Rev. A*, **4**(1), 226–232. 31
- Xiaolong, H. 2009. Nuclear Data Sheets for A = 198. *Nuclear Data Sheets*, **110**, 2533 – 2688. 16, 52, 54, 70

## Acknowledgments

The "AMS measurement of the reaction  $^{35}\text{Cl}(n,\gamma)^{36}\text{Cl}$ " is not only relevant for astrophysics and nuclear technology, but for two years, it was also an important part of my life. A lot of people helped me to master this period of my life. Therefore I want to express my gratitude.

At first, I want to thank my advisor Anton Wallner, for the proposal of the diploma thesis, for the discussions of the measured data, and his advices regarding the evaluation of this data and the theoretical and mathematical background. Toni, thanks for your patience in the discussions concerning this work. Thanks for always having time for me, especially in the final stage of the work, when you were in Australia and a time offset of ten hours made communication more complicated. Thank you very much.

Martin Martschini, thanks for sharing your experience of AMS-measurements, -evaluations and chemical pretreatment of chlorine with me. Thanks for the mentoring and support during the beam-times, for your patience and for helping me turning megabytes of data into meaningful results. It was a pleasure to have an additional, inofficial advisor like you.

Claudia Lederer, thanks for helping me with the activity measurements and for your suggestions towards calculating the MACS. I also want to thank you for the organization of the "Physikerabende", which always were fun.

Leonard Michlmayr, thanks for the help considering computer problems. Thanks for your help with Latex and for the discussion of interesting mathematical and physical problems.

Jenny Feige, thanks for your Latex advices, interesting office conversation in late afternoon hours and for lending me an ear when I was "moaning" about minor problems of my work.

Karin Eisenhut and Klaus Mair, you went through the same difficulties of writing a diploma thesis at the same time as I. Thanks for motivating conversations regarding all these difficulties.

Oliver Forstner, Alfred Priller and Peter Steier thanks for the help during the

## *Acknowledgments*

---

beam-times and for advices according AMS-measurements. Oliver thanks for solving some software problems and Peter thanks for the delicious VERA-lunches.

Peter Kueß, thanks for your help with the activity measurements.

Robin Golser, thanks for organizational help and for proposing Anton Wallner as advisor to me.

Gerhard Winkler, thanks for discussing neutron absorption, neutron scattering and the math of activity measurements and uncertainties with me.

Walter Kutschera, Jakob Liebl and again Robin Golser and Peter Steier, thanks for your time and your advices during the preparation of my talk and poster for the "ÖPG-Tagung".

Kerstin Rumpelmayr and Franz Dellinger thanks for the enjoyable coffee breaks.

I want to thank Max Bichler, Georg Steinhauser and Mario Villa for the irradiation of NaCl-samples at the ATI in Vienna.

Thanks to Tamás Belgya, László Szentmiklósi and Zoltán Kis for receiving me so kindly at the KFKI in Budapest and for the irradiation of NaCl samples at the BRR.

Thanks to Iris Dillmann for the data of the irradiations and the activity measurements of the NaCl samples from KIT.

Thanks to Neven Soić and Željko Pastuović for the correction of the Croatian abstract. Lijepa hvala.

Thanks to Gabi Obstmayer for manufacturing the Al-target-holders for the irradiations.

Thanks to Helga Vincro and Renée Pollack for their help with bureaucracy.

Especially I want to thank Kathi Buczak for her advices in numerous cases, regarding this work and also more private problems. Thanks for the long and interesting conversations, the mental support and for always having time for me. Thanks for simply being one of my best- and my most reliable friend. Dziękuję że jesteś taką dobrą i wiarygodną przyjaciółką.

Thanks to all my other friends which accompanied me throughout my life as a student.

---

I want to thank my family for the support and the tolerance during the work on this thesis. Thanks to my parents for their financial support, which allowed me to study what I want and to enjoy a "students-life". Thanks to my father for helping me with the Croatian translation of the abstract.

Lipa hvala za vaš trud koga ste s manom imali. Hvala da mi uvijek pomorete najti "pravi" put u životu i da ste me odgojili na pravičnoga čovika. Na kraju i lipa hvala za financijsko i organizatorsko podupiranje, ko mi je stopr omogućilo studij fizike.

*Acknowledgments*

---

# Curriculum vitae

**Name:** Stefan Pavetich  
**Date of birth:** 27.03.1984  
**Place of birth:** Oberpullendorf, Austria  
**Parents:** Stefan and Maria Pavetich (born Dragschits)  
**Nationality:** Austria  
**Marital status:** Single

## Education:

**1990-1994** Volksschule Nikitsch  
**1994-2002** Bundesoberstufenrealgymnasium (BORG) Oberpullendorf  
**24.06.2002** Matura mit ausgezeichnetem Erfolg  
**Sep. 2002 - Apr. 2003** Military service, Sporck-Kaserne Oberwart  
**since 2003** Student of physics at the University of Vienna  
**since Jan. 2009** Diploma thesis at the Vienna Environmental Research Accelerator (VERA), Isotope Research, Faculty of Physics, University of Vienna, *AMS measurement of the reaction  $^{35}\text{Cl}(n,\gamma)^{36}\text{Cl}$  and its relevance to astrophysics and nuclear technology*, Advisor: Mag. Dr. Anton Wallner

## Work experience:

**since 2000** intermittently work at the BMV (Burgenländischer Müllverband)  
**summer 2001:** work at archaeological excavation in Unterpullendorf  
**since 2002:** private lessons in mathematics and physics  
**since summer 2008:** part time work at Fruhmann GmbH NTL Manufacturer & Wholesaler, developing experiments for education of physics in schools  
**summer semester 2008:** e-tutor for the lecture *Praktikum zur Einführung in die Physik 2*

## Publications and talks:

**Sep. 2010** I presented preliminary results of this work (talk and poster) at the 60<sup>th</sup> Annual Meeting of the Austrian Physical Society in Salzburg.